Confocal single molecule fluorescence detection - methodical developments and applications to biological specimens

Von der Fakultät für Mathematik, Informatik und Naturwissenschaften der RWTH Aachen University zur Erlangung des akademischen Grades eines Doktors der Naturwissenschaften genehmigte Dissertation

vorgelegt von

Diplom-Physiker

Daryan Kempe

aus Hemmerde bei Unna

Berichter: Prof. Dr. rer. nat. Jörg Fitter

Prof. Dr. rer. nat. Dominik Wöll

Tag der mündlichen Prüfung: 6. September 2017

"You miss 100 percent of the shots you never take."

Wayne Gretzky

Publication list

Parts of this thesis were submitted and accepted for publication.

- Lamprou, P.*, Kempe, D.*, Katranidis, A., Büldt, G. and Fitter, J. (2014). Nanosecond Dynamics of Calmodulin and Ribosome-Bound Nascent Chains Studied by Time-Resolved Fluorescence Anisotropy. ChemBioChem, 15, 977-985 (*equal contribution)
- Höfig, H., Gabba, M., Poblete, S., Kempe, D. and Fitter, J. (2014). Inter-Dye Distance Distributions Studied by a Combination of Single-Molecule FRET-Filtered Lifetime Measurements and a Weighted Accessible Volume (wAV) Algorithm, Molecules, 19 (12), 19269-19291
- Kempe, D.*, Schöne, A., Fitter, J. and Gabba, M.* (2015). Accurate Fluorescence Quantum Yield Determination by Fluorescence Correlation Spectroscopy, The Journal of Physical Chemistry B, 119 (13), 4668-4672 (*equal contribution)
- Kempe, D., Cerminara, M., Poblete, S., Schöne, A., Gabba, M. and Fitter, J. (2017). Single-molecule FRET measurements in additive-enriched aqueous solutions, Analytical Chemistry, 89 (1), 694-702

Abstract

Over the last few decades, single-molecule FRET has become a valuable tool enlightening the fields of molecular conformational dynamics, folding and structure determination of biological macro-molecules. However, quantitative statements about any parameter obtained using FRET are based on a precise calibration of the acquired data, among others taking into account the properties of the FRET-pair used. In this work, two methods are developed and established that facilitate this calibration by means of confocal microscopy, automatically allowing a sample characterization under application relevant conditions, i.e. close to the single-molecule level. To assess the orientation factor entering the Förster radius calculation, time-resolved anisotropy measurements are performed. In this regard, the depolarization effects induced by the use of a high numerical aperture objective have to be taken into account by two correction factors. These are precisely determined by combining an extended experimental calibration procedure adjusted to the temporal resolution of the setup at hand with theoretical predictions considering the exact measurement conditions. To determine the fluorescence quantum yields of donor and acceptor used in the FRET efficiency calculation, the linear relation between the molecular brightness, made accessible by Fluorescence Correlation Spectroscopy, and the fluorescence quantum yield in the limit of low excitation intensities is exploited. Based on this, the presented quantum yield determination method lowers the needed amount of sample by a factor of around thirty as compared to a commonly applied optical method, but still provides at least the same precision. As compared to fluorescence lifetime based quantum yield determination methods, the novel approach is more comprehensive as it is sensitive not only to dynamic, but also to static fluorescence quenching. Hence, apart from its relevance for smFRET, a reliable characterization of biological samples with limited expression yields is made possible. With these two methodical developments available, smFRET data of structurally rigid, double-stranded DNA-oligonucleotides in aqueous buffer and in buffers with specific amounts of glycerol, guanidine hydrochloride and sodium chloride added are analyzed. It is demonstrated that the calculation of inter-dye distances, without taking into account solvent-induced spectral and photo-physical changes of the labels, leads to deviations of up to 4 $\AA$ from the real inter-dye distances and furthermore to a misinterpretation of the underlying structural changes. Additionally, it is experimentally shown that electrostatic dye-dye repulsions are negligible for the inter-dye distance regime considered here (> 50 $\AA$). Expanding the given framework of accessible volume calculations by taking into account the electrostatic interaction potential of donor and acceptor in the respective solvent environment, these findings are supported by theoretical predictions. Finally, all methodical approaches and experimental/theoretical findings are combined to validate the further compaction of the already unfolded state of the protein Phosphoglycerate Kinase (PGK) with decreasing concentrations of denaturant, a mechanism

known as coil-globule transition.

Zusammenfassung

Immer wieder werden mit Hilfe von Förster Resonanz Energie Transfer (FRET) Messungen auf Einzelmolekülniveau wertvolle Erkenntnisse in den Bereichen der molekularen Konformationsdynamik, der Faltung und der Strukturaufklärung von biologischen Makromolekülen erlangt. Quantitative und präzise Aussagen können dabei nur mittels einer genauen Kalibrierung der erhobenen Daten gewonnen werden, welche unterem anderen die Eigenschaften der als FRET-Paar eingesetzten Farbstoffe berücksichtigen muss. In dieser Arbeit werden zwei Methoden entwickelt und etabliert, die es ermöglichen die benötigte Farbstoffcharakterisierung mit einem Konfokalmikroskop durchzuführen, folglich können die betrachteten FRET-Proben unter anwendungsnahen Bedingungen, d.h. nahe dem Einzelmolekülniveau vermessen werden. Zuerst wird der für die Berechnung des Förster Radius benötigte Orientierungsfaktor mittels zeitaufgelöster Fluoreszenzanisotropie Messungen abgeschätzt. Durch die in der Konfokalmikroskopie verwendeten Objektive mit hoher numerischer Apertur können dabei Depolarisationsartefakte auftreten, die durch zwei Korrekturfaktoren berücksichtigt werden müssen. Die präzise Bestimmung dieser Korrekturfaktoren wird in dieser Arbeit mit Hilfe der Kombination von theoretischen Vorhersagen mit einer erweiterten experimentellen, an das zeitliche Auflösungsvermögen des Systems angepassten Kalibrierungsprozedur erreicht. Um die Fluoreszenzquantenausbeuten von FRET Donor und Akzeptor zu bestimmen, die direkt in die Berechnung der FRET Effizienzen eingehen, wird die lineare Abhängigkeit der molekularen Helligkeit, zugänglich durch die Methode der Fluoreszenz Korrelations Spektroskopie, von der Quantenausbeute im Grenzbereich kleiner Anregungsintensitäten ausgenutzt. Die darauf basierende Methode zur Quantenausbeutenbestimmung benötigt im Vergleich mit anderen häufig verwendeten optischen Verfahren nur einen Bruchteil (ca. drei Prozent) der Stoffmenge und ist dennoch mindestens genauso präzise. Durch ihre Sensibilität für dynamische und statische Fluoreszenzauslöschung ist die neu etablierte Methode zudem umfassender als andere Verfahren. Neben der Charakterisierung von Einzelmolekül FRET Proben ist sie generell zur Vermessung von (biologischen) Proben mit geringer Stoffmengenausbeute geeignet. Mit Hilfe der genannten methodischen Entwicklungen werden dann Einzelmolekül FRET Daten von strukturell rigiden, doppelsträngigen DNA Oligonukleotiden in reinem wässrigem Puffer und in Puffer mit bestimmten, hinzugegebenen Mengen von Glycerol, Guanidinhydrochlorid und Natriumchlorid analysiert. Es wird gezeigt, dass ohne die Korrektur von Solvens-induzierten photophysikalischen und spektralen Änderungen der fluoreszierenden Marker die berechneten Abstände zwischen Donor und Akzeptor-Farbstoff um bis zu 4 $\AA$ von den realen Abständen abweichen und zudem die zugrunde liegenden strukturellen Prozesse fehlinterpretiert werden. Zudem wird experimentell demonstriert und theoretisch untermauert, dass die elektrostatische Farbstoff-Farbstoff Repulsion für die betrachteten Abstände (> 50 $\AA$)

vernachlässigbar klein ist. Zuletzt werden alle methodischen Entwicklungen und experimentellen/theoretischen Resultate kombiniert um Erkenntnise über den schon entfalteten Zustand des Proteins Phosphoglyceratkinase in Abhängigkeit von der Denaturierungsmittelkonzentration zu gewinnen.

Acknowledgements

Zuerst möchte ich meinem Betreuer Prof. Jörg Fitter für die Möglichkeit danken, meine Promotion in seiner Arbeitsgruppe durchführen zu dürfen. Ich finde es bemerkenswert, dass Prof. Fitter für persönliche sowie fachliche Gespräche immer zur Verfügung steht und immer motiviert ist, seine Studenten beim Aufbau einer (wissenschaftlichen) Karriere zu unterstützen. Rückblickend kann ich nur sagen, dass ich die Zeit in der AG Biophysik sehr genossen habe und nur hoffen kann, in Zukunft weiterhin in so einer angenehmen und kollegialen Atmosphäre zu arbeiten.

Prof. Dominik Wöll möchte ich gerne dafür danken, dass er sich als Zweitgutachter für meine Doktorarbeit zur Verfügung gestellt hat.

Weiterhin möchte ich allen Mitgliedern der AG Biophysik für die gute persönliche sowie fachliche Kommunikation danken. Insbesondere möchte ich mich bei Julia Walter bedanken, die mit ihrer großen Kompetenz und ihrem sympathischen Wesen „den Laden am Laufen hält“. Alyazan Albarghash möchte ich dafür danken, dass er mich in Notsituationen anstandslos in der Lehre vertreten hat und er mit seiner offenen Art den Arbeitsalltag aufgehellt hat. Henning Höfig möchte ich für die netten Büro-Gespräche und die generell gute Zusammenarbeiten danken. Nicht zuletzt möchte ich auch allen Bachelor-und Masterstudenten danken die ich in den letzten Jahren betreut habe und die mein Leben immer wieder neu bereichert haben.

Bei allen Mitarbeitern des I. Physikalischen Instituts der RWTH Aachen möchte ich mich für die angenehme Zusammenarbeit bedanken.

I would like to thank Dr. Simón Poblete for the development of the extended AV code and the great collaboration in this regard.

Des Weiteren möchte ich mich bei der gesamten Molecular Biophysics Group im ICS-5 des Forschungszentrum Jülich bedanken, insbesondere bei Antonie Schöne, Ilona Ritter und Dr. Michele Cerminara für die fruchtbare Zusammenarbeit am PGK Projekt. Many thanks go to Dr. Matteo Gabba for being a supportive and creative colleague and collaborator during and after my time at the Forschungszentrum Jülich. Zudem möchte ich ganz besonders Dr. Tina Züchner dafür danken, dass sie mit ihrer enormen Kompetenz dauernd dazu bereit war, mir bei Belangen jeglicher Art voll und ganz weiter zu helfen. Ohne sie hätte die Arbeit in Aachen etliche Male lange still gelegen.

Zuletzt möchte ich meinen Eltern, meinem Bruder Florian und meiner Freundin Lioba für ihre andauernde und verlässliche Unterstützung danken.

Contents

Publication list iii

Abstract v

Zusammenfassung vii

Acknowledgements ix

1 Introduction 1

2 Materials 9
2.1 Fluorophores . . . 9
2.2 Bio-molecules . . . 9
2.2.1 DNA oligo-nucleotides . . . 9
2.2.2 Phosphoglycerate Kinase (PGK) from *Saccharomyces cereviseae* . . . 10
2.3 Buffers . . . 10
2.3.1 DNA buffer . . . 10
2.3.2 PGK buffer . . . 11
2.3.3 PBS . . . 11
2.4 Glycerol solutions . . . 11
2.5 Cover slip surface preparation . . . 11
2.6 Software . . . 12

3 Instrumentation 13
3.1 Confocal setup . . . 13
3.2 Other instruments used in this work . . . 17

4 Theory and methods 19
4.1 Fluorescence . . . 19
4.1.1 Fluorescence lifetime . . . 20
Time-correlated single-photon counting (TCSPC) histograms . . . 20
Pile-up . . . 22
The instrument response function (IRF) . . . 22
4.1.2 Fluorescence quantum yield . . . 23
Quantum yield determination: standard approach . . . 23
4.1.3 Absorption: The Lambert-Beer law . . . 23
4.2 Single-molecule FRET (smFRET) measurements . . . 25
4.2.1 FRET theory in a nutshell . . . 25
4.2.2 Confocal single-molecule spectroscopy in solution . . . 29
One molecule at a time: the Poisson distribution . . . 30
The molecule detection function (*MDF*) . . . 31
An important quantity: the signal-to-noise ratio (SNR) 34

Selection of fluorescence bursts . . . 35
4.2.3 Single-molecule FRET . . . 40
Labeling . . . 40
Acquisition of FRET efficiencies . . . 41
Pulsed interleaved excitation (PIE) and burst coincidence 42
4.3 Fluorescence Correlation Spectroscopy (FCS) . . . 44
4.3.1 FCS theory boiled down . . . 45
The *MDF* and the effective volume . . . 46
Pure diffusion, triplet and calibration equation . . . 47
Detector after-pulsing . . . 48
4.4 Time-resolved anisotropy (TRA) measurements . . . 49

5 Results **53**
5.1 Characterization of the confocal microscope MT200 . . . 53
5.1.1 Laser beam size characterization . . . 53
5.1.2 Power diode read-out: Conversion from a.u. to Watts 53
5.1.3 Molecule detection function (MDF) . . . 56
Bead imaging . . . 56
FCS . . . 56
MDF volume overlap . . . 58
5.2 Temporal resolution of the MT200: the instrument response function (IRF) . . . 58
5.3 Determination of depolarization corrections factors . . . 59
5.4 Quantum yield determination by low-intensity FCS (liFCS) . 63
5.4.1 Theoretical fundamentals of the liFCS approach . . . 63
5.4.2 liFCS approach: experimental realization . . . 65
Determination of the molecular brightness . . . 65
Finding the linear regime experimentally . . . 67
Determination of the absorption coefficient . . . 67
Determination of the transmission/detection efficiency parameter . . . 68
5.4.3 The MDF: case differentiation . . . 71
Refractive index mismatch and EID: theoretical insights 71
Refractive index mismatch and *MDF*: experimental results . . . 73
Refractive index mismatch and *MB*: experimental results 75
5.4.4 Experimental validation of the liFCS approach . . . 76
5.4.5 Comparison of liFCS approach with lifetime-based method . . . 78
5.5 smFRET measurements in additive-enriched solutions . . . 84
5.5.1 Physical properties of employed solvents . . . 84
5.5.2 FRET studies of rigid DNA-oligonucleotides . . . 84
Sample introduction . . . 84
Fluorescent markers: directly solvent-induced changes only . . . 85
Assessment of the the orientation factor κ^2 . . . 85
Determination of FRET calibration parameters . . . 86
Single-molecule measurements: optimal excitation intensity . . . 87
smFRET measurements . . . 88
5.5.3 Inter-dye distance calculations: electrostatic interactions 90

5.5.4 Coil-globule transition of Phosphoglycerate-Kinase . 95
Sample introduction 95
Fluorescence lifetime analysis 96
Assessment of the orientation factor κ^2 97
Determination of FRET calibration parameters 98
smFRET measurements 98

6 Discussion/Outlook **101**
6.1 Depolarization correction factors 101
6.2 Quantum yield determination by liFCS 102
6.3 smFRET measurements in additive-enriched solutions . . . 104

A Appendix **107**

B Appendix **115**

Bibliography **119**

List of Figures

1.1 Protein folding funnel . . . 2
1.2 Discrepancy smFRET and SAXS . . . 6

3.1 MT200: Laser combining unit (LCU) . . . 15
3.2 MT200: Main optical unit (MOU) . . . 16

4.1 Jablonski diagram . . . 19
4.2 TCSPC histogram generation . . . 21
4.3 Concentration depolarization . . . 25
4.4 Transfer efficiency . . . 28
4.5 Single-molecule detection . . . 29
4.6 Poisson distribution . . . 30
4.7 Gaussian beam . . . 32
4.8 Collection efficiency function . . . 33
4.9 Depiction dynamic binning . . . 36
4.10 10 bp DNA smFRET timetrace . . . 37
4.11 Countrate distribution background . . . 38
4.12 Burst duration/size distributions . . . 39
4.13 Maleimide reaction . . . 40
4.14 TCSPC PIE . . . 43
4.15 Coincidence FRET PIE . . . 43
4.16 FRET histogram PIE . . . 44
4.17 Depolarization due to high NA objective . . . 51

5.1 Laser beam characterization . . . 54
5.2 Conversion power-diode readout to Watts . . . 55
5.3 Point-spread function cross-sections . . . 57
5.4 MDF volume overlap . . . 58
5.5 IRF red and blue . . . 59
5.6 Depolarization correction factors . . . 62
5.7 *MB* AL488 . . . 64
5.8 Intensity time trace . . . 65
5.9 Triplet fraction . . . 67
5.10 Pure diffusion fit . . . 68
5.11 *MB*-curves . . . 69
5.12 Absorption coefficient . . . 70
5.13 g . . . 70
5.14 MDF refractive index mismatch . . . 72
5.15 D_r AL488 Glycerol . . . 74
5.16 Calibration of the effective volume . . . 75
5.17 Integrated MDF ratio . . . 76
5.18 liFCS *MB* . . . 77
5.19 QY AT488/AT655 in Glycerol . . . 79
5.20 QY AL488 TRP . . . 80

5.21 Quenching AL488 TRP 81
5.22 Natural lifetime AL488 Al647 82
5.23 DNA AV 85
5.24 DNA and free dye spectra in Glycerol 86
5.25 Excitation intensity and SBR 87
5.26 SNR 88
5.27 Inter-dye distances DNA 89
5.28 Efficiency histograms DNA 91
5.29 Electrostatic interaction scenarios 94
5.30 Inter-dye distances elctrostatic scenarios 95
5.31 PGK S1C Q135C and AV clouds 96
5.32 PGK S1C Q135C TRA 97
5.33 PGK S1C Q135C FRET 99
5.34 PGK S1C Q135C inter-dye distances 100

A.1 MB curve red dyes 107
A.2 Absorption cyan dyes 108
A.3 Fluorescence cyan dyes 109
A.4 Transmission/detection efficiency g cyan dyes 110
A.5 DNA spectra 111
A.6 AL488/AL647-linker structure, AV parameter 112
A.7 Dynamic viscosity GdnHCl 113

List of Tables

3.1 Properties of objectives 14

5.1 $1/e^2$ half axis of PSF 56
5.2 Depolarization correction factors 61
5.3 Quantum yields AL488/Al647 in Glycerol 77
5.4 QY fluorophores 78
5.5 Properties of solvents 84
5.6 TRA DNA constructs 86
5.7 FRET calibration factors DNA 87
5.8 Linker-dye parameters AV 92
5.9 Inter-dye distances expanded AV 93
5.10 Fluorescence lifetimes PGK 97
5.11 FRET calibration factors PGK 98

B.1 D_t AL488 in Glycerol 115
B.2 FRET efficiency values DNA constructs 115
B.3 Förster radii DNA 116
B.4 Inter-dye distances DNA 116
B.5 TRA PGK 116
B.6 FRET efficiency values PGK 117
B.7 Förster radii PGK 117
B.8 Inter-dye distances PGK 117
B.9 Linker-dye parameters AV 117

Dedicated to my parents.

Chapter 1

Introduction

In 2014, with the Nobel prize in chemistry awarded to Moerner, Hell and Betzig for the development of super-resolved fluorescence microscopy, the scientific relevance and inter-disciplinary future potential of single-molecule techniques was impressively acknowledged. Although the Nobel prize committee's focus was set on the conceptual developments needed to transcend Abbe's diffraction limit of $\lambda/2$ to resolve structures that are only 20 nm (or even less) apart [1, 2], unquestionable single-molecule microscopy/spectroscopy in general has opened the doors to ground-breaking new insights [3].

Taking a few steps back, the first observation of single pentacene molecules in a p-terphenyl host crystal at cryogenic temperatures was achieved almost thirty years ago [4–6]. Shortly after that, the first observation of single fluorescent Rhodamine-6G molecules in solution at room temperature [7] proved that single-molecule fluorescence measurements had the potential to become a valuable tool not only in the physical but also the life sciences. At that time, measurements in solution were performed with the help of a flow-cell and the required signal-to-noise ratio was achieved by means of the temporal discrimination between scattered and fluorescence photons. By employing a laser beam focused by a high numerical aperture objective and a confocal pinhole, the number of scatterers contributing to the signal could be significantly reduced, hence circumventing the need of temporal gating in single-molecule detection [8]. Still nowadays, and more specifically in this work, epi-fluorescence confocal microscopy setups equipped with single-photon sensitive detectors (like single-photon avalanche diodes or photo-multiplier tubes) and time-correlated single-photon counting electronics are frequently employed for measurements of single molecules diffusing in solution [9]. Analyzing the bursts of fluorescence created by each molecule during its transit through the confocal volume, information about, for example, spectral identity, brightness, rotational and translational diffusion and fluorescence lifetime can be obtained [10].

As distinct from ensemble measurements yielding an average value of the considered experimental variable, single-molecule measurements provide the complete probability distribution function of a given parameter. This is of specific importance considering the heterogeneous, unsynchronized and dynamic systems commonly studied in the life sciences, like proteins in differently folded states, conformations or stages of an enzymatic cycle for instance. Obviously, assuming an adequate temporal resolution, also rare intermediates can be identified by single-molecule methods that would get lost in the shuffle otherwise [11]. Additionally, single-molecule

fluorescence spectroscopy does not only facilitate the determination of several sub-states in a given sample, but also allows to analyze whether these sub-states are static or inter-convert dynamically [12].

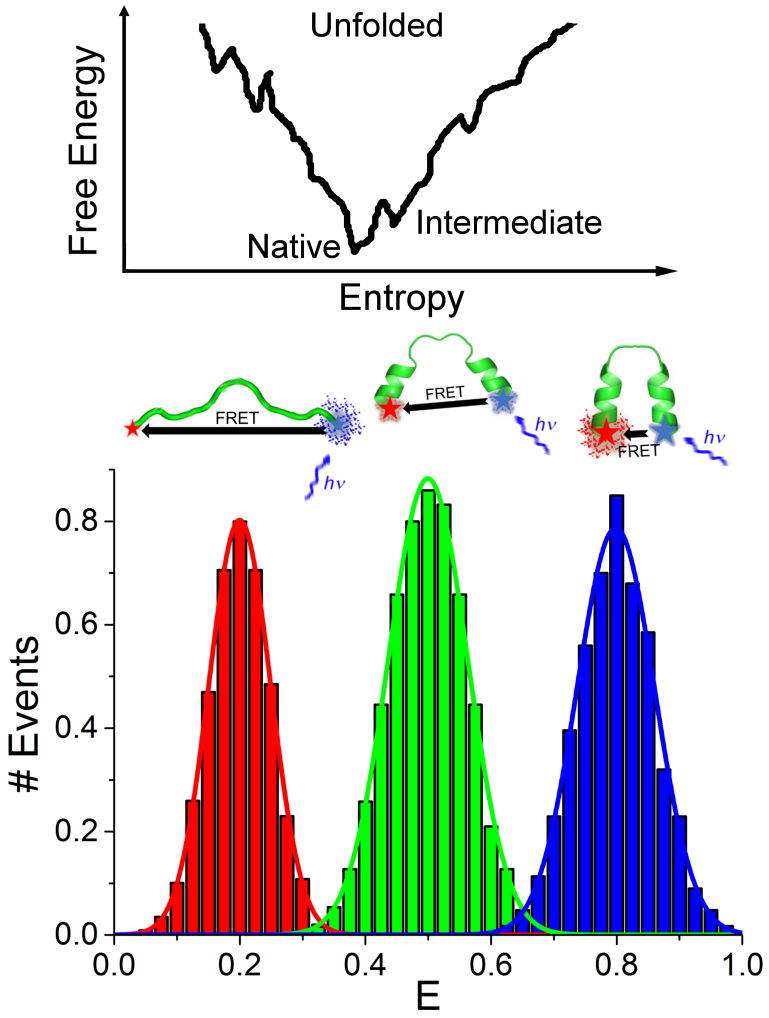

Figure 1.1: Top: Protein folding pathway depicted as one of multiple routes through a rugged, funneled free energy landscape, with a minimum corresponding to the native state and a width representing the conformational entropy [13]. Bottom: Three dimensional structure of a protein in its native (right), an intermediate (middle) and an unfolded state (left). Labeled with donor (blue) and acceptor (red) fluorophore at both ends, the extent of FRET efficiency decreases from the native over the intermediate to the unfolded state. The corresponding transfer efficiency histograms are schematically shown below. Without the functionality of single-molecule FRET, only an average efficiency value would be assessable. Fictional protein structure generated with the help of PDB-files 2n6h and 1AL1 and Pymol.

One of the most powerful techniques in the context of dynamic structural biology is Förster Resonance Energy Transfer, in the following abbreviated as FRET [14–16]. FRET describes the non-radiative transfer of energy from a donor (D) to an acceptor (A) fluorophore, with the efficiency of transfer (E) depending on the so-called Förster radius (R_0) of the employed FRET pair and the distance between D and A. Hence, attaching D and A to specific positions of a (biological) target macro-molecule, FRET can be used as a

spectroscopic nanometer ruler [17]. Demonstrated in ensemble already fifty years ago, due to the required chemical and technical improvements the first single-molecule FRET (smFRET) measurement in solution was performed thirty years later, validating once more the distance-dependency of FRET with the help of fluorescence labeled rigid DNA oligonucleotides [18]. Among others, smFRET was subsequently employed to decipher the folding pathways (see figure 1.1) and conformational dynamics of several proteins [19–27] and proved its capability of macromolecular structural modeling [28–30] and the enlightenment of aggregation processes [31–33].

Focusing on fluorescence intensity based smFRET measurements, the transfer efficiency is calculated burst-wise using the number of photons emitted by the directly excited donor (F_D) and the FRET excited acceptor (F_A). Additionally, excluding confocal volume mismatches, E depends on the wavelength dependent transmission/detection efficiencies $g_{D,A}$ of the setup at hand and the fluorescence quantum yields of D and A, $\phi_{fl,D,A}$ [34]:

$$E = \frac{1}{1 + (\frac{R_{DA}}{R_0})^6} = \frac{F_A}{F_A + \frac{\phi_{fl,A}}{\phi_{fl,D}} \frac{g_A}{g_D} F_D}$$

Obviously, the reliability of the obtained FRET efficiencies and, maybe even more important, the corresponding inter-dye distances (R_{DA}) crucially depend on the precise knowledge of the calibration parameters $g_{D,A}$, $\phi_{fl,D,A}$ and R_0. Here, the Förster radius is determined by the spectral overlap of donor and acceptor, the refractive index of the fluorophore environment, the donor quantum yield and the relative orientation of the transition dipole moments of D and A [34]. As the spectral, photo-physical and electrostatic signature of D and A can vary significantly with the characteristics of the surrounding environment, for instance the refractive index, the viscosity and the polarity [35–37], naturally the FRET calibration parameters should be determined under application relevant conditions. Hence, one aim of this thesis is to accurately determine the needed calibration parameters in the shortest amount of time and to the largest possible extent at (close to) single-molecule concentrations with the help of confocal microscopy.

In this regard, one focus is set on time-resolved anisotropy (TRA) measurements performed with a confocal setup. Commonly, TRA decays are measured with the help of fluorescence spectrometers equipped with a linearly polarized pulsed laser, photo-multiplier tubes and electronics recording the fluorescence intensity of the two orthogonal polarization components at specific delay times after the excitation pulse. The laser light and the fluorescence emission are focused/collected under small angles providing a close to parallel excitation and detection geometry, hence, all standard TRA decay models are adjusted to this situation [38]. As distinct from that, considering confocal microscopes equipped with high numerical aperture objectives, the excitation light is strongly focused and the fluorescence emission collected under large angles, which leads to depolarization artifacts and consequentially the need of setup adapted TRA decay models. Already in the 1970s, Dragsten [39] and Axelrod [40] mentioned high-aperture fluorescence detection depolarization effects in steady-state polarization measurements and derived the mathematical treatment needed to take these into account. About twenty years later, Koshioka et al. focused on time-resolved anisotropy measurements performed with a confocal microscope, facing the

problem of a high aperture detection and excitation geometry. With a more pragmatic approach, they proposed an experimental calibration procedure to adjust the high-aperture parallelly and perpendicularly polarized emission components to the traditional parallel beam emission components with the help of two depolarization correction factors (k_1 and k_2). Shortly after that, Ha et al. presented a theoretical framework for, and an experimental study of the polarization spectroscopy of single, surface-immobilized molecules [41]. Finally, another ten years later, Fisz also derived a complete theoretical prediction of k_1 and k_2, taking into account the high-aperture excitation and detection geometry as well as the Gaussian beam intensity profile [38, 42]. Although the calibration procedure described by Koshioka et al. is in principle straightforward, it has to be taken into account that the temporal resolution of the photo-multiplier tubes employed in their work was around 20 times better than the one of the single-photon avalanche diodes employed in this and other works focusing on single-molecule spectroscopy. To circumvent this problem, in this work an extended measurement protocol is established, using a fluorophore in a whole set of glycerol solutions with increasing refractive indices and viscosities. For each test sample, the depolarization parameters are determined and with the help of a support-plane-analysis [43] the corresponding confidence intervals are calculated, allowing an estimation of the parameter reliability. In combination with the theory of Fisz, a precise determination of the two depolarization correction factors is facilitated. Having adjusted the TRA models to the given confocal setup, the orientation factor κ^2 entering the Förster radius calculation can be assessed.

Another focus is set on the quantum yield determination of the fluorescent markers. Besides its importance for the calculation of FRET efficiencies, the quantum yield can be considered as one of the key parameters characterizing a fluorophore, as it defines to which extent absorbed photon energy is converted into fluorescence emission [43]. Hence, together with the photo-destruction yield, it assesses the suitability of a fluorophore for ultra-sensitive spectroscopy [44, 45]. Nowadays, quantum yields are commonly determined by comparison of the integral fluorescence emission of a sample with unknown quantum yield and a reference sample with known quantum yield under identical measuring conditions for solutions of known optical densities [46–48]. Practically, the set of absorption and emission spectra is obtained by varying the fluorophore concentrations. Thus, only an absorption spectrophotometer and a fluorescence spectrophotometer are needed, which makes this method attractive to many groups. However, to achieve an adequate accuracy with this method, cuvettes with long path length are required resulting in a large sample consumption. In this work, a new method for the quantum yield determination exploiting the advantages of confocal microscopy based Fluorescence Correlation Spectroscopy (FCS) is established. FCS makes use of fluorescence intensity-fluctuations to, for example, determine the diffusion properties, photo-physical characteristics or chemical rate constants of a sample as well as the average number of molecules in the confocal effective volume [49, 50]. The latter can be used to determine the molecular brightness (MB) of a sample, defined as the fluorescence count rate per molecule and time for a specific excitation photon flux and the given setup. Working in a limit of low excitation intensities, the MB is proportional to the underlying sample quantum yield. Hence, comparing

the MB of a reference sample to the MB of a sample with unknown quantum yield, the latter can be assessed.

After a derivation of the needed theoretical framework, the experimental implementation of the new method, further on called liFCS approach, is explained step-by-step. The analysis of FCS curves and the resulting output parameters depend on the assumed shape of the underlying effective volume, which can be approximated by a 3D Gaussian distribution under specific conditions. As most confocal microscopes are equipped with water-immersion objectives, these conditions are most likely fulfilled under design conditions, which correspond to measurements in sample solvents of a refractive index close to the one of water. As distinct from that, using sample solvents with a refractive index value mismatching the default one potentially leads to a significant distortion of the effective volume [51, 52]. Supported by theoretical estimations and validating experiments a measurement protocol erasing the impact of a refractive index mismatch is developed to make the liFCS approach applicable to fluorescent specimen in solvents of arbitrary refractive index. By means of proof-of-principle measurements, the accuracy and precision of the determined quantum yields is evaluated and compared to other approaches. Additionally, it is demonstrated that in combination with fluorescence lifetime measurements, the liFCS approach can be used to determine static and dynamic quenching constants. Another benefit of the liFCS approach is that the needed sample concentrations lie in the sub-nanomolar regime and the required sample volumes in the µl range. This means that also rather complicated biological systems relying on cell-free expression with low yields can be characterized [53, 54], just as samples with a strong, concentration-dependent oligomerisation/aggregation tendency [55]. Additionally, as distinct from other approaches working at close to single molecule sample concentrations, no surface-immobilization of the fluorescent particles and no additional, custom-build devices are required [56–58].

As already mentioned before, the FRET calibration parameters should always be determined under the real measurement conditions, which is directly clear considering the broad range of biophysical experiments conducted under strongly varying solvent properties. For example, coming back to protein (un)folding experiments, concentrations of up to 6 M of the chemical denaturant Guanidine Hydrochloride (GdnHCl) are frequently employed, changing the refractive index n from 1.33 to 1.43 [59]. Simultaneously, the dielectric constant decreases by more than 50 % whereas the viscosity increases by a factor of 1.6 as compared to aqueous buffer [60, 61]. Furthermore, to study B-to-Z-DNA transitions [62], to determine the thermodynamic parameters describing the salt dependent duplex formation of DNA [63] or to evaluate the effect of Hofmeister ions on alpha-helical protein structures [64], salt-concentrations in the molar range have to be used, which implies a decrease of the Debye length and the dielectric constant [65]. In addition, to stabilize samples or elongate the observation time window of smFRET measurements, specific amounts of Glycerol can be added to solutions [66, 67], which has a strong effect on the refractive index and viscosity of the solution [68]. Although providing most interesting insights, the performance of smFRET in the cell is technically challenging and hence only a few realizations of this complicated tasks have been published, see for instance [69–72]. Hence, particularly in the recent past, buffers crowded

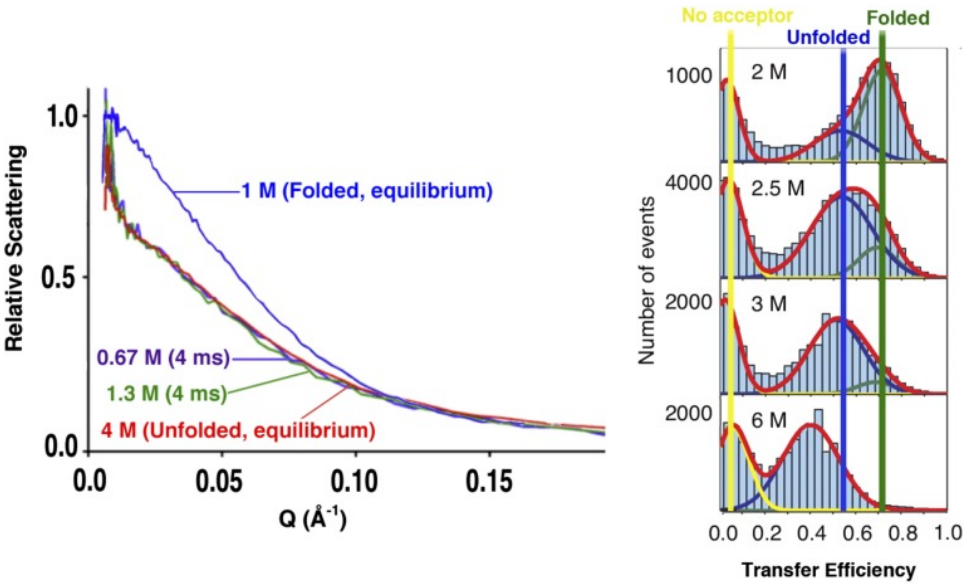

Figure 1.2: Left: Time-resolved small-angle X-Ray scattering profiles of protein L at equilibrium at 1 M (folded), at equilibrium at 4 M GdnHCl (unfolded), and transiently before folding on transfer to denaturant concentrations as low as 0.67 M. Within experimental uncertainty, the scattering profiles of the different unfolded states coincide. This suggests that the unfolded chain does not change its dimensions before folding. Right: Equilibrium smFRET efficiency histograms for fluorescently labeled protein L at varying GdnHCl concentrations. Here, the already unfolded state appears to expand with increasing denaturant concentrations, a process called coil-globule transition. Figure copied from reference [73].

with macro-molecular agents like Polyethylenglycol (PEG), Dextran or Ficoll have been frequently used to artificially mimic the cytosol of the cell [74–80], resulting in changes of the refractive index and of the microscopic viscosity that can be hard to assess [81]. Using so-called crowding sensors, the FRET efficiency observed in an artificially crowded environment is compared to the FRET efficiency observed in the cell to draw conclusions about the cellular interior [82]. Obviously, a large number of experiments are commonly done in additive-enriched aqueous solutions, making the evaluation of possible solvent-induced artefacts in smFRET data a relevant issue extensively treated in this thesis. Another motivation to tackle this question is given by the fact that several comparative studies of GdnHCl induced unfolded states of proteins showed a significant disagreement between smFRET and small-angle X-ray scattering (SAXS) data (see figure 1.2). This raises the question whether the compaction of the unfolded state upon decrease of denaturant concentration (coil-globule transition) observed by smFRET might be a consequence of disregarded calibrations or electrostatic repulsions between the negatively charged fluorescent markers employed in all cases [73, 83, 84]. In summary, the last aim of this thesis is to systematically evaluate the importance of solvent characteristics with respect to smFRET parameters. As a first step, double stranded DNA oligonucleotides are used to assess the importance of electrostatic dye-dye interactions in a distance regime typically considered in protein unfolding measurements. To complement the experimentally obtained inter-dye distances, theoretical predictions taking into account electrostatic dye-dye repulsions are made. Furthermore, aiming to rule out that the discrepancy between scattering and

smFRET measurements of denatured proteins originates from artifacts due to the complex composition of the solution, the impact of denaturant on the two-domain protein Phosphoglycerate Kinase (PGK) is monitored. By eliminating possible artifacts in the inter-dye distance determination, the existence of a coil-globule transition beyond the classical unfolding transition is validated.

Chapter 2

Materials

If not stated otherwise, chemical consumables are purchased from Sigma-Aldrich, St. Louis, USA.

2.1 Fluorophores

- Alexa Fluor 488-C5 maleimide/NHS-Ester (AL488), ThermoFisher Scientific, Waltham, USA
- Alexa Fluor 647-C2 maleimide/NHS Ester (AL647), ThermoFisher Scientific, Waltham, USA
- Fluorescein (FL), Reference dye kit, Life Technologies, Carlsbad, USA
- Atto 655 NHS-Ester (AT655), ATTO-TEC GmbH, Siegen, Germany
- Atto 488 NHS-Ester (AT488), ATTO-TEC GmbH, Siegen, Germany
- Atto 647N NHS-Ester (AT647N), ATTO-TEC GmbH, Siegen, Germany
- Tetraspeck^{TM} Microspheres , 0.1 µm, ThermoFisher Scientific, Waltham, USA

In all measurements using unattached AL488 and AL647, the NHS-Ester variant is used, as it was observed to be more stable concerning its photophysical properties than the unattached maleimide variant.

2.2 Bio-molecules

2.2.1 DNA oligo-nucleotides

Double-stranded DNA (dsDNA) samples were prepared by hybridization of complementary single-strands as described in reference [85].

- Labeled (AL488 or AL647) single strands, Purimex, Grebenstein, Germany
- Unlabeled single strands, Eurofins, Aachen, Germany

The sequences of the single-strands are:

Donor-strand I:

5'- GGA CTA GTC TAG GCG AAC GTT TAA GG**X** GAT CTC TGT TTA

CAA CTC CGA - 3‘

Donor-strand II:

5‘- GGA CTA GTC TAG GCG AAC GTT TAA GGC GAT CTC **X**GT TTA CAA CTC CGA - 3‘

Acceptor-strand:

5‘- TCG GAG TTG TAA ACA GAG ATC GCC TTA AAC G**X**T CGC CTA GAC TAG TCC - 3‘

Here, **X** denotes a thymine nucleobase with a fluorophore bound to its methyl-group via a C6 amino linker. Hybridization of donor-strand I with the acceptor-strand results in a distance of 10 base-pairs in between the dye-attachment points, whereas the hybridization of donor-strand II with the acceptor- strand yields a distance of 17 base-pairs.

2.2.2 Phosphoglycerate Kinase (PGK) from *Saccharomyces cerevisiae*

The production and labeling of single- and double-mutants of PGK is described in detail in reference [86]. In this work, the double cysteine mutant PGK C97S S1C Q135C and the respective single cysteine mutants are employed. In all cases, AL488 and AL647 with a reactive maleimide group are used to site-specifically label the PGK mutants.

2.3 Buffers

2.3.1 DNA buffer

- 20 mM TRIS
- 100 mM NaCl
- 10 mM $MgCl_2$
- pH= 7.5

For the DNA measurements in additive-enriched solutions, the following substances were added to the DNA buffer at a time:

- 1 M NaCl
- 4 M Guanidine Hydrochloride (GdnHCl)
- 50 wt. % Glycerol

The pH was again adjusted to pH=7.5. The concentration of GdnHCl was validated with refractive index measurements [59]. The Glycerol-buffer solution was sealed and stirred at 400 rpm for 30 min at room temperature. The concentration was additionally validated by refractive index measurements [87].

2.3.2 PGK buffer

- 50 mM MOPS
- 50 mM NaCl
- 0.005 % Tween20
- pH= 7.4

For the unfolding experiments, specific amounts of GdnHCl were added. Again, the pH was adjusted to 7.4. The concentrations of denaturant solutions were adjusted by refractive index measurements [59]. Additionally, for the single-molecule FRET measurements a photo-protection cocktail (1 mM Trolox, 10 mM cysteamine) was added.

2.3.3 PBS

- 50 mM Potassium Phosphate
- 150 mM NaCl
- pH= 7.2

2.4 Glycerol solutions

Glycerol solutions used for the calibration of the effective volume needed for Fluorescence Correlation Spectroscopy (FCS) were prepared by adding the specific amounts of Glycerol to ultra-pure water. The solutions were sealed and stirred at 400 rpm for 30 min at room temperature.The viscosities of the glycerol solutions were estimated according to their concentrations [68]. Concentrations were additionally validated by refractive index measurements [87].

2.5 Cover slip surface preparation

For all measurements, precision glass cover slips (No. 1.5H, Marienfeld, Lauda-Königshofen, Germany) are employed.

- Fluorophore measurements: The cover slips are simply cleaned from dust with the help of ultra-pure air or nitrogen.
- DNA sample measurements: The cover slips are cleaned from dust and plasma-cleaned for ten minutes.
- PGK sample measurements: For ensemble measurements, the cover slips are cleaned from dust, plasma-cleaned for ten minutes and subsequently treated with a 10 mg/mL bovine serum albumin solution (incubation time 30 min). After that, they are rinsed with water and dried with nitrogen. With respect to the solutions containing GdnHCl, each cover slip is used for 15 minutes only. For the single-moleculeFRET measurements, the cover slip surfaces are coated with Poly-ethylenglycol (PEG). Further details can be found in reference [86].

2.6 Software

- Fluorescence lifetime decays: Matlab R2015b, Mathworks, Natick, Massachusetts, USA
- Time-resolved anisotropy decays: Matlab R2015b, Mathworks, Natick, Massachusetts, USA
- Single-molecule FRET data: Matlab R2015b, Mathworks, Natick, Massachusetts, USA
- Fluorescence-Correlation spectroscopy: Symphotime64, Picoquant, Berlin, Germany
- Molecular modeling: Pymol 1.7.4.5 Edu, Schrödinger LLC, New York, USA
- Accessible volume calculations (standard): FRET Positioning and Screening (FPS) 1.1, Molecular Physical Chemistry Group, HHU Düsseldorf, Germany
- Accessible volume calculations (expanded): Python-Code by Simón Poblete, Molecular and Statistical Biophysics, SISSA Trieste, Italy

Chapter 3

Instrumentation

3.1 Confocal setup

The Microtime 200 by Picoquant (Berlin, Germany), further on denoted as MT200, is the confocal setup all methodical developments and more elaborate measurements presented in this work are associated with. Hence, as distinct from other instruments used here, it shall be discussed shortly.

The laser combining unit (LCU) is the part of the MT200 where the excitation laser light is coupled into a single mode, polarization maintaining fibre which generates a Gaussian beam shape and directs the light into the main optical unit (MOU). As shown in figure 3.1, it contains four different pulsed diode laser heads (LDH-D-C-440, LDH-D-C-485, LDH-D-C-510, LDH-D-C-640) with optimal pulse widths around 70 to 100 ps. Throughout this work, only two of these laser heads are used, namely the LDH-D-C-485 and the LDH-D-C-640, with excitation wavelength profiles peaked around 481/633 nm in the case of pulsed, and 487/637 nm in the case of continuous excitation. Laser power and frequency are controlled by the PDL-828 Sepia II laser driver, providing repetition rates between 196 kHz and 80 MHz as well as the already mentioned continuous excitation (*cw*) mode. With the help of an array of one mirror and three dichroic mirrors, the excitation light is directed onto a set of controllable neutral filters facilitating its attenuation in discrete (OD-filter wheel) or continuous (scaffold filter) steps. Thereafter, the laser beam gets reflected by another mirror onto the fibre coupler.

Having reached the MOU (see figure 3.2) and being coupled out of the delivery fibre, the excitation light passes an objective to get expanded and collimated. After being reflected by a mirror, the laser beam impinges on a semitransparent mirror so that a small part of it gets deflected onto a photodiode used as an indicator of the light intensity reaching the sample. The other part of the laser beam passing through the semitransparent mirror is directed into the body of an inverted microscope (IX 73, Olympus, Shinjuku, Japan) with the help of a dual-band dichroic mirror (XF2401, Omega Optical, Brattleboro, USA). In the microscope body, the laser beam gets deflected onto the back-aperture of an objective, which is mounted on a piezo-stage movable along three axes at a nominal precision of one nanometer. The properties of the three Olympus objectives employed in this work are summarized in table 3.1. The back aperture radii of all objectives were determined with the help of a caliper. Referring to the default objective used for most of the measurements in this work (UPLSAPO 60XW), the laser beam is focused by the objective and passes a layer of immersion water and a layer of glass (cover slip) before finally reaching the (aqueous) sample solution. Being equipped with a correction collar, the objective can handle

Objective	NA	Magnification	Immersion medium	Back aperture radius [mm]
UPlanFl	0.3	10x	Air	6.0 ± 0.1
UPLSAPO **(default)**	1.2	60x	Water	4.3 ± 0.1
UPlanSAPO	1.35	60x	Oil	5.5 ± 0.1

Table 3.1: Properties of the three objectives used in this work. NA denotes the numerical aperture of the objective.

cover slip thicknesses between 130 and 210 µm. Nevertheless, only precision glass cover slips (No. 1.5H, Marienfeld, Lauda-Königshofen, Germany) with a thickness of (170 ± 5) µm are used here, so the correction collar is fixed to a value of 0.17. To be able to position the laser beam focus on the upper or lower cover slip surface, a CCD camera is incorporated in the MOU which detects and displays the back-reflected excitation light, which is naturally most intense at interfaces between media of different refractive index.

The fluorescence emission of the sample is collected by the same objective used for excitation (epi-fluorescence microscopy). As the fluorescence light is shifted to longer wavelengths than the excitation light, it can pass the major dichroic mirror and gets focused onto the confocal pinhole by a tube lens. The pinhole acts like a spatial filter along the beam propagation axis, with the degree of filtering depending on its diameter and the numerical aperture (NA) of the objective. Here, a pinhole diameter of 30 µm is used for all Fluorescence correlation spectroscopy (FCS) applications, whereas a larger pinhole (d= 75 µm) is employed for all Förster resonance energy transfer (FRET) measurements.

Having passed the pinhole, the emission light gets expanded by another lens and is deflected by a mirror onto a tower containing several, adjustable optical elements. With respect to FCS measurements, the light signal is split into two (approximately equal) fractions with the help of a beam-splitting cube (Olympus Deutschland, Hamburg, Germany). Referring to FRET measurements, a minor dichroic mirror (620 dcxr, Chroma Technology, Vermont, USA) is employed to direct the signal of the donor emission in the direction of one detector and the signal of the acceptor emission to the other. In terms of time-resolved anisotropy measurements (TRA), a polarizer cube (Linos Photonics, Goöttingen, Germany) is used, whereas concerning other techniques the emission light simply passes the tower. In any case, depending on its wavelength, the fluorescence light passes an appropriate emission filter (FF01 530/55 or ET658/80 M, Semrock, Rochester, USA) before impinging on the active area of the two detector units (τ-SPADs, Picoquant, Berlin). Subsequently, the detected signal is processed by Time-correlated Single Photon Counting (TCSPC) electronics (Picoharp 300, Picoquant, Berlin) working in Time-Tagged Time Resolved (TTTR)-mode.

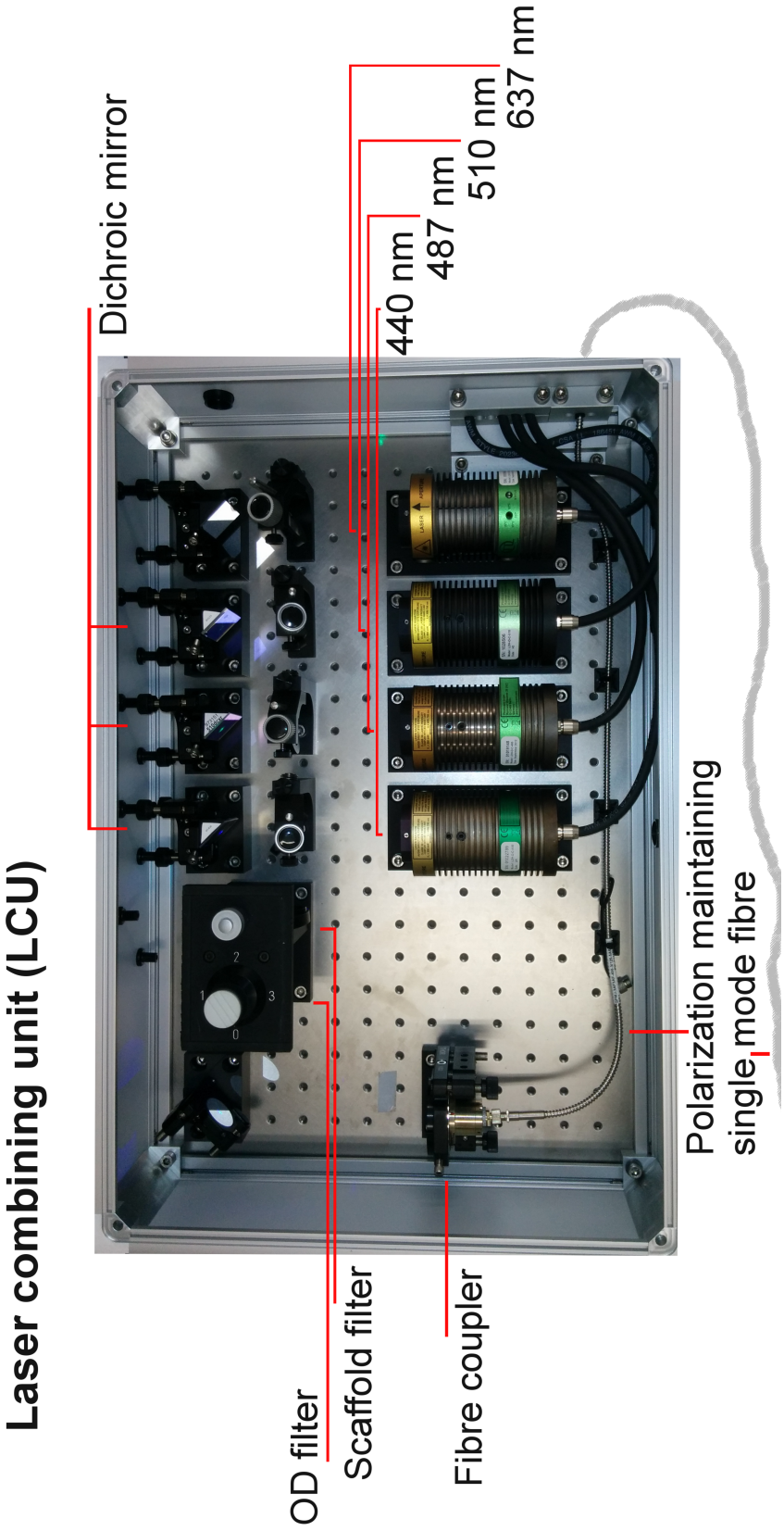

Figure 3.1: Top view on the MT200 laser combining unit (LCU); raw photo provided by N.Junker

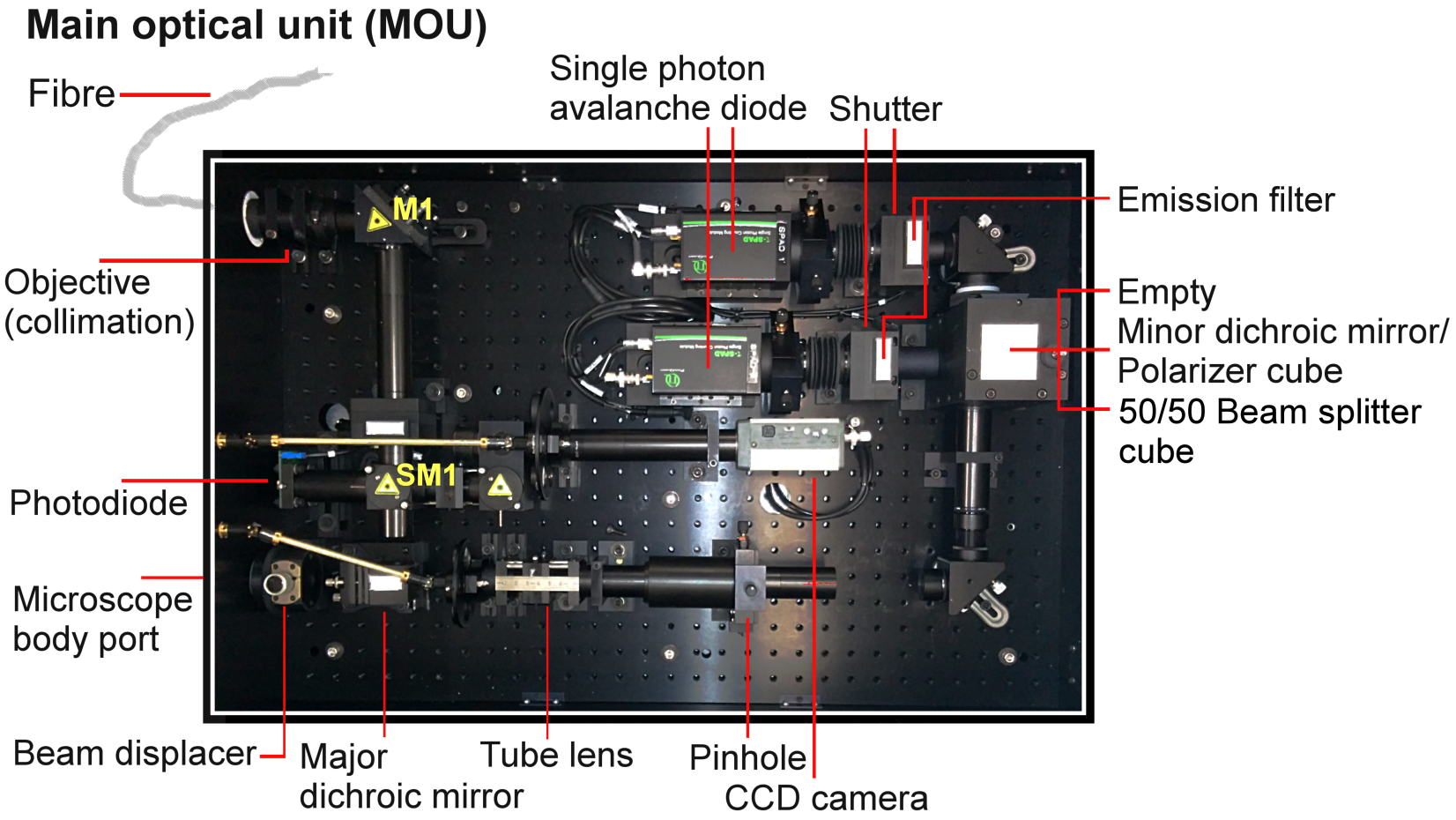

Figure 3.2: Top view on the MT200 main optical unit (MOU); raw photo provided by N.Junker

3.2 Other instruments used in this work

- Plasma cleaner: PDC-32G, Harrick Plasma, Ithaca, USA
- Absorption spectrometer: UV-2600, Shimadzu, Kyoto, Japan
  Cuvette: 104F-QS, Hellma, Mühlheim, Germany, 1 cm
  Cuvette: 104-QS, Hellma, Mühlheim, Germany, 5 cm
- Fluorescence spectrometer: QuantaMaster40, PTI, Birmingham, USA
  Cuvette: 105.253-QS, Hellma, Mühlheim, Germany, 10x2 mm
- Abbe refractometer: AR4, A. Krüss Optronic, Hamburg, Germany
- pH-meter: SevenCompact, Mettler Toledo International Inc., Columbus, OH, USA
- Beam diagnostic tool: Beamage 3.0, Gentec Electro-Optics, Quebec, Canada

Chapter 4

Theory and methods

4.1 Fluorescence

In the followings sections, a brief outline of the fundamentals of fluorescence and some related measurement techniques will be given.

Neglecting hot body radiation, all forms of light emission are summarized under the term luminescence. Furthermore, luminescence can be grouped into the two categories of fluorescence and phosphorescence. To explain these two phenomena in more detail, a so-called Jablonski diagram, shown in figure 4.1, has proved to be useful.

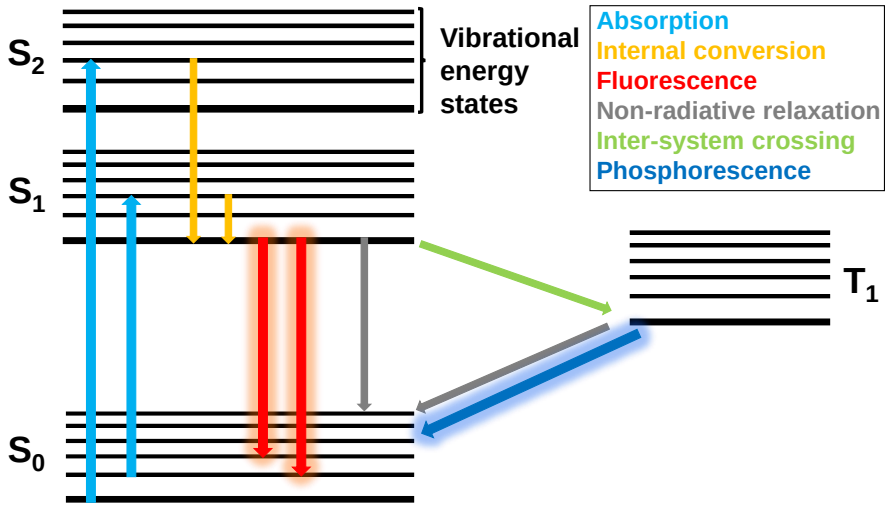

Figure 4.1: Jablonski diagram illustrating processes of fluorescence, phosphorescence and other (de-)excitation pathways: Photon absorption induces transition from ground state (S_0) to one of the higher vibrational energy sub-levels (narrow horizontal black lines) of first (S_1) or second (S_2) excited singlet state (light blue arrow). Internal conversion causes relaxation to lowest vibrational level of S_1 (orange arrow). Molecule returns to one of the higher vibrational levels of ground state by radiative (fluorescence, red arrow) or non-radiative relaxation (gray arrow). Transition from first excited singlet to first excited triplet state (T_1) is called inter-system crossing (green arrow). Upon phosphorescence emission, the molecule returns to ground state (dark blue arrow).

Through the (instantaneous) absorption of a photon, a molecule transitions from the ground state into one of the higher vibrational energy sub-levels of the first or second excited electronic state. From there, it rapidly (picoseconds) relaxes back to the lowest vibrational sub-level of the first excited state, a process that is called internal conversion. Upon return into

one of the higher vibrational levels of the ground-state, a fluorescence photon can be emitted. Comparing the energy differences linked to absorption and fluorescence, it gets clear that absorption takes place at higher photon frequencies than fluorescence, a phenomenon also called Stokes-Shift. Competitively to the emission of a fluorescence photon, non-radiative relaxation to the ground-state can take place.

An alternative to the radiative or non-radiative return to the ground-state is the process of inter-system crossing from the first excited singlet to an excited triplet state, a transition that is accompanied by a spin-flip. The radiative return from the excited triplet to the ground state is called phosphorescence. Comparing fluorescence and phosphorescence, it is important to mention that the transition from the first excited singlet state to the ground is spin-allowed, whereas the transition from the first excited triplet state to the ground state is not. Hence, fluorescence emission rates lie around 10^8 per second, while phosphorescence emission rates lie in the range between one and 10^6 per second depending on the considered system [43].

4.1.1 Fluorescence lifetime

One of the most important parameters characterizing a fluorescent molecule is its fluorescence lifetime, further on abbreviated as τ_{fl}. It is defined as the average time a molecule spends in the excited singlet state before emitting a fluorescence photon, and can be derived using a simple rate equation [43]:

$$\dot{N}_{S1}(t) = -k_{10} N_{S1}(t) + f(t) \tag{4.1}$$

Here, $N_{S1}(t)$ equals the number of molecules that are in the excited state at time t, and k_{10} is an effective rate taking into account all de-excitation pathways from the first excited singlet state to the ground-state. f(t) is a function describing the time-course of excitation. Assuming that the measurement starts directly after the excitation source has been switched off, the situation typically given when using a short excitation laser pulse, equation 4.1 turns into:

$$\dot{N}_{S1}(t) = -k_{10} N_{S1}(t) \tag{4.2}$$

with its solution given by:

$$\begin{aligned} N_{S1}(t) &= N_{S1,0} \exp\left(-t k_{10}\right) \\ &= N_{S1,0} \exp\left(-\frac{t}{\tau_{fl}}\right) \end{aligned} \tag{4.3}$$

Here, $N_{S1,0}$ is the number of excited molecules at the time of excitation. Obviously, the number of excited molecules decays exponentially with time, with the fluorescence lifetime being the time at which 63 % of the population of initially excited molecules have returned to the ground state.

Time-correlated single-photon counting (TCSPC) histograms

To determine fluorescence lifetimes experimentally, the sample gets periodically excited by a short laser pulse. The time between two consecutive pulses is divided into bins of equal size, also called time-channels. With the help of single-photon sensitive detectors and time-correlated single photon

counting (TCSPC) electronics, each detected fluorescence photon is assigned to a specific time-channel. In other words, the photon arrival time with respect to the time of excitation is determined, which is then used to build a so called TCSPC-histogram. This process is also schematically sketched in figure 4.2. As only molecules in the excited state are able to emit fluorescence

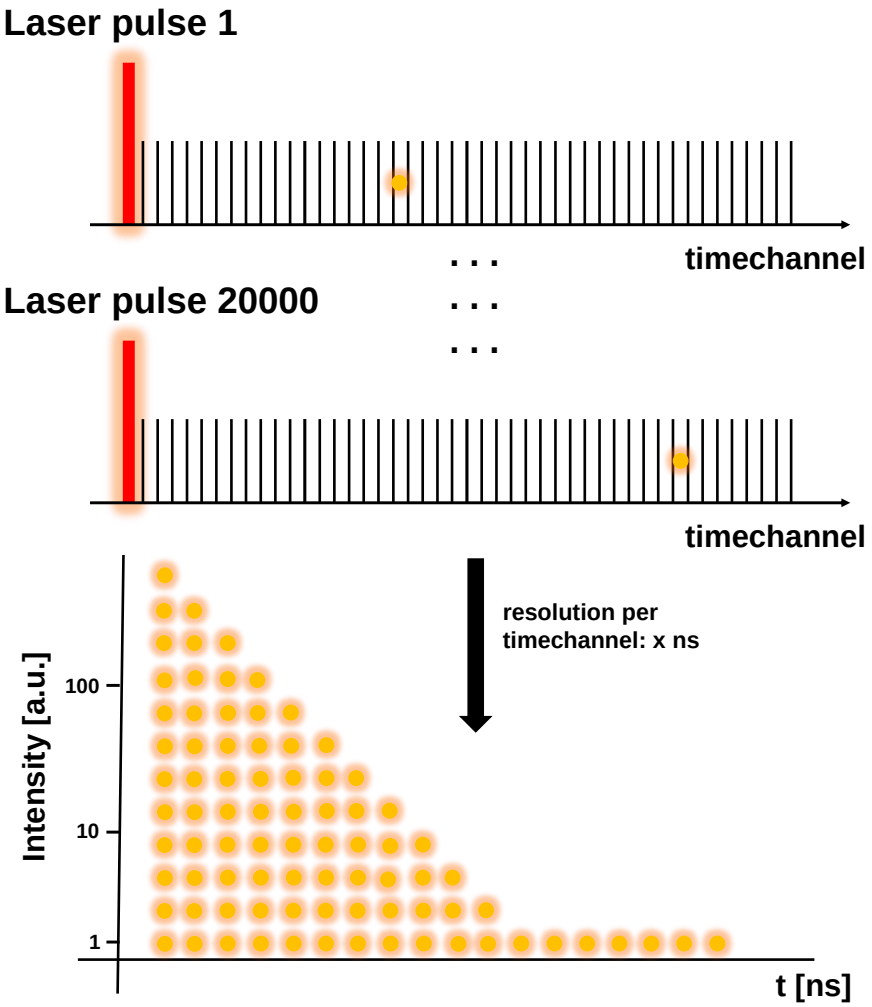

Figure 4.2: Top and center: A short laser pulse periodically excites a sample. During an excitation cycle, a detected fluorescence photon is assigned to a specific time-channel. The resolution per time-channel determines the real arrival time after the excitation pulse. Bottom: After many excitation cycles (indicated by 20000 here), the corresponding TCSPC histogram can be used to determine the fluorescence lifetime (distribution) of a sample.

photons, the probability to detect a photon in a specific time-channel after excitation is proportional to the number of molecules still excited at that time. Hence, the TCSPC-histogram reflects the exponential decay given in equation 4.3 and, by fitting a suitable model equation to it, can be employed to determine τ_{fl}. Considering mixtures of fluorophores or fluorophores sensing a heterogeneous environment, in many cases the measured lifetime decay is multi-exponential [43]:

$$I_{fl}(t) = \sum_{i=1}^{N} a_i \exp\left(-\frac{t}{\tau_{fl,i}}\right) \tag{4.4}$$

Here, the intensity $I_{fl}(t)$ equals the number of photons per time-channel/arrival time. The parameter a_i denotes the amplitude of the lifetime decay of the particular fluorescent species and is proportional to the number of excited molecules and the effective emission rate of the species. If useful, an average fluorescence lifetime can be calculated according to [43]:

$$\bar{\tau}_{fl} = \sum_{i=1}^{N} \frac{a_i \tau_{fl,i}^2}{a_i \tau_{fl,i}} \tag{4.5}$$

Pile-up

Experimentally, it is important that the concentration of the sample or the applied excitation intensity are adjusted in such a way that per excitation cycle (at most) only one fluorescence photon is detected. At higher emission rates, due to the dead time of the TCSPC device (typically lying in the range of 25 to 90 ns here), only the first of a number of photons would be detected. This so-called pile-up effect leads to apparently shorter fluorescence lifetimes and converts a mono-exponential into a bi-exponential lifetime decay [43]. In this work, applying an excitation frequency of 20 MHz in all cases, the average count rate was kept below 100 kcounts/s during all measurements.

The instrument response function (IRF)

It should also be mentioned that the detection system has a specific instrument response function (IRF) biasing the measured TCSPC histogram. Its influence can be corrected for by determining the IRF, convoluting the model function with it and fitting the resulting curve to the measured lifetime decay (also called iterative re-convolution) [43].

The IRF is determined by simply measuring the TCSPC histogram generated by a scattering solution. This obviously has the disadvantage that the IRF is measured at a different wavelength than the actual sample, which might be problematic if the detection system has a wavelength dependent timing response. A particularly convenient way to circumvent this problem is to quench a fluorophore, lying in the same spectral range as the sample of interest, with the help of a saturated potassium iodide solution and measure the corresponding TCSPC histogram [88]. Due to the short lifetime of the quenched dyes, the emitted photons impinge on the detection system in a time-window corresponding approximately to the full width at half maximum (FWHM) of the IRF. Assuming an average count rate of 10 kcounts/s, an excitation frequency of 20 MHz and a FWHM of 500 ps, the real photon detection rate lies around 10 Mcounts/s. This results in pile-up and consequently a distorted shape of the acquired IRF. To circumvent this problem and to obtain coincident real photon detection rates during the sample and the IRF measurement, the IRFs were measured at an average count rate of 1000 counts/s. To obtain the desired precision, an IRF peak value of 10000 counts was achieved in all cases.

The optimal fitting parameters are obtained by the non-linear least squares minimization of the goodness-of-fit parameter χ^2_{red}, defined as [43]:

$$\chi^2_{red} = \frac{1}{N-P} \sum_{i=1}^{N} \frac{(I_{fl}(t_i) - D(t_i))}{\sigma(t_i)^2} \tag{4.6}$$

Here, N is the number of data points and P is the number of fitting parameters. The measured photon counts in time-bin i are denoted as $D(t_i)$, whereas the corresponding photon counts predicted by the model function are given by $I_{fl}(t_i)$. The parameter $\sigma(t_i)$ is the standard deviation of the photon counts in time bin i.

4.1.2 Fluorescence quantum yield

The fluorescence quantum yield, further on abbreviated as ϕ_{fl}, is another important characteristic of a fluorescent molecule. It describes to which extent a molecule converts absorbed light into fluorescence emission [43]:

$$\phi_{fl} = \frac{k_{fl}}{k_{10}} = \frac{\tau_{fl}}{\tau_n} \tag{4.7}$$

Here, k_{fl} is the fluorescence emission rate and k_{10} the already mentioned effective emission rate. The parameter τ_n is the inverse of the fluorescence emission rate and is called the natural lifetime of a fluorophore.

Quantum yield determination: standard approach

A commonly employed approach to determine ϕ_{fl} is based on plotting the integrated fluorescence intensity of the sample with unknown quantum yield and the integrated fluorescence intensity of a reference sample with known quantum yield against the respective optical density at the excitation wavelength. By comparison of the slopes of the two linear curves, the unknown quantum yield is determined according to [46–48]:

$$\phi_{fl,s} = \frac{m_r}{m_s}\frac{{n_r}^2}{{n_s}^2}\phi_{fl,r} \tag{4.8}$$

Here, the subscript r denotes the reference and the subscript s the sample of interest, whereas m is the slope of the curves. The refractive index is named n.

To circumvent problems due to the inner filter effect, the optical densities of sample and reference (at and above the excitation wavelength) have to be kept below ≈ 0.05 per cm of cuvette path length. Consequently, to obtain adequate signal-to-noise ratios in the absorption measurements, cuvettes with long path lengths (5 cm in this work) have to be used [43, 89].

4.1.3 Absorption: The Lambert-Beer law

Absorption is the prerequisite for fluorescence occur, hence this short section dealing with the Lamber-Beer law is classified as a sub-section within the field of fluorescence for convenience.

Considering a cuvette containing a solution of absorbers irradiated by light of intensity I, the differential equation describing the amount of light (dI) that is absorbed per thickness (dx) is given by [43]:

$$\frac{\mathrm{d}I}{\mathrm{d}x} = -IN\sigma \tag{4.9}$$

Here, σ is the absorption cross-section, N is the number of absorbers per cm^3. The solution of equation 4.9 is given by [43]:

$$\ln\left(\frac{I_0}{I}\right) = N\sigma d \tag{4.10}$$

$$\log\left(\frac{I_0}{I}\right) = OD = \epsilon c d \tag{4.11}$$

Equations 4.10 and 4.11 are alternative formulations of the so-called Lambert-Beer law, whereas equation 4.11 is the more common one. Here, I_0 denotes the light intensity at x=0 (boundary condition), ϵ is the molar absorption coefficient, c is the sample concentration and d the sample thickness (or cuvette path length). The abbreviation OD stands for the optical density of the sample. Combining equations 4.10 and 4.11, the relationship between the absorption cross-section and the molar absorption coefficient is obtained:

$$\sigma = 3.82 \cdot 10^{-21}\epsilon \tag{4.12}$$

Here, σ is given in cm^2 and ϵ in $M^{-1}cm^{-1}$.

4.2 Single-molecule FRET (smFRET) measurements

4.2.1 FRET theory in a nutshell

Already in the beginning of the 20th century, it was observed that the fluorescence emission of viscous solutions of fluorophores, previously excited with linearly polarized light, showed a decrease of polarization with increasing fluorophore concentration (see figure 4.3) [90]. It was concluded

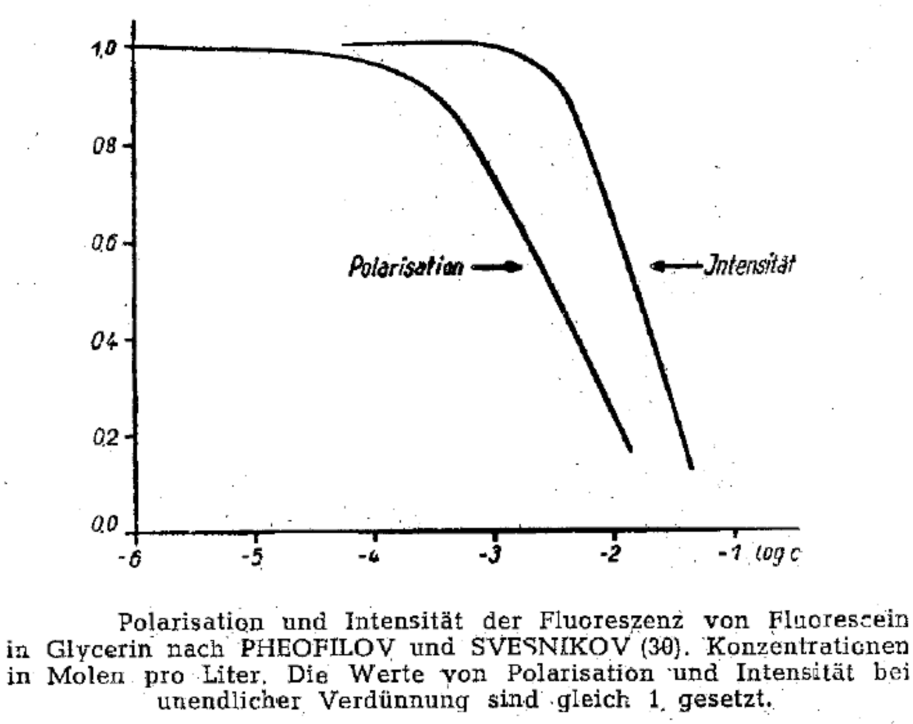

Polarisation und Intensität der Fluoreszenz von Fluorescein in Glycerin nach PHEOFILOV und SVESNIKOV (30). Konzentrationen in Molen pro Liter. Die Werte von Polarisation und Intensität bei unendlicher Verdünnung sind gleich 1 gesetzt.

Figure 4.3: In a viscous medium, the polarization of fluorophores excited with linearly polarized light decreases upon increasing fluorophore concentration. Already noticed around 1900, the observed phenomenon led to the assumption that the excited molecules transferred a part of their energy to surrounding, differently oriented molecules. Figure taken from one of the first papers of Theodor Förster dealing with resonance energy transfer [14].

that the molecules in the excited state transferred a part of their energy to surrounding, differently oriented molecules, thereby reducing the effect of photo-selection and the polarization of the fluorescence emission. Having ruled out that other processes (like the direct re-absorption of fluorescence photons, collisions or the generation of associated molecule complexes) were sufficient to explain the observed extent of depolarization, it was inferred by Francis and Jean B. Perrin that the energy transfer could be caused by a direct electromagnetic interaction between the excited molecules and adjacent energy acceptors [91–93]. A correct description of the energy transfer mechanism and a precise quantification of its extent was accomplished by Theodor Förster in two seminal papers, the first one containing a classical, and the second one containing a quantum-mechanical derivation of the process [14, 15]. Consequently, the observed phenomenon was named Förster Resonance Energy Transfer or FRET.

In the following, only an outline of a classical derivation of FRET will be given. As mentioned before, FRET is the transfer of energy from an excited

donor molecule to an acceptor molecule in the ground state, mediated by the electromagnetic coupling of both molecules. Therefore, the first step is to consider the electric field of the excited donor molecule, the latter visualized as a group of electrons oscillating around a stationary nucleus in response to an external electromagnetic perturbation. The generated electric field is rather complex, but can be significantly simplified by considering specific distance regimes. As was shown by the already mentioned experiments on concentration depolarization [90], FRET is limited to a distance regime larger than the spatial extent of the donor and much smaller ($\approx$ 1-10 nm) than the wavelength of the light used to excite it. The real part of the electric near-field of an excited molecule, treated as an ideal dipole emitter, has the same form as the field of a static electric dipole with an oscillatory term added [94]:

$$\vec{E}(\vec{R}_{DA}, t) = \frac{1}{4\pi\epsilon_0 n^2 {R_{DA}}^3}[3(\vec{\mu}_D\hat{R}_{DA})\hat{R}_{DA} - \vec{\mu}_D]\cos(\omega_D t) \tag{4.13}$$

Here, $\vec{\mu}_D$ denotes the dipole moment of the donor fluorophore transferring its energy. $\vec{R}_{DA}$ is the distance vector pointing from the donor to the position of interest, in this case certainly the position of the acceptor molecule. Obviously, $\hat{R}_{DA}$ is the corresponding unit vector. The refractive index of the medium surrounding donor and acceptor is denoted as n, the vacuum permittivity is abbreviated by ϵ_0 and the excited state circular frequency is termed ω_D.

As a next step, the acceptor molecule is also treated as an ideal dipole with a dipole moment $\vec{\mu}_A$ and a natural circular frequency ω_A. According to Newton's second law, a net force on a charge q_e with a mass m_e results in an acceleration of the latter [94]:

$$\ddot{x} = -\omega_A^2 x + \frac{q_e}{m_e} E_A(\vec{R}_{DA})\cos(\omega_D t) \tag{4.14}$$

Here, $E_A(\vec{R}_{DA})$ denotes the component of the electric field of the donor parallel to $\vec{\mu}_A$:

$$E_A(\vec{R}_{DA}) = \vec{E}(\vec{R}_{DA}) \cdot \vec{\mu}_A \tag{4.15}$$

The solution of equation 4.14 is given by [94]:

$$x(t, \vec{R}_{DA}) = \frac{q_e E_A(\vec{R}_{DA})}{m_e(\omega_A^2 - \omega_D^2)}(\cos(\omega_D t) - \cos(\omega_A t)) \tag{4.16}$$

The overall energy transferred to the acceptor corresponds to the sum of its potential and its kinetic energy. Assuming that donor and acceptor frequency are close to each other (resonant), it is given by [94]:

$$U_A = \frac{q_e^2 E_A^2(\vec{R}_{DA})}{8m_e} t^2 \tag{4.17}$$

For convenience, an orientation parameter κ can be defined as:

$$\kappa = \hat{\mu}_A \cdot \hat{\mu}_D - 3(\hat{\mu}_A \cdot \hat{R}_{DA} \cdot \hat{\mu}_D \cdot \hat{R}_{DA}) \tag{4.18}$$

Then, the insertion of equation 4.13 into equation 4.17 leads to the following expression for the energy passed from a donor to an acceptor molecule [94]:

$$U_A = \frac{q_e^2 \mu_D^2 \kappa^2 t^2}{8 m_e (4\pi\epsilon_0)^2 n^4 {R_{DA}}^6} \propto \frac{\kappa^2}{{R_{DA}}^6 n^4} \tag{4.19}$$

Having a look at equation 4.19, three important features of the extent of the transferred energy become clear: (i) it depends inversely on the sixth power of the distance between donor and acceptor; (ii) it varies strongly with the mutual orientation of the donor and acceptor dipole moments, which finds expression through the the factor κ^2; (iii) it also depends inversely on the fourth power of the refractive index of the solvent. Another important aspect not yet considered are the distributions of the natural oscillation frequencies of the excited state of the donor and the ground state of the acceptor. Without going into detail here, it is clear that both distributions have to overlap to some extent to facilitate resonant oscillations and thereby energy transfer.

Having obtained a rough picture of the dipole-dipole coupling leading to FRET, only the final equations needed further on will be given in the following. Differentiating the acceptor energy with respect to time, it is possible to obtain a rate equation describing the rate of energy transfer, which is given by [94]:

$$k_{FRET} = \frac{1}{\tau_D} \left(\frac{R_0^6}{{R_{DA}}^6} \right) \tag{4.20}$$

Here, τ_D is the lifetime of the donor without quenching by the acceptor due to FRET. R_0 is the so-called Förster radius, which is the distance at which the effective emission rate of the isolated donor equals its energy transfer rate to the acceptor. It is defined as [94]:

$$R_0^6 = \frac{9000 \ln(10) \kappa^2 \phi_{fl,D} J}{128 \pi^5 n^4 N_A} \tag{4.21}$$

Here, $\phi_{fl,D}$ denotes the donor quantum yield, N_A is Avogadro's constant and J is the overlap integral related to the oscillation frequency distributions of donor and acceptor. It is calculated according to [94]:

$$J = \int f_D(\lambda) \epsilon_A(\lambda) \lambda^4 d\lambda \tag{4.22}$$

The area normalized fluorescence emission spectrum of the donor is termed $f_D(\lambda)$, whereas the peak normalized absorption spectrum of the acceptor is multiplied with its molar absorption coefficient to obtain $\epsilon_A(\lambda)$. If the wavelength is expressed in nm, the Förster radius defined by equation 4.21 is given in $\mathring{A}$. It should be mentioned that the experimentalist can mainly influence the Förster radius by choosing a specific pair of fluorophores as donor and acceptor, thereby increasing or decreasing the spectral overlap integral and the quantum yield of the donor. The other parameters are either dictated by the solvent/molecule, as in the case of the refractive index n, or are rather hard to predict *a priori* like the orientation factor κ^2.

At last, the transfer efficiency, a parameter relating the Förster radius and the actual donor-acceptor distance, is defined as [34, 94]:

$$E = \frac{k_{FRET}}{k_{FRET} + \frac{1}{\tau_D}} \tag{4.23a}$$

$$= \frac{1}{1 + (\frac{R_{DA}}{R_0})^6} \tag{4.23b}$$

In figure 4.4 (a), the transfer efficiency is plotted as a function of the FRET-rate. The donor-only lifetime is assumed to be τ_D= 4 ns, consequently a

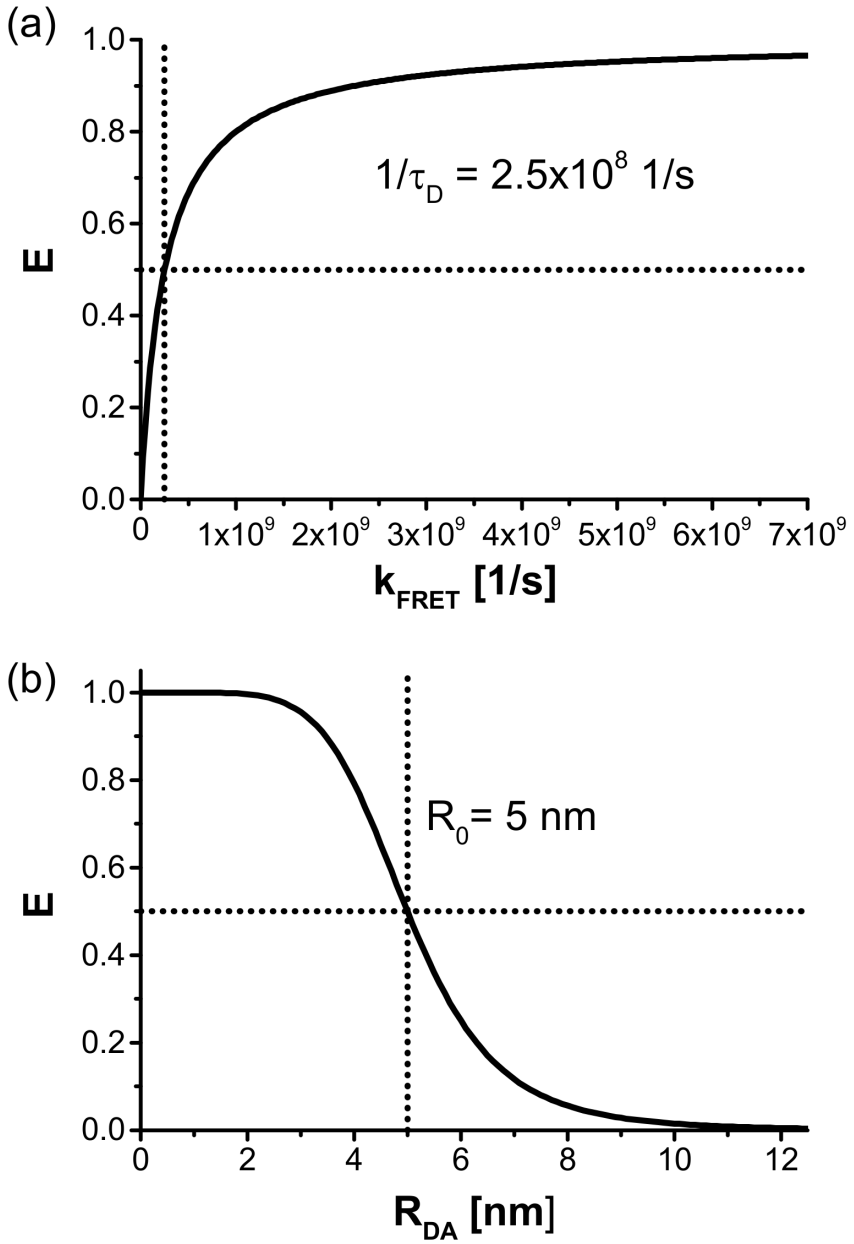

Figure 4.4: (a) Transfer efficiency E as a function of FRET rate k_{FRET} (donor only lifetime τ_D= 4 ns). At $k_{FRET}=1/\tau_D$, a transfer efficiency of 50 % is reached (intersection of black dotted lines). (b) Transfer efficiency E as a function of the donor-acceptor distance: a transfer efficiency of 50 % is reached at the Förster radius R_0= 0.5 nm (intersection of black dotted lines).

FRET-rate equal to its inverse leads to a transfer efficiency of 0.5 (indicated by the intersection of the dotted black lines). Additionally, in figure 4.4 (b) the transfer efficiency is plotted as a function of the donor-acceptor distance, with an assumed Förster radius of 5 nm. A donor-acceptor distance equal to the Förster radius leads to a transfer efficiency of 0.5 (again indicated by the intersection of the dotted black lines). Obviously, for distances close to the Förster radius the transfer efficiency reacts most sensitive to distance changes. In terms of a rational design of a FRET experiment, this has to be taken into account to select the most reasonable donor-acceptor fluorophore pair providing a Förster radius suitable for the specimen at hand.

4.2.2 Confocal single-molecule spectroscopy in solution

As its name implies, single-molecule fluorescence spectroscopy addresses the interaction of electromagnetic radiation with a solitary fluorescent particle. Therefore, one needs to detect the fluorescence emission of only one molecule at a time. Naturally, considering a sample droplet containing multiple diffusing molecules, this means that either the distribution of photons used for excitation, or the collection of emitted fluorescence photons, or both, are spatially limited to a sufficiently small volume. How small this so-called molecule detection function (MDF) volume exactly has to be, is a question of the sample concentration, as is depicted in figure 4.5. Considering an average

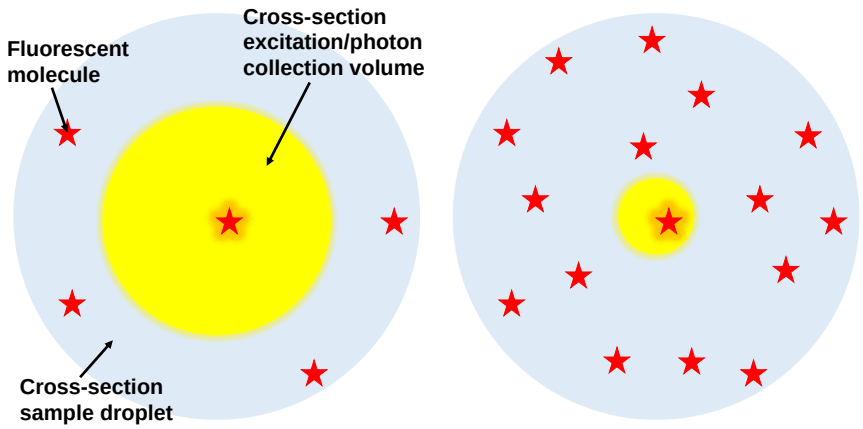

Figure 4.5: Left: Measuring a highly diluted sample opens up the possibility to use a large MDF volume and to still observe one molecule at a time. Right: Shrinking the MDF volume facilitates single-molecule measurements at higher sample concentrations. Single-molecule measurements in solution are based on an adaptation of the concentration of a sample to the given optical measurement conditions.

sample concentration of one nano-molar, approximately 10^{14} molecules are distributed in a volume of one liter. Accordingly, the average volume one molecule occupies is in the femto-liter regime, which means that the MDF volume should also lie in this range. Obviously, the minimal size of the MDF volume is limited by the optical setup in use, whereas the further dilution of a sample is technically always achievable as long as specific biological questions don't put a lower limit on the acceptable sample concentration range [95].

One molecule at a time: the Poisson distribution

As mentioned before, single-molecule measurements require that at all times (at the most) one molecule resides in the MDF volume. Maybe counter-intuitive, that means that the average number of fluorescent particles in the volume has to be significantly smaller than one. This is due to the fact that the actual number of molecules in the MDF volume follows a Poisson distribution, as derived in the following in two dimensions (all results are directly transferable to the three-dimensional equivalent).

As a first step, a cross-sectional area through a sample droplet is considered, further on abbreviated as A. In this area A, a number of N particles are distributed (see figure 4.6, left). As a next step, the area A is divided

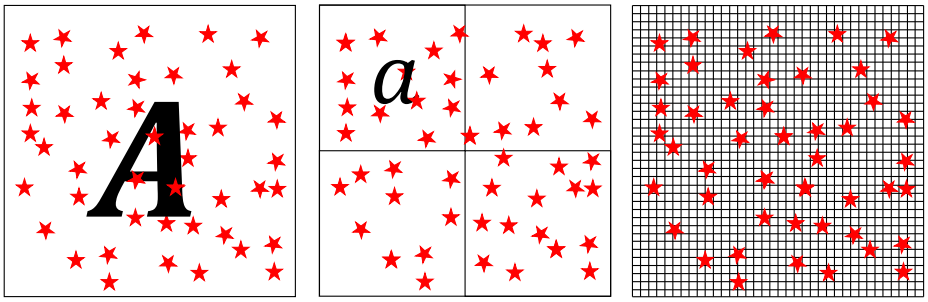

Figure 4.6: The actual number of molecules in the MDF volume follows a Poisson distribution. Left: Cross section through sample volume of area A with N specimen. Center: A is divided in equal compartments of area a with n specimen inside. The probability to find n specimen in one compartment is described by a binomial distribution. Right: Significantly decreased compartment size, resulting in a much larger number of subunits. Probability to find n molecules in one compartment is described by a binomial distribution in the limit of large N and A, approximated by a Poisson distribution.

into equally sized compartments of smaller area a (see figure 4.6, center). As before, the particle density ρ equals N/A. The probability to find n particles in one compartment, is then described by a Binomial distribution [96]:

$$p(n) = \binom{N}{n} \cdot \left(\frac{a}{A}\right)^n \cdot \left(\frac{A-a}{A}\right)^{N-n} \tag{4.24}$$

Going one step further, the area A is divided into a larger number of smaller compartments, again containing an area a (see figure 4.6, right). The particle density ρ still equals N/A. Now, the number of molecules per compartment,n , is now much smaller than the overall number of particles N. Additionally, a is very small as compared to the whole area A. This is exactly the setting of a single molecule measurement, with the MDF volume being equivalent to one compartment. Ergodicity given, averaging the number of particles in one specific compartment over time (experimental situation) will lead to the same result as averaging over all compartments observed at one fixed point in time (sketched situation). However, in the considered case, the probability to find n molecules in one compartment is given by the

binomial distribution, but now in the limit of very large N and A [96]:

$$\begin{aligned}\lim_{N,A\to\infty} p(n) &= \binom{N}{n}\cdot\left(\frac{a}{A}\right)^n\cdot\left(\frac{A-a}{A}\right)^{N-n}\\ &= \frac{N^n}{n!}\cdot\left(\frac{a}{A-a}\right)^n\cdot\left(1-\frac{a}{A}\right)^N\\ &= \frac{N^n}{n!}\cdot\left(\frac{a\rho}{N}\right)^n\cdot\left(1-\frac{a\rho}{N}\right)^N\\ &= \frac{(a\rho)^n}{n!}\cdot\exp(-a\rho)\\ &= \frac{\bar{n}^n}{n!}\cdot\exp(-\bar{n})\end{aligned} \tag{4.25}$$

Here, $\bar{n}$ denotes the average number of molecules in one compartment. Having a closer look at the last line of equation 4.25, it gets clear that the Binomial distribution has been transformed into a Poisson distribution. With a given $\bar{n}$, it can be used to calculate the probability to find more than one molecule in the excitation/photon collection volume:

$$p(n>1,\bar{n}) = 1 - p(0,\bar{n}) - p(1,\bar{n}) \tag{4.26}$$

For $\bar{n}$=1, the probability to find more than one molecule at a time in one compartment lies around thirty percent, whereas it lies below one permille for $\bar{n}$ around 0.03. Therefore, $\bar{n}$=0.03 is used as a benchmark throughout all single-molecule measurements in this work. It is adjusted with the help of Fluorescence Correlation Spectroscopy (FCS), a technique discussed in section 4.3.

The molecule detection function (*MDF*)

Having considered a few basics vital in every single-molecule measurement, the next step is to consider how the abstract MDF volume is experimentally implemented in the case of confocal microscopy. The spatial confinement of the excitation photons is achieved by employing a Gaussian laser beam that is focused with the help of a high numerical aperture (NA) objective. Assuming that the back aperture of the objective is under-filled and no aberrations occur, the intensity profile of the focused beam is Gaussian in the plane perpendicular to the beam propagation axis and Lorentzian along the latter [97, 98]:

$$I(r,z) = I_0\cdot\left(\frac{\omega_0}{\omega(z)}\right)^2\cdot\exp\left(-\frac{2r^2}{\omega(z)^2}\right) \tag{4.27}$$

Here, the beam propagation axis is chosen to coincide with the z-axis. Keeping z fixed, the parameter $\omega(z)$ denotes the radial distance from the beam propagation axis where the ratio of the intensity to the amplitude of the distribution equals 13.5 %. It depends on the z-position according to [98]:

$$\omega(z) = \omega_0\cdot\sqrt{1+\left(\frac{z}{z_R}\right)^2} \tag{4.28}$$

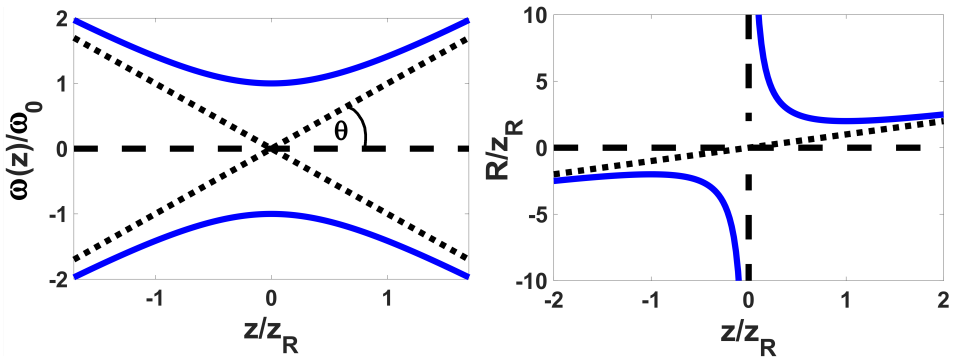

Figure 4.7: Left: Radial beam width $\omega(z)$ of a Gaussian laser beam as a function of z. $\omega(z)$ is normalized to the beam waist and z is normalized to the Rayleigh range, z_R. With increasing distance from the beam waist, $\omega(z)$ increases according to equation 4.27. For very large distances, $\omega(z)$ depends linearly on z (dotted black lines). Additionally, the angle of divergence (θ) is shown. Right: Radius of curvature of the wavefront of a Gaussian beam as a function of the distance from the beam waist. Here, both parameters are normalized to the Rayleigh range. At the beam waist, R diverges as is normally observed for plane waves. With increasing distance, R decreases and reaches a minimum at z_R, meaning that at the Rayleigh range the curvature of the wavefront is maximal. For distances much larger than z_R, the radius of curvature of the wavefront shows a linear dependency on z (dotted black lines).

with the so-called Rayleigh range $z_R=\pi\omega_0^2 n/\lambda_{exc}$. The dependency given in equation 4.28 is also depicted on the left side in figure 4.7. For z=0, $\omega(z=0)$ equals the beam waist ω_0 of the focused laser beam. At the Rayleigh range z_R, the beam width has increased by a factor 1.41 as compared to the beam waist and the amplitude of the intensity distribution equals half of the maximal peak intensity I_0. For large distances from the focus point, $\omega(z)$ depends linearly on z, which is indicated by the dotted lines in figure 4.7 (left). Additionally, in this distance regime an angle of divergence (θ) can be defined [99]:

$$\tan(\theta) = \frac{\lambda_{exc}}{\pi\omega_0 n} \tag{4.29}$$

Consequently, assuming a fixed wavelength, a smaller beam waist leads to a more divergent beam. Another parameter frequently used to characterize a Gaussian beam is the radius of curvature of its wavefront, which is given by [99]:

$$R = z \cdot \left(1 + \left(\frac{z_R}{z}\right)^2\right) \tag{4.30}$$

On the right side of figure 4.7, the dependency of R on the distance z from the focus is depicted. At the beam waist, the radius of curvature of the wavefront goes to infinity, meaning that the wavefront equals the one of a planar wave. With increasing distance from the beam waist, the radius of curvature decreases until the Rayleigh range is reached. For distances much larger than z_R, the wavefront radius of curvature depends linearly on z, as is expected for a spherical wave [100]. In a final step, it can be said that a Gaussian laser beam is completely determined by the laser wavelength and the beam waist.

Having discussed a few of the features of a Gaussian beam, the focus should be set back on its connection to confocal (single-molecule) microscopy.

Considering a Gaussian laser beam focused by a high NA objective into a highly diluted sample droplet containing fluorescent molecules, the probability that a molecule gets excited at a specific position in the droplet is determined by the normalized excitation intensity of the beam at that position. Consequently, a molecule that resides close to the focal region is more likely excited than a molecule only touching the exterior of the Excitation Intensity Distribution (EID). Obviously, the proportionality between excitation intensity and excitation probability is only valid provided that the considered fluorescent molecule is available for excitation or, put another way, not optically saturated [99]. As a next step, the position dependent

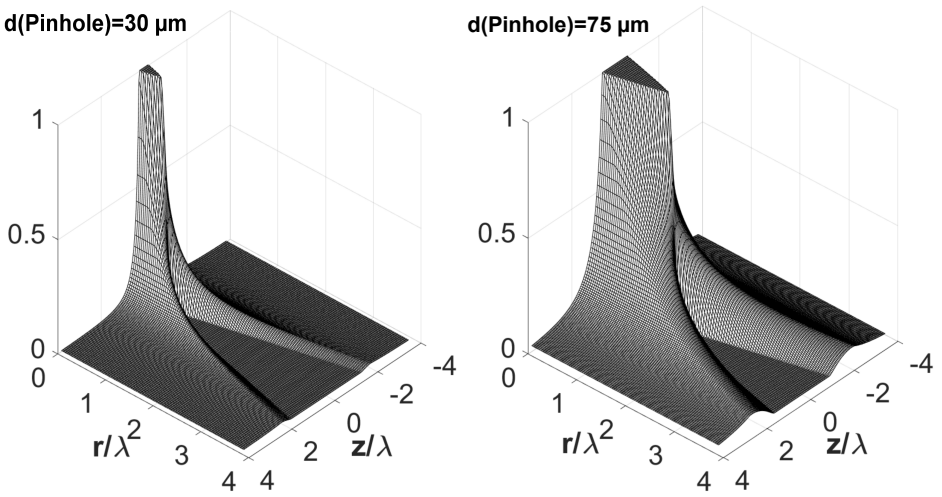

Figure 4.8: Collection efficiency function (CEF) for two different pinhole diameters (NA=1.2, emission wavelength around 500 nm), calculated using a semi-geometric approach [99, 101]. A smaller pinhole size limits the radial and axial extension of the CEF significantly. Both spatial variables are normalized to the emission wavelength.

probability that the photons emitted by an excited molecule are subsequently collected shall be discussed. Assuming that no confocal pinhole is employed in the light path, this probability would be equal for all considered locations. As distinct from that, employing a pinhole leads to a suppression of out of focus light, which naturally means that the probability to collect photons emitted by a molecule residing close to the focal point is much higher than the probability to collect photons from a molecule located more exterior. The quantification of this probability distribution, further on called Collection Efficiency Function (CEF) is discussed in detail in references [99, 101]. Without going into detail, it should be mentioned that the CEF is mainly determined by the NA of the objective and the size of the pinhole. The impact of a varying pinhole diameter on the CEF is shown in figure 4.8.

The complete distribution describing the probability that a molecule at a specific position gets excited and that its fluorescence emission gets collected is obviously given by the product of the EID and the CEF. As already mentioned, this product is called the molecule detection function (MDF). Experimentally, it can either be evaluated with the help of FCS or by directly measuring the point spread function using fluorescent beads [102].

An important quantity: the signal-to-noise ratio (SNR)

Inherent in the measurement of the rather weak fluorescence emission generated by a single molecule lies the need to be able to detect the latter. Nowadays, two typically employed types of point detectors that are sensitive enough to count single-photons are photomultiplier-tubes (PMT) and single-photon-counting avalanche-diodes (SPAD) [103]. In this work, SPADs with wavelength dependent quantum efficiencies between 30 % and 80 % are used for photon detection. The quantum efficiency describes the fraction of incident photons that contributes to the generation of charge carriers. Another important parameter used to characterize SPADs is the dark count rate, which is the average count rate showing up without any incident light. Here, it lies below 100 counts per second.

However, using highly sensitive detection systems one obviously has to consider possible sources of background contributions distorting the signal of interest and limiting the achievable signal-to-noise ratio. Most background photons are generated by the interaction between the excitation light and the solvent molecules surrounding the fluorescent specimen. Disregarding fluorescence impurities, undoubtedly the most disruptive kind of background, elastic (Rayleigh) and inelastic (Raman) scattering of the excitation photons contribute to the measured overall signal. Obviously, the wavelength of elastically scattered photons coincides with the excitation source wavelength. As the fluorescence emission of the specimen is shifted towards lower energies (Stokes Shift), spectral filtering is an efficient way of eliminating the contribution of Rayleigh scattering from the signal. On the contrary, the spectrum of in-elastically scattered light can partially overlap with the fluorescence emission of the specimen, precluding the option of spectral filtering [99]. Therefore, in the first work demonstrating the detection of single fluorescent molecules in liquid at room temperature, fluorescent and background photons were separated using temporal information to enhance the signal-to-background ratio. Using a short excitation laser pulse, scattered photons show a much shorter temporal distance to the preceding pulse than fluorescence photons, so that time-gating facilitates an efficient discrimination between both [7]. However, as the scattering intensity is proportional to the number of scattering solvent molecules, this way of background suppression is mainly important if the MDF volume is rather large. With an MDF-volume commonly lying in the femto-liter range, confocal microscopy setups are intrinsically well-suited to keep the number of scatterers small enough to achieve an adequate signal-to-background ratio (SBR) in single-molecule measurements without the need of time-gating. Additionally, the size of the MDF can be varied by employing pinholes of different sizes and hence can be adjusted to achieve the required SBR. Furthermore, the background rate as well as the number of detected fluorescence photons per molecule and time unit, also known as molecular brightness (MB), are functions of the impinging photon flux (details in section 5.4.1). Consequently, also the SBR is affected by the applied laser power and the experimentalist has to find the optimal excitation power regime for the given experiment. With the help of FCS, the MB of a sample can easily be determined (see section 5.4.2 for details). The corresponding background contribution ($\overline{\mathrm{BG}}$) is obtained by measuring the average count rate generated

by the pure solvent under the same experimental conditions:

$$SBR = \frac{MB}{\overline{BG}} \tag{4.31}$$

Obviously, the dark count rate of the detector is then included in $\overline{\mathrm{BG}}$.

The determined SBR can then be used to estimate the corresponding signal-to-noise ratio (SNR). In general, the SNR is defined as the ratio of the mean of the signal to its standard deviation. Consequently, here it is defined as [104]:

$$SNR = \frac{MB\Delta t}{\sqrt{(MB + \overline{BG})\Delta t}} \tag{4.32}$$

Here, Δt is the measurement duration. Due to the discretization of electromagnetic radiation energy in terms of photons, which are emitted randomly and independent from each other, the number of photons emitted (or detected) in a specific time-interval is statistically described by a Poisson distribution. The corresponding fluctuations in the number of detected photons are called shot-noise. One characteristic of the Poisson distribution is that its mean equals its variance, so the standard deviation of the measured distribution of photon counts is given by the square root in the denominator of equation 4.32. Alternatively, equation 4.32 can be expressed as:

$$SNR = \sqrt{\frac{MB\Delta t}{1 + SBR^{-1}}} \tag{4.33}$$

Therefore, the SNR can either be maximized by increasing the MB of a sample, by enhancing the measurement duration, or by increasing the signal-to-background ratio.

Selection of fluorescence bursts

Having considered the most important points to achieve reasonable measurement conditions, the next step is to discuss the analysis of the obtained raw data. Commonly, the photon detection systems are connected to Time-Correlated-Single-Photon-Counting (TCSPC) electronics further processing the received signal. In classical TCSPC experiments, only the arrival time of each photon with respect to the time of excitation by the laser pulse is used to build up TCSPC histograms. These can be analyzed to obtain information about the fluorescence lifetime distribution of the sample of interest, as already discussed in section 4.1.1. As distinct from that, more advanced photon-counting systems additionally store the arrival time of each photon with regard to the beginning of the measurement. The combined tagging of each photon with its microscopic and macroscopic arrival time is called Time-Tagged-Time-Resolved (TTTR) mode and facilitates more comprehensive ways of data evaluation, for instance TCSPC and FCS in a single experiment. Besides the already mentioned temporal information, each photon can also be assigned to the detection channel it is detected by, providing information about its spectral properties or its polarization. This multi-parameter fluorescence detection-approach can be used to selectively analyze sub-populations in a heterogeneous sample or evaluate molecular dynamics at the single-molecule level [105].

However, coming back to single-molecule measurements, the macroscopic time assigned to each photon is used to discriminate fluorescence photons from background photons. This can be achieved in several ways. Probably the simplest approach is to bin the stream of macroscopic photon arrival times in intervals of equal duration adjusted to the time the molecule needs to traverse the MDF-volume. Assuming a volume in the femto-liter range and biological macro-molecules with hydrodynamic radii of 1-10 nm, the bin sizes typically lie in the ms regime. In a time trace generated in this way, the fluorescence photons of a single molecule show up as a prominent fluorescence burst above a lower background signal [106]. Therefore, each part of the time trace lying above a specific threshold and consisting of multiple photons is selected as a single fluorescence burst. Another approach makes use of the fact that the temporal delay between consecutive fluorescence photons is much shorter than the temporal delay between consecutive background photons [107]. Calculating the delay between every detected photon and the previous (or successive) one, an inter-photon-distance (IPD) trace can be plotted, in which the bursts of fluorescence are presented as dips interrupting the background signal [108]. Again, a specific threshold is defined to select the fluorescence bursts, but as distinct from the previous case the signal IPD lies below the background IPD. In this work, a third approach is used which might be perceived as a hybrid of the previously introduced burst selection schemes. Instead of integrating the photon stream into static bins, around each macroscopic photon arrival time a time-window of specific length (T) is set and the number of photons in this time-window is calculated [109]. This process might be considered as a kind of dynamic binning to generate a local count rate (k_l) and is depicted in figure 4.9. Here,

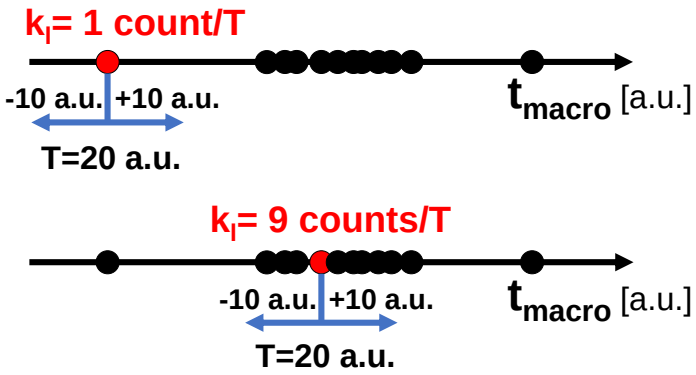

Figure 4.9: Processing of the stream of macroscopic photon arrival times (t_{macro}) leading to the generation of a local count rate (k_l). Around each photon arrival time, a window of length T is arranged and the number of photons in this time-window is calculated. Consecutive fluorescence photons appear with a shorter temporal delay after each other, therefore the number of fluorescence photons in the time-window is much higher than the number of background photons.

the size of the time window has to be adjusted to the range of the molecule's dwell-time in the MDF-volume. The diffusion time determined by FCS can be used as a reference value in this respect [10]. A typically obtained local count rate time trace is depicted in figure 4.10. By way of comparison, the time trace obtained by simple static binning is also shown. Obviously, the photon specific local count rate time trace has a higher resolution than the

statically binned time trace and therefore enables a more precise selection of fluorescence bursts. Additionally, the information contained in the stream of macro-times does not have to be integrated in the case of dynamic binning, which means that all further steps of data processing are naturally possible on the single-photon level. As is shown in figure 4.10, a background spe-

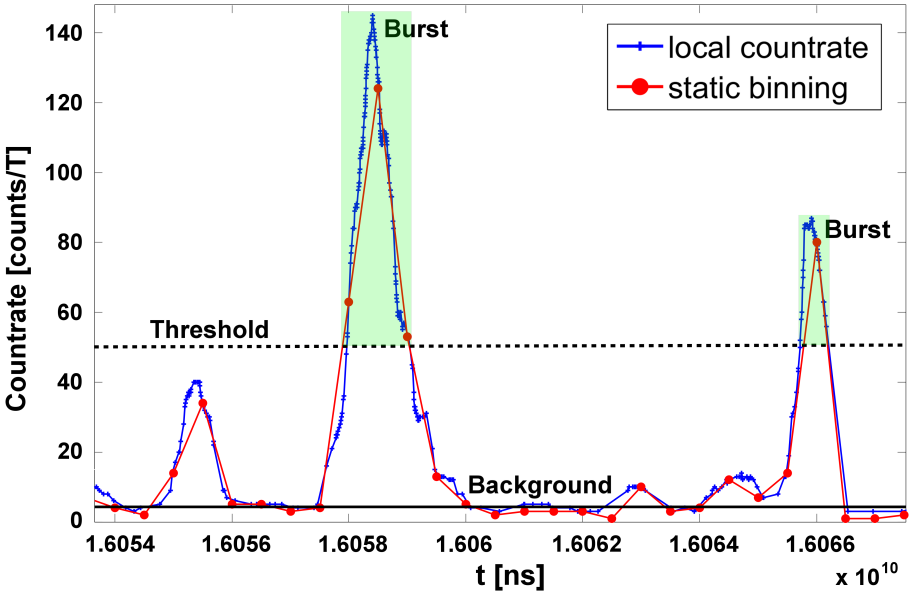

Figure 4.10: Comparison of time trace generated by static binning with time trace showing a local count rate generated by dynamic binning. The local count rate time trace is photon-specific and enables a more precise burst selection. In both approaches, a background count rate specific burst selection threshold has to be defined (dashed black line). The green-shaded areas indicate all photons belonging to a burst.

cific selection threshold (dashed black line) has to be defined, determining the lower limit of the count rate above which photons are considered to belong to a fluorescence burst. This threshold is calculated by taking into account that the number of background photons per time bin, BG, is Poisson distributed around its mean value [99]:

$$p(BG) = \frac{\overline{BG}^{BG}}{BG!} \exp(-\overline{BG}) \tag{4.34}$$

This is also shown in figure 4.11, where the experimental count rate distributions of pure buffer for different time-window lengths are overlayed with the corresponding Poisson distributions. Here, the 481 nm laser in pulsed mode (20 MHz) is employed, applying an excitation power of 1500 a.u.. Given a specific count rate threshold $\mathrm{Thr_{sel}}$, the probability that the count rate generated by background photos reaches or exceeds $\mathrm{Thr_{sel}}$ can be calculated according to:

$$p(BG > Thr_{sel}) = \sum_{BG=Thr_{sel}}^{\infty} p(BG) \tag{4.35}$$

Obviously, equation 4.35 also defines the probability that applying a specific $\mathrm{Thr_{sel}}$, a background photon can be mistakenly selected as a fluorescence

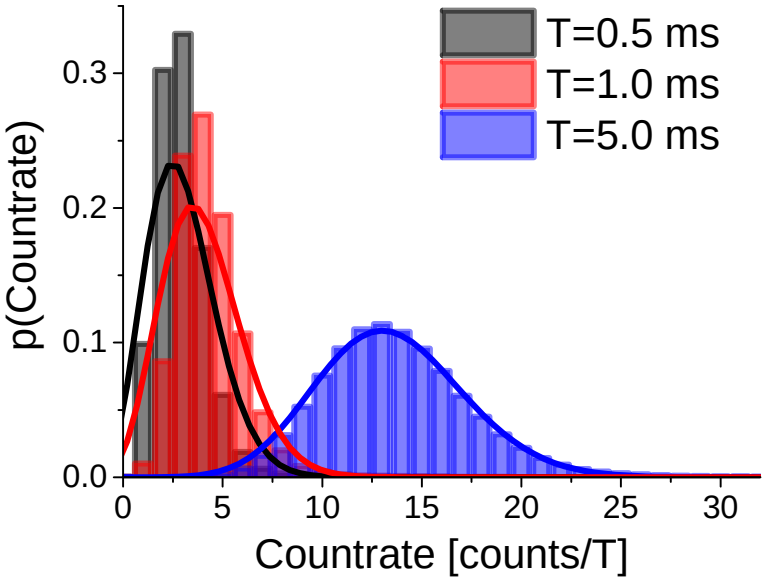

Figure 4.11: Experimental count rate distribution of pure buffer (481 nm laser, 20 MHz, 1500 a.u.). With increasing binning duration, the mean value of the Poisson distribution increases.

photon. In this work, Thr_{sel} is set to a value that corresponds to a probability of around one permille that a false selection occurs.

Having selected all potential fluorescence bursts from a given count rate time trace, commonly only bursts containing more than a specific number of photons are selected to facilitate further evaluation steps [110]. Here, as a first step, the product of the molecular brightness and the diffusion time determined by FCS is used as a coarse estimate of the expected mean number of photons per burst. Although the molecular brightness follows a Super-Poisson distribution in reality [111], here, for convenience and without making a significant error it is assumed to be Poisson-distributed. Hence, also the number of photons per burst, again calculated as the product of the molecular brightness and the diffusion time, is supposed to follow a Poisson-distribution. Considering the latter, the majority of the distribution lies in an interval defined by its mean $\pm$ three standard deviations. As the square root of the mean equals the standard deviation in the case of a Poisson distribution, the minimal reasonable number of photons per burst can be assessed as the mean number of photons per burst minus three times the square root of the mean. To illustrate the impact of this burst selection criterion, two exemplary FRET burst duration distributions of a double-labeled DNA oligo-nucleotide (48 bp, donor (Al488) and acceptor (AL647) linker attachment distance 10 bp) are shown in figure 4.12 (a). The distribution shaded in gray contains all bursts, whereas the distribution shaded in red consists of bursts with sizes above the previously specified threshold only. Obviously, the unrestricted distribution is shifted to smaller burst durations and shows an additional, unsolicited peak around zero. Furthermore, the mean dwell-time the molecule spends in the MDF-volume, here determined by fitting a mono-exponential decay to the burst duration distribution [110], is larger for the distribution of selected bursts only. It should be noted that the mean dwell-time does not coincide with the mean burst duration but is significantly shorter. Additionally, it critically depends

on the applied time-window sizes used to generate the count rate time trace. This is also depicted in figure 4.12 (b) for time-window sizes of 0.5 ms and 2 ms. In figure 4.12 (c), the impact of the time-window length on the acquired mean burst size is visualized, showing that larger time-window sizes lead to an increase of the average number of photons per burst. At last, the dependency of the obtained mean molecular brightness on the time-window length is depicted in figure 4.12 (d), demonstrating that the MB of a sample decreases with increasing T. A more elaborate burst size distribution

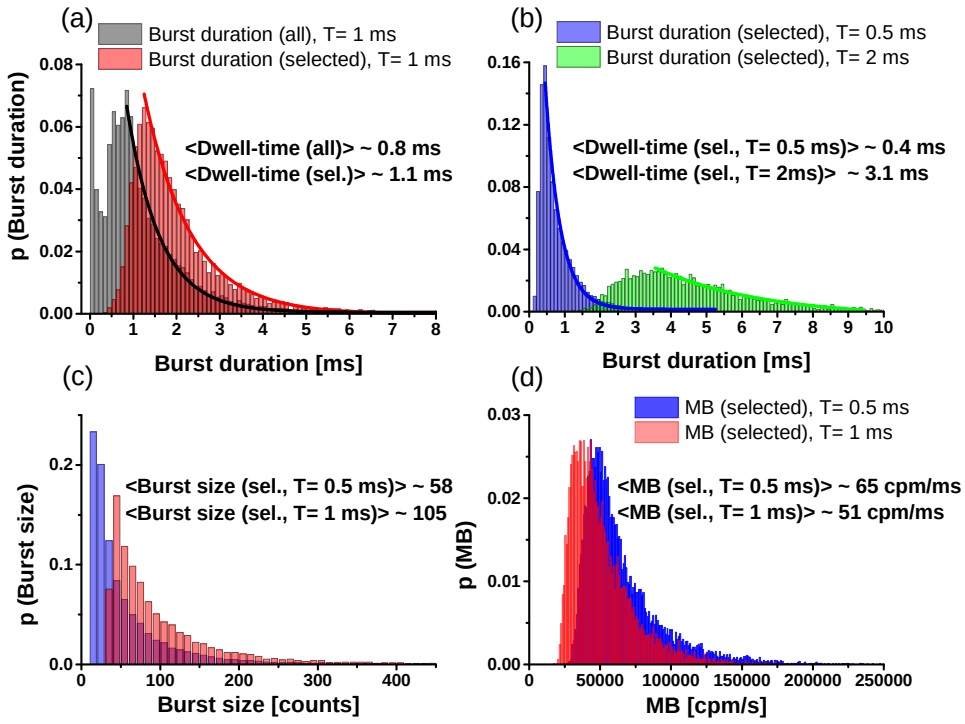

Figure 4.12: Distributions of FRET burst durations, burst sizes and corresponding molecular brightnesses obtained for a double-labeled DNA oligo-nucleotide construct with donor (AL488) and acceptor (AL647) linker attachment points separated by a distance of 10 bp.(a) Impact of eliminating bursts with small numbers of photons on burst duration distribution. The peak around zero showing up in the unrestricted distribution (gray) has vanished in the distribution containing selected bursts only (red). The MDF dwell-time is determined by fitting a mono-exponential decay to the burst duration distribution. The unrestricted distribution shifts the dwell-time to shorter values. (b) Burst duration distributions for T= 0.5 ms and 2 ms. With increasing T, the burst duration distribution gets shifted to larger duration times. (c) Burst size distributions obtained for T= 0.5 ms and T= 1 ms. Doubling the time-window size leads to a twice as large mean burst size. (d) Corresponding molecular brightness distributions. Larger time-windows lead to smaller *MB*-values, as shorter bursts are more likely condensed into larger ones.

analysis is not the focus of this work, nevertheless the given results should raise awareness for the influence of the chosen burst selection parameters on the obtained outcome. However, with respect to FRET it should also be mentioned that FRET efficiency histograms are not that sensitive concerning the burst selection procedure. That means that a time-window size lying in the range of the FCS dwell-time will give reasonable results in most cases. A well-known exception from this rule of thumb are FRET samples with

conformational dynamics with relaxation times on the order of the time-window size, where the chosen value of T can reveal or hide sub-populations [112].

4.2.3 Single-molecule FRET

In the previous sections, an outline of the fundamental physics of FRET was given and the most important aspects of confocal single-molecule spectroscopy were covered. Taking the next logical step, the two worlds will be united in this subsection.

Obviously, the first step towards single-molecule FRET measurements is the selection of the appropriate FRET pair suitable to monitor the process of interest, be it protein unfolding, conformational dynamics or ligand binding, for instance. As already mentioned in the previous sections, this means that (a) the distance between donor and acceptor has to lie in a regime around the Förster radius and (b) the fluorophores have to be bright enough to achieve a SNR value sufficient for the selection of bursts (of an adequate size). In this work, in all cases AL488 is employed as donor and AL647 as acceptor molecule, which results in a Förster radius of ≈ 5 nm, so that the accessible distance regime lies between 3 and 7 nm (see figure 4.4 (b)). Neglecting the properties of the setup, the brightness of a dye is to a great extent determined by its quantum yield and its molar absorption coefficient, therefore AL488 (ϕ_{fl}=0.92, ϵ_{max}=73000 $M^{-1}cm^{-1}$) and AL647 (ϕ_{fl}=0.33, ϵ_{max}=270000 $M^{-1}cm^{-1}$) both are well-suited for single-molecule applications.

Labeling

Commonly, small organic dyes are attached to biological macro-molecules by covalent binding of the reactive group of the fluorophore to a specific side-chain/nucleobase, for instance the -SH group of a cysteine residue in the case of proteins. In figure 4.13, such a reaction scheme of a fluorophore linked to a reactive maleimide group and the thiol group of a bio-molecule is depicted. As cysteine is a relatively rare amino acid [113], it is often

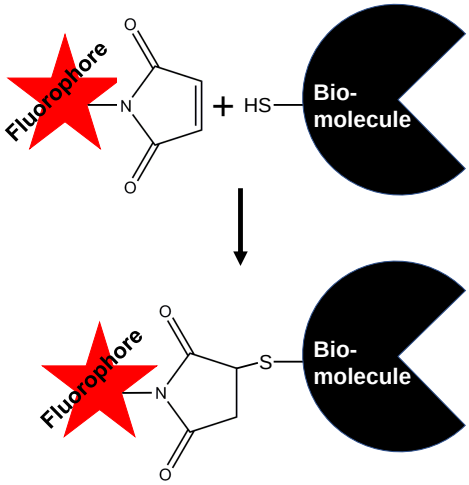

Figure 4.13: A fluorophore linked to a reactive maleimide group binds covalently to the thiol group of the cysteine residue of a macro-molecule.

possible to eliminate cysteine residues by site-directed mutagenesis [114]

without significantly perturbing the protein structure. Then, one or two cysteine residues can be inserted at the specific positions suitable for FRET. The integrity of the mutated structure can be assessed by comparison to the wild-type with regard to, among others, enzymatic activity and content of secondary structure. The latter is often determined by circular dichroism (CD) spectroscopy [115].

In this work, the site-specific double-labeling of the protein Phosphoglycerate Kinase (PGK) is achieved exactly in the mentioned way, namely by maleimide-labeling of two cysteine residues inserted by site-directed mutagenesis. More details on the production of the sample, the labeling procedure and evaluation of mutant integrity/functionality can be found in reference [86].

Acquisition of FRET efficiencies

Sticking to the protocol for single-molecule measurements given in the previous section 4.2.2, the obtained double-labeled sample is highly diluted and the optimal excitation conditions for the sample are determined. The direct fluorescence emission of the donor and the FRET induced fluorescence emission of the acceptor are separated by a spectral filter and detected by two different SPADs. The already mentioned transfer efficiency E can then be determined according to [34]:

$$E = \frac{1}{1 + (\frac{R_{DA}}{R_0})^6} \tag{4.36a}$$

$$= \frac{F_A}{F_A + \gamma F_D} \tag{4.36b}$$

The parameter γ is a calibration factor which takes into account the imperfections of the optical setup and the photo-physical differences between donor and acceptor. It is defined as the product of the ratio of the acceptor transmission/detection efficiency (g_A) to the donor transmission/detection efficiency (g_D), and the ratio of acceptor to donor quantum yield [34]:

$$\gamma = \frac{g_A}{g_D} \frac{\phi_{fl,A}}{\phi_{fl,D}} \tag{4.37}$$

Details on the determination of γ are given in the results section 5.4.2. F_D and F_A denote the corrected number of donor and acceptor photons per selected fluorescence burst, given by:

$$\begin{aligned} F_D &= \tilde{F}_D - \tilde{BG}_D \\ F_A &= \tilde{F}_A - \tilde{BG}_A - \alpha \tilde{F}_D \end{aligned} \tag{4.38}$$

Hence, the experimentally determined numbers of photons are given by $\tilde{F}_{D,A}$ and the corresponding background contributions by $\tilde{BG}_{D,A}$. The latter is determined by multiplying the average background count rate with the burst-duration. The parameter α denotes the fraction of the donor signal unintentionally detected in the acceptor channel, or cross-talk. Experimentally, it can be determined by taking the ratio of the intensity detected by the acceptor-channel to the intensity detected by the donor-channel using a sample containing donor molecules only. In this work, α lies below 1 % for all samples.

Coming back to the burst selection process, the separate streams of donor and acceptor photons are merged into one FRET-photon stream, which is then used to generate a local count rate time trace. Applying the burst selection criteria introduced in section 4.2.2, FRET-bursts are picked and subsequently split into photons belonging to donor and acceptor again. Knowing the exact number of donor and acceptor photons in a burst, the corresponding FRET efficiency can be calculated according to equation 4.36. The obtained distribution of FRET efficiencies can then be used to build up a histogram which can be fitted by one or several Gaussian distribution(s). Thereby, each molecular sub-population in the sample can be associated with a mean transfer efficiency and the corresponding standard deviation [18].

Pulsed interleaved excitation (PIE) and burst coincidence

However, with a labeled FRET-sample at hand, it is worth to remember that all external labeling procedures are imperfect. This means that a double-labeled sample will also contain unlabeled specimen and specimen carrying one or two donors (donor-only sample) or one or two acceptors (acceptor-only sample). While unlabeled and acceptor-only specimen are negligible as they are invisible for the laser light used for donor-excitation, the donor-only sample indeed gets excited but does not transfer any energy due to the lack of an acceptor molecule. Consequently, the obtained FRET efficiency histogram will consist of the distribution of the real FRET-efficiencies and a peak around zero associated with the donor-only population. Obviously, the existence of an acceptor can be checked by directly exciting it and observing the corresponding fluorescence burst. However, to prevent an overlap of direct and FRET-induced acceptor bursts, the direct acceptor excitation has to be applied at some other point in time than the excitation of the donor leading to FRET. This is exactly the working principle of pulsed interleaved excitation (PIE), where the sample gets alternatingly excited by a donor and an acceptor excitation laser pulse [116]. Commonly, the cycle duration is adjusted to be around twice as long as the fluorescence lifetime decay time-window of the donor. A typical TCSPC histogram of a FRET sample excited in PIE-mode is shown in figure 4.14. Obviously, all photons tagged with a microscopic arrival time lying in the FRET window can be used to generate a FRET time trace, whereas the other photons, stemming from the directly excited acceptor, form the further on called PIE time trace. Then, applying the criteria already discussed, all FRET and PIE bursts are selected and their macroscopic starting and ending times are determined. The starting and ending times of each burst, denoted as T_S and T_E further on, are then used to examine whether a FRET burst is accompanied by a coinciding PIE burst or not. The four different temporal configurations leading to coincidence are sketched in figure 4.15. Knowing the numbers of detected FRET, PIE and coincident bursts, further denoted as NB_{FRET}, NB_{PIE} and NB_{DA}, the fraction of double-labeled molecules in the sample can be (roughly) estimated according to:

$$frac_{DA} = \frac{NB_{DA}}{NB_{FRET} + NB_{PIE} - NB_{DA}} \tag{4.39}$$

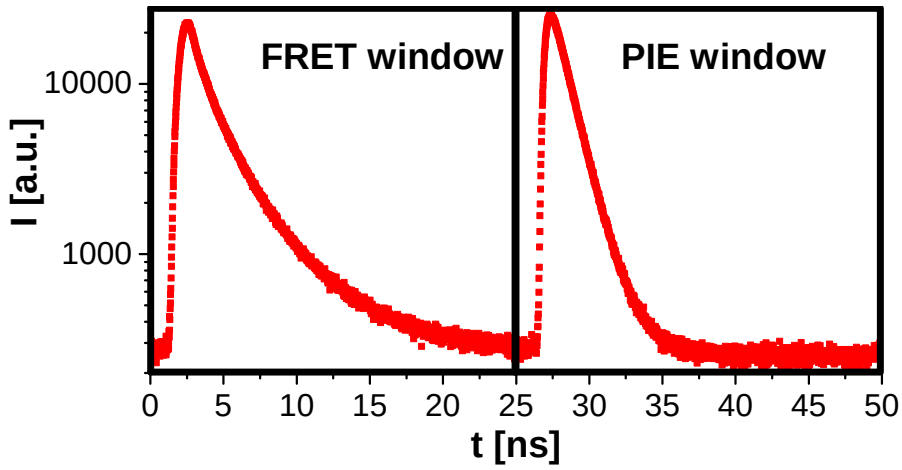

Figure 4.14: Pulsed interleaved excitation: the direct excitation of the donor and the acceptor occur with alternating laser pulses (cycle duration 50 ns , temporal shift between pulses 25 ns). Consequently, donor and acceptor FRET-photons and directly excited acceptor photons can be separated by their microscopic arrival times.

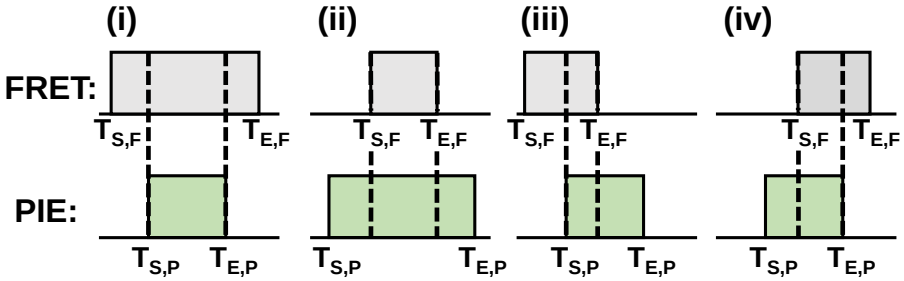

Figure 4.15: Possible temporal configurations of coincident FRET and PIE bursts, sketched as rectangular boxes ranging from the starting to the ending point of each burst. The temporal overlap of both bursts is indicated by the vertical dashed black lines.

As indicated in figure 4.15, two coincident FRET and PIE bursts don't have to temporally overlap exactly. On the one hand, it is possible that the MDF-volumes for the two different wavelengths of donor and acceptor don't match to 100 %, which means for instance that the FRET donor might be excited slightly earlier or later than the acceptor. On the other hand, both fluorophores are prone to bleaching while traversing the MDF-volume, but certainly to a varying extent. This means that a donor might stay intact during the dwell time in the volume whereas the acceptor bleaches, or vice versa. Additionally, donor and/or acceptor can turn into non-fluorescent dark states, for instance by inter-system crossing or by cis-trans isomerization [43]. To eliminate potential photo-physical and/or bleaching artifacts leading to biased transfer efficiencies, the selected coincident bursts are therefore subject to a second analysis step. For each pair of coincident bursts, the overlap time interval is determined, which is depicted by dashed black lines in figure 4.15. Then, only photons with macroscopic arrival times found in this overlap time-interval are used to calculate FRET efficiencies, which simultaneously erases the contribution of blinking and bleaching bursts [109]. The difference between a FRET histogram with and without

the contribution from donor-only and bleaching/blinking bursts is shown in figure 4.16. Besides the prominent donor-only peak, the uncorrected histogram additionally shows a trace of FRET efficiencies ranging from the real distribution to the zero-peak, which is a typical footprint of bleaching and/or blinking of the acceptor. Again, due to the process of counting

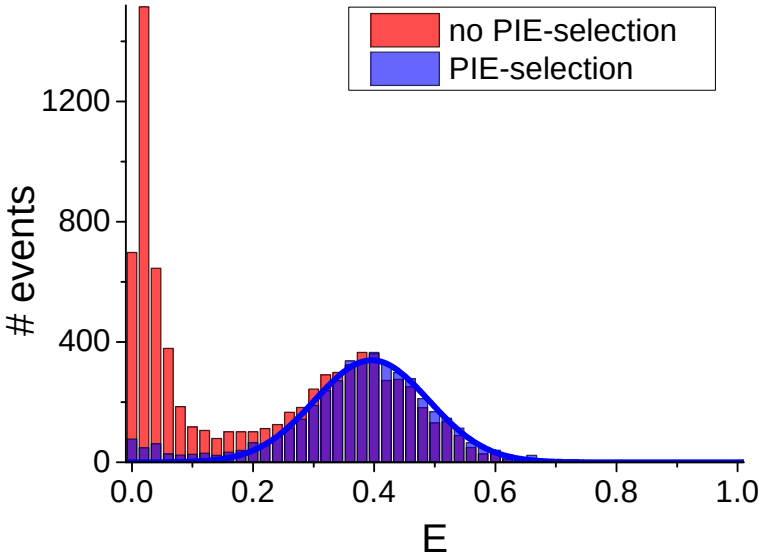

Figure 4.16: FRET efficiency histograms with and without donor-only and bleaching/blinking bursts. In red, the FRET efficiency histogram of all FRET bursts is shown. The FRET efficiency histogram containing FRET-bursts coincident with a PIE burst only is shown in blue.

discrete numbers of donor and acceptor photons in a FRET burst and the related shot-noise, even for a fixed inter-dye distance not a single transfer efficiency, but a distribution around a mean efficiency value ($\bar{E}$) is obtained. Precluding other sources leading to a broadening, the minimal width of the shot-noise limited FRET-distribution is given by [34]:

$$\sigma^2 = \frac{\bar{E}(1-\bar{E})}{(F_D + F_A)_{min}} \tag{4.40}$$

Here, $(F_D{+}F_A)_{min}$ is defined as the minimal number of fluorescence photons per FRET burst included in the transfer efficiency calculation. Comparing the width of the experimentally determined FRET histogram with the shot-noise limited distribution can provide information about additional processes inducing a broadening of the histogram, for instance slow conformational dynamics (timescale $\approx$ dwell-time) or photo-physical artifacts [117, 118].

4.3 Fluorescence Correlation Spectroscopy (FCS)

Fluorescence Correlation Spectroscopy, further on abbreviated as FCS, was originally introduced in the 1970s in the seminal papers by Elson, Magde and Webb [49, 50]. At that time, diffusion coefficients and chemical reaction rate constants were only accessible by experiments in which a system was at first slightly perturbed, and then monitored during its relaxation back to equilibrium. In contrast to that, based on the fundamental regression hypothesis stated by Onsager [119, 120], Elson et al. made use of microscopic

(thermodynamic concentration) fluctuations in an *equilibrated* system to determine its macroscopic transport properties and chemical interaction rates.

To facilitate the observation of these spontaneous microscopic fluctuations, fluorescent markers proved to be useful monitors displaying the latter. On the one hand, many fluorophores react sensitive to changes in their environment, for instance the binding of a ligand or a conformational change, by decreasing or enhancing their emission rate. On the other hand, any laser beam used for their excitation defines a well-defined open volume the labeled specimen can enter or leave, thereby facilitating the observation of diffusion related concentration fluctuations. The time dependence of any kind of fluctuation in the fluorescence signal is then determined by calculating and subsequently analyzing its corresponding correlation curve, explaining the term FCS.

However, due to relatively dim fluorophores, low detection efficiencies, large ensemble numbers and significant background scattering, the correlation curves obtained in the early studies by Elson et al. suffered from low signal-to-noise ratios and the resultant need of measurement times of several hours. Naturally, spontaneous, non-synchronized fluorescence intensity fluctuations only contribute significantly to the overall signal when very few, relatively bright molecules reside in a sufficiently small open volume. Accompanied by steady technical improvements and the synthesis of brighter fluorescent labels, this requirement was met for the first time by Rigler and colleagues around 1990, when they combined the concept of FCS with the experimental advantages of confocal microscopy [121]. These were discussed extensively in the previous sections and will not be recapitulated at this point. Nevertheless, it should be mentioned here that, with the spatial extent of the MDF lying in the femto-liter range, nowadays FCS optimally works with samples in the nano-molar range. Depending on the brightness of the fluorescent labels and the required SNR, measurement durations typically lie in the range of seconds to a few minutes.

4.3.1 FCS theory boiled down

Now, a few of the basic mathematical concepts needed to understand FCS shall be described. In general, the correlation function of the detected fluorescence signal is given by [122]:

$$G(\tau_c) = \frac{\langle \delta I(t) \delta I(t+\tau_c) \rangle}{\langle I(t) \rangle^2} \tag{4.41}$$

Before considering further details, it is worth to have a closer look at the amplitude of the correlation curve, given by:

$$G(0) = \frac{\sigma^2_{I(t)}}{\langle I(t) \rangle^2} \tag{4.42}$$

Here, $\sigma^2_{I(t)}$ denotes the variance of the fluorescence signal. It is intuitively clear that the mean value of the measured fluorescence signal should be proportional to the mean number of fluorescent particles in the considered excitation/photon collection volume, and that its variance should resemble the variance of this number. In section 4.2.2 it has been shown that, low

sample concentrations given, the mean number of particles in a small volume follows a Poisson distribution. Consequently, equation 4.42 can be written as:

$$G(0) = \frac{\sigma_n^2}{\langle n \rangle^2} = \frac{1}{\bar{n}} \tag{4.43}$$

Hence, independent from the measurement setup at hand, the inverse of the correlation curve amplitude equals the mean number of fluorescent particles in the considered volume.

The *MDF* and the effective volume

Now focusing on confocal microscopy and assuming a single fluorescent species, fluctuations in the fluorescence signal can be calculated according to [122]:

$$\begin{aligned} \delta I(t) &= I_0 \int MDF(\vec{r}) \delta(\sigma_{\lambda_e xc} \phi_{fl} \cdot c(\vec{r}, t)) dV \\ &= \int MDF(\vec{r}) \delta(MBc(\vec{r}, t)) dV \end{aligned} \tag{4.44}$$

Here, c(r⃗,t) denotes the local particle concentration and the product of quantum yield (ϕ_{fl}), absorption cross section ($\sigma_{\lambda_{exc}}$) and excitation intensity (I_0) is combined into the molecular brightness (MB). Under the assumption that the molecular brightness stays constant, hence excluding chemical interactions and considering diffusion processes only, equation 4.44 can be simplified to:

$$\delta I(t) = MB \int MDF(\vec{r}) \delta c(\vec{r}, t) dV \tag{4.45}$$

Insertion of equation 4.45 into the enumerator of equation 4.41 then leads to:

$$G_{en}(\tau_c) = MB^2 \iint MDF(\vec{r}_1) MDF(\vec{r}_2) \langle \delta c(\vec{r}_1, t) \delta c(\vec{r}_2, t + \tau_c) \rangle dV_1 dV_2 \tag{4.46}$$

As a next step, the so-called concentration correlation factor has to be introduced [50]:

$$\begin{aligned} \Phi(\vec{r}_1, \vec{r}_2, \tau_c) &= \langle \delta c(\vec{r}_1, t) \delta c(\vec{r}_2, t + \tau_c) \rangle \\ &= \langle \delta c(\vec{r}_1, 0) \delta c(\vec{r}_2, \tau_c) \rangle \\ &= \langle c \rangle (4\pi D \tau_c)^{-3/2} \exp\left(-\frac{(\vec{r}_1 - \vec{r}_2)^2}{4D\tau_c} \right) \end{aligned} \tag{4.47}$$

The step leading from the first line of equation 4.47 to its second line is valid due to the principle of microscopic reversibility and the fact that the system is stationary. The third line is the classical solution to the diffusion equation in an open system and three dimensions. Insertion of the second line of equation 4.47 into the correlation function 4.41 yields:

$$G(\tau_c) = \frac{\iint MDF(\vec{r}_1)(\vec{r}_2) \Phi(\vec{r}_1, \vec{r}_2, \tau_c) dV_1 dV_2}{\langle c \rangle^2 \left(\int MDF(\vec{r}_1) dV_1 \right)^2} \tag{4.48}$$

As previously done for the general correlation function 4.41, now the amplitude of the specified correlation curve given by equation 4.48 should be examined [122]:

$$\begin{aligned} G(0) &= \frac{\iint MDF(\vec{r}_1)MDF(\vec{r}_2)\Phi(\vec{r}_1,\vec{r}_2,0)dV_1dV_2}{\langle c\rangle^2\left(\int MDF(\vec{r}_1)dV_1\right)^2} \\ &= \frac{\iint MDF(\vec{r}_1)MDF(\vec{r}_2)\langle c\rangle\delta(\vec{r}_1-\vec{r}_2)dV_1dV_2}{\langle c\rangle^2\left(\int MDF(\vec{r}_1)dV_1\right)^2} \\ &= \frac{1}{\langle c\rangle}\left[\frac{\int MDF^2(\vec{r}_1)dV_1}{\left(\int MDF(\vec{r}_1)dV_1\right)^2}\right] \\ &\stackrel{!}{=} \frac{1}{\bar{n}} \end{aligned} \tag{4.49}$$

Going from the first to the second line of equation 4.49, the initial condition of the solution of the three-dimensional diffusion equation is used to replace the concentration correlation factor at time zero. In the third line, the integration of the delta distribution is carried out. The fourth line simply reproduces the identity between the inverse of the correlation amplitude and the number of fluorescent particles in the measurement volume. By comparison of the third and the fourth line of equation 4.49, it gets clear that the factor in square brackets has to be the inverse of an effective measurement volume:

$$V_{eff} = \frac{\left(\int MDF(\vec{r})dV\right)^2}{\int MDF^2(\vec{r})dV} \tag{4.50}$$

As was shown in the previous sections, the *MDF* is the normalized product of the EID of the Gaussian laser beam and the CEF taking into account the properties of the objective and the pinhole. However, although a realistic modeling of the MDF would provide an exact (numerical) calculation of the effective volume, an analytical solution of the integral in equation 4.50 is not achievable. For convenience, the exact MDF is therefore approximated by a three-dimensional Gaussian distribution [122]:

$$MDF_{Gauss} = \exp\left(-\frac{r^2}{\omega_0^2}\right)\exp\left(-\frac{z^2}{\omega_z^2}\right) \tag{4.51}$$

Insertion of equation 4.51 into equation 4.50 and subsequent integration leads to:

$$V_{eff} = \pi^{3/2}\omega_0^2\omega_z \tag{4.52}$$

It is worth to mention that V_{eff} is by a factor of $\sqrt{8}$ larger than the confocal volume obtained by the direct integration of the approximated MDF.

Pure diffusion, triplet and calibration equation

Having obtained a rough picture of the theory behind FCS, from this point on only the resulting equations needed in this work will be given. With the MDF approximated by a Gaussian, the correlation function describing the case of pure diffusion of one species is given by [122]:

$$G_{PD}(\tau_c) = \frac{1}{\bar{n}}\frac{1}{1+\frac{\tau_c}{\tau_D}}\frac{1}{\sqrt{1+\frac{\tau_c}{\tau_D\kappa^2}}} \tag{4.53}$$

Here, κ is defined as the ratio of the axial to the radial $1/e^2$ half axes of the effective volume and should not be confused with the orientation factor used in the theory of FRET. The characteristic dwell time of the molecule in the effective volume is denoted as τ_D. Knowing the radial $1/e^2$ half axis, it can be used to determine the setup independent diffusion coefficient D:

$$D = \frac{\omega_0^2}{4\tau_D} \tag{4.54}$$

Besides the intensity fluctuations caused by diffusion, which commonly determine the shape of the correlation curve in the millisecond rang, inter-system crossing to a long-lived excited triplet state leads to the blinking of the fluorescent molecules in the microsecond regime. The correlation function describing the case of diffusion and additionally taking into account transitions to and from triplet states is given by:

$$G_{PD,T}(\tau_c) = G_{PD}\left(1 + \frac{\bar{T}}{1-\bar{T}}\exp\left(-\frac{\tau_c}{\tau_T}\right)\right) \tag{4.55}$$

Having a look at equations 4.53 and 4.55, it is clear that fitting the model equations to the measured correlation curves the parameters $\tau_{D,T}$, T and $\bar{n}$ are adjusted, whereas κ should be known and fixed. Additionally, to calculate the diffusion coefficient D, the radial $1/e^2$ half axis has to be inserted into equation 4.54. Consequently, the extent of the effective volume has to be determined before the sample of interest can be analyzed.

This is easily achieved by analyzing the FCS curve obtained for a sample with a know diffusion coefficient, in most cases a fluorophore freely diffusing in aqueous solution [102]. The pure diffusion equation can then by written as:

$$G_{PD}(\tau_c) = \frac{1}{\bar{n}}\frac{1}{1+\frac{\tau_c 4D}{\omega_0^2}}\frac{1}{\sqrt{1+\frac{\tau_c 4D}{\omega_0^2\kappa^2}}} \tag{4.56}$$

Now, fitting the equation to the measured correlation curve the diffusion coefficient is fixed and the parameters $\bar{n}$, κ and ω_0 are adjusted. Obviously, the same can be done by fitting the triplet model, except that in this case two more free parameters contribute.

Often, the nominal value of the diffusion coefficient known from some literature source is valid at 25° C, which means that, if the calibration measurement is performed at a different temperature, the actual diffusion coefficient has to be corrected according to [123]:

$$D(T) = D_{25}\cdot\frac{T}{298.15K}\cdot\frac{8.9\cdot10^{-4}Pas}{\eta(T)} \tag{4.57}$$

with:

$$\eta(T) = 2.414\cdot10^{-5}Pas\cdot10^{\left(\frac{247.8K}{T-140K}\right)} \tag{4.58}$$

Here, T is the temperature in Kelvin. Equation 4.58 describes the dependency of the dynamic viscosity of water on the temperature.

Detector after-pulsing

Sensitive detectors working in the photon-counting Geiger mode, like the SPADs employed in this work, are prone to a phenomenon called after-pulsing, which means that after a real photon detection event a spurious

detection event is potentially created [124]. Unfortunately, this leads to an additional bump in an FCS curve at short time-scales, hence complicating the analysis of processes occurring in this temporal range. To circumvent this problem, in this work the fluorescence emission signal is split onto two different detectors and the two intensity traces are cross-correlated. As the after-pulsing events created by the two different detectors are uncorrelated, they do not contribute to the correlation curve generated in this way.

All other details about FCS that are important for specific applications are explained in the referring results sections.

4.4 Time-resolved anisotropy (TRA) measurements

In this work, time-resolved anisotropy (TRA) measurements are only employed to make estimations about the orientation factor κ^2 important for FRET. Hence, TRA is not one of the core techniques used in this thesis, therefore only a short outline will be given in the following.

Considering an isotropic fluorescent sample solution that is excited with a linearly polarized, short laser pulse, molecules with specific orientations are more likely to pass to an excited state than others, which is also called photo-selection. This leads to the fact that, at least in the moment of excitation (or time zero), the fluorescence emission of the sample is an-isotropic. However, due to Brownian motion the fluorescent molecules continuously rotate and consequently change their orientation, which after some specific time leads to a sample fluorescence emission that is isotropic again. Obviously, the time-scale of this depolarization depends on the rotational correlation time of the considered sample [43].

With the orientation of the polarization vector of the excitation source taken as reference, the extent of the anisotropy of a sample can be quantified by comparing its parallely and perpendicularly polarized fluorescence emission components. With the help of TCSPC this can be done in a time-dependent manner, which allows to determine the rotational correlation time of a fluorescent molecule, regardless of whether it freely diffuses in solution or is attached to a macro-molecule. In the latter case, additional information about the restriction of the rotational freedom of the fluorescent marker and the flexibility of the domain it is bound to can be obtained [43].

The parallely and perpendicularly polarized fluorescence emission components, $I(t)_{\parallel}$ and $I(t)_{\perp}$, are defined as [43]:

$$\begin{aligned} I(t)_{\parallel} &= I_{fl}(t)(1 + 2r_0 Ph(t)) \\ I(t)_{\perp} &= G I_{fl}(t)(1 - r_0 Ph(t)) \end{aligned} \tag{4.59}$$

Here, $I_{fl}(t)$ is the fluorescence lifetime decay already defined in equation 4.4 and G (also known as G-factor) is a calibration factor correcting for potential, polarization dependent differences in the detection efficiency of the setup. The anisotropy decay is given by the product of the fundamental (or time-zero) anisotropy, here denoted as r_0, and the sample specific, time-dependent anisotropy function Ph(t).

In the case of freely diffusing fluorophores, the anisotropy function is given by a mono-exponential function [43]:

$$Ph(t) = \exp\left(-\frac{t}{\theta_r}\right) \tag{4.60}$$

Here, the rotational correlation time of the fluorophore is denoted as θ_r. The anisotropy function describing a fluorophore attached to a macro-molecule is given by the so-called wobbling-in-a-cone-model [125]:

$$Ph(t) = \left[(1 - A_\infty)\exp\left(-\frac{t}{\theta_r}\right) - A_\infty\right]\exp\left(-\frac{t}{\theta_{r,slow}}\right) \tag{4.61}$$

In this case, the fluorophore is again characterized by its rotational correlation time θ_r, but also by the parameter A_∞ quantifying its motional restriction. It is given by [125]:

$$A_\infty = \left[0.5\,(1 + \cos(\theta_{max}))\cos(\theta_{max})\right]^2 \tag{4.62}$$

Here, θ_{max} is the half angle of a cone the transition dipole moment of the fluorescent marker is free to rotate in. The rotational correlation time of the macro-molecule is given by $\theta_{r,slow}$.

However, it is important to mention that equation 4.59 only applies in cases where the sample excitation and photon collection occur under small angles. The reason for that is depicted in figure 4.17, showing the excitation path in a standard, cuvette-based measurement setup in the upper sketch, and the excitation path in a confocal microscope in the lower sketch. Whereas in the case of small convergence angles the polarization vector orientation does not change significantly, a high NA objective converts the previously unique polarization vector orientation of the linearly polarized laser beam into a distribution of orientations. Obviously, the reverse situation occurs considering the fluorescence emission collected by the high NA objective.

In this work, all TRA measurements were performed using the MT200, hence, the mentioned depolarization effects have to be taken into account. Therefore, equations 4.59 are adjusted to [38]:

$$\begin{aligned} I(t)_\parallel &= I_{fl}(t)\left[1 + k_1(\alpha,\beta)\frac{5}{2}r_0 Ph(t)\right] \\ I(t)_\perp &= GI_{fl}(t)\left[1 + k_2(\alpha,\beta)\frac{5}{2}r_0 Ph(t)\right] \end{aligned} \tag{4.63}$$

Here, the parameters k_1 and k_2, which are functions of the convergence angle of the laser beam (α) and the maximum angle of photon collection (β), correct for potential depolarization effects. Reasonable values lie between 0 and 0.8 for k_1 and between -0.4 and 0 for k_2. Obviously, equation 4.59 is a special case of equation 4.63 with k1= 0.8 and k2= -0.4 inserted.

As already mentioned in section 4.1.1, every TCSPC histogram is affected by the profile of the IRF of the detection system and can only be analyzed accurately by iterative re-convolution. In the case of TRA, the TCSPC histograms for the two polarization components are determined simultaneously using two different detectors, hence two different IRFs have to be taken into account. Additionally, a reasonable way to obtain more reliable output parameters is to fit the two different TCSPC histograms globally, with the rotational correlation time, the fluorescence lifetime and intensity, and the fundamental anisotropy being the minimal set of global parameters.

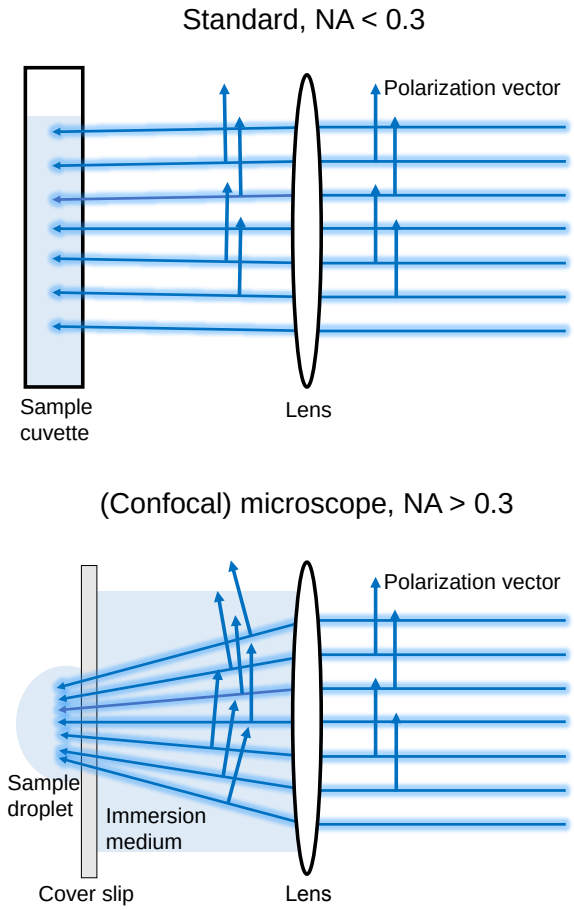

Figure 4.17: Upper figure: Standard, fluorescence spectrometer setup: the linearly polarized laser beam is only slightly focused before impinging on the sample cuvette, so that the orientation of the polarization vector does not change significantly. Lower figure: Confocal microscopy: the linearly polarized laser beam is focused by a high NA objective before impinging on the sample. The unique orientation of the polarization vector is converted into a distribution of orientations (refraction at interfaces not depicted here).

Chapter 5

Results

5.1 Characterization of the confocal microscope MT200

The fundamental prerequisite for all experimental work is the profound knowledge of the tools one wants to use. Therefore, this chapter starts with a thorough characterization of the confocal setup, introducing a number of parameters that will also be of interest for other sections following later on.

5.1.1 Laser beam size characterization

The radial intensity distributions of the laser beams, operated in *cw*-mode here, were measured between M1 and SM1 of the MOU (see Figure 3.2 for details) with the help of the Beamage 3.0 system. The center of the Beamage 3.0 CMOS detection sensor was fixed approximately 5 cm behind M1 on the beam propagation axis ($\hat{=}$ z- axis), with the active sensor area approximately perpendicular to the latter. The size of the sensor area is 11.3 x 6.0 mm^2, with a pixel equivalent of 2048 x 1088. Consequently, the resolution is approximately 5.5 x 5.5 μm^2 per pixel. The measured intensity distributions are depicted as two-dimensional contour projections in Figure 5.1, with the corresponding contour profiles (intersecting the distribution maximum) added at the top and on the right side. For both laser beams, the $1/e^2$ radii along the x- and y-axis lied around 2 mm and did not show any measurable changes with varying positions of the sensor along the z- axis (data not shown here).

5.1.2 Power diode read-out: Conversion from a.u. to Watts

To enable an online-control of the laser power reaching the back aperture of the objective, a small part of the excitation light passing through the MOU is deflected by the semitransparent mirror SM1 and impinges on a photo-diode (see Figure 3.2 for details). There, the measured power is specified in arbitrary units (a.u.), so one needs to know how to convert the photo-diode read-out into the physically relevant unit Watts. This can be achieved by determining sets of corresponding Watt/a.u. pairings with the help of a power meter. The slope of a linear function fitted to the corresponding data points gives the required conversion factor, here denoted as s. The results obtained for the given setup are depicted in figure 5.2, measured with the power meter placed on top of the objective thread (objective removed). It is important to notice that in the case of the 481/487 nm laser the conversion factor changes significantly going from pulsed to *cw*-excitation, whereas it stays constant for the 633/637 nm laser.

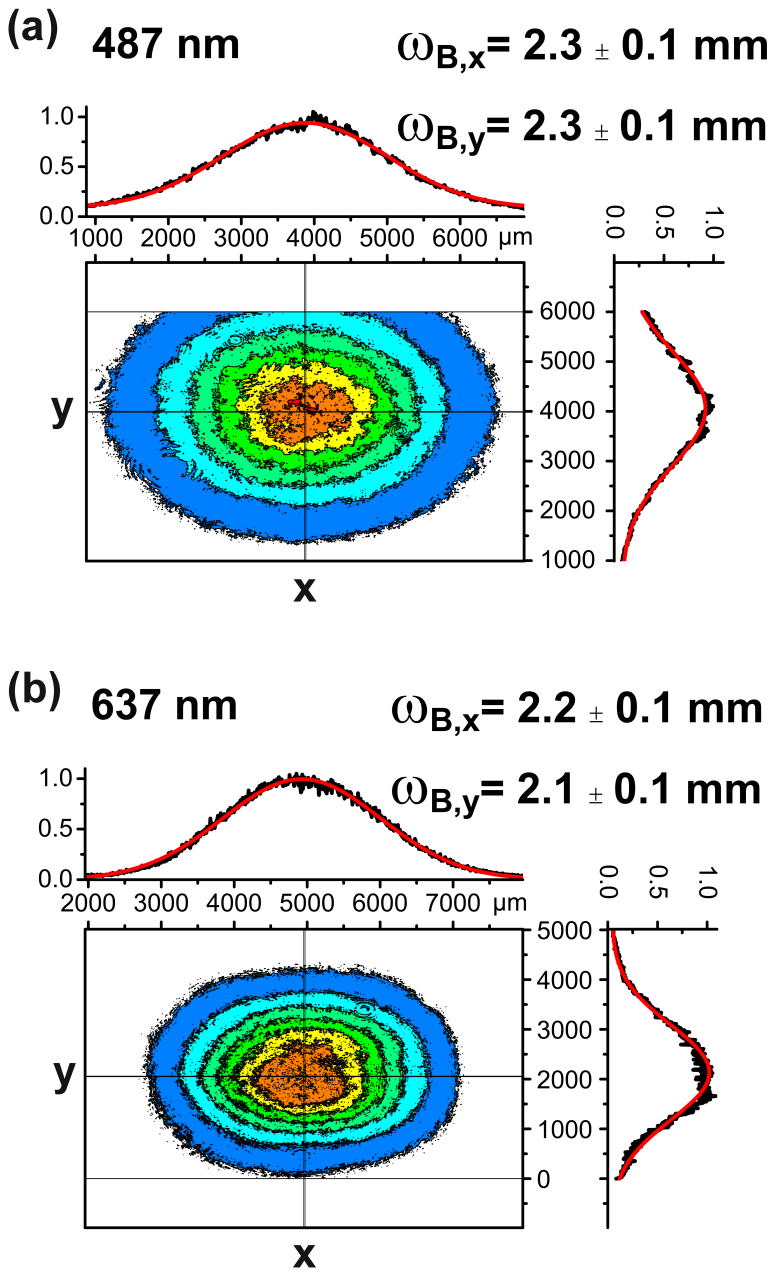

Figure 5.1: Contour projection and x,y-contour profiles of the radial intensity distributions of the excitation laser beams. (a) Center: Radial intensity distribution of the 487 nm laser beam operated in *cw*-mode (center of sensor area not coincident with z- axis). Top: contour profile along x-axis, y-position fixed to maximum of intensity distribution. Right: equivalent contour-profile along y-axis. $\omega_{B,x}$ and $\omega_{B,y}$ denote $1/e^2$-radii of Gaussian distributions (red) fitted to contour profiles (black). (b) Corresponding representation for 637 nm laser. $\omega_{B,x}$ and $\omega_{B,y}$ are slightly smaller than for the 487 nm laser.

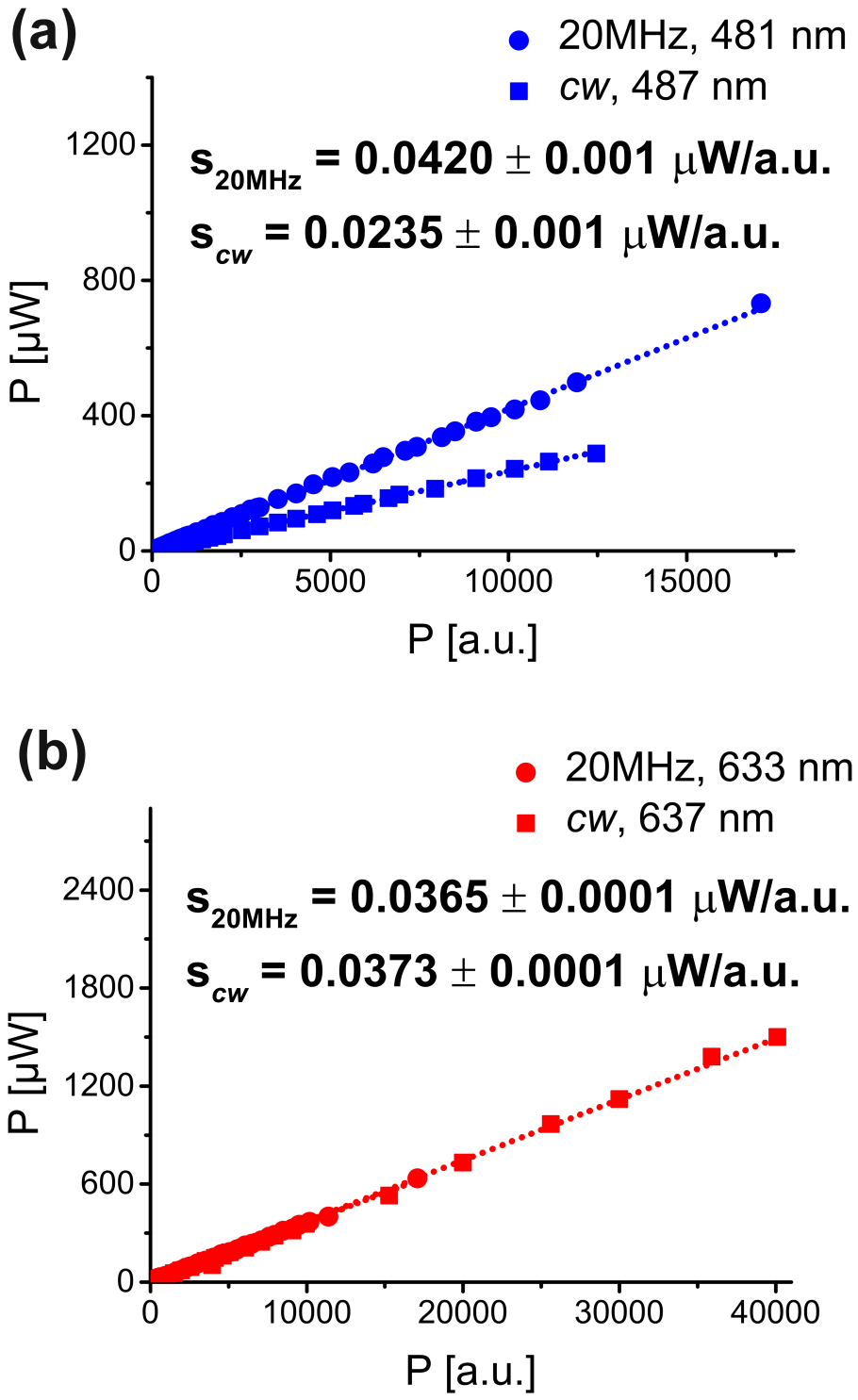

Figure 5.2: Pairings of power meter (µWatt) and photo-diode (a.u.) read-out for both lasers. (a) The conversion factor s changes going from pulsed (481 nm, blue dots) to *cw*-excitation (487 nm, blue squares). (b) The conversion factor stays constant going from pulsed (633 nm, red dots) to *cw*-excitation (637nm, red squares).

5.1.3 Molecule detection function (MDF)

Bead imaging

The MDF can be determined experimentally with the help of fluorescent beads that have a radius smaller than the airy disc of the objective. Here, Tetra-speck^{TM} Microspheres with a radius of 50 nm were used to determine MDF cross-sections of the MT200 equipped with the default objective and the 30 µm confocal pinhole. The excitation power was set to 20 a.u. for both lasers, corresponding to P_{481}= 0.84 µW and P_{633}= 0.73 µW. To be able to determine the focal shift of the two MDFs measured for the two different excitation wavelengths, the lasers were operated in PIE-mode. As compared to imaging the fluorescent beads with two colors at the same time, using PIE has the advantage that problems due to fluorescence bleed through or FRET are minimized. The obtained results are shown in Figures 5.3. First, it should be noticed that the xy-contour projection of the PSF is not symmetric and that its yz-projection appears to be slightly tilted. This phenomenon was already observed earlier in other measurements and is a consequence of laser beam astigmatism induced by the usage of a polarization maintaining fibre [126]. Fitting a Gaussian distribution to each of the contour-profiles, the $1/e^2$-radii and the peak positions of the intensity distributions, here denoted as $\omega_{x,y,z}$ and $[x,y,z]_c$, can be determined. The obtained results are given in figure 5.3. The shift between the focal points of the two MDF-volumes lies around 30 nm along the x-axis and between 40 and 100 nm along the y-axis. Along the z-axis, a shift of $\approx$ 200 nm is observed.

FCS

As shortly discussed in section 4.3.1, another way to determine the $1/e^2$ half axes of the MDF is to analyze the FCS curve of a fluorophore with a well-known diffusion coefficient. Here, AL488 and AL647 in ultra-pure water were used as calibration samples, with $D_{AL488,25}$ = 435 µm^2/s [127] and $D_{AL647,25}$ =330 µm^2/s [123]. The number 25 indicates that these diffusion coefficients are valid at a temperature of 25° C and have to be adjusted to the measurement conditions as described in section 4.3.1. For each fluorophore sample and the 30 µm pinhole, five measurements of two minutes each were performed applying an excitation power of 100 a.u.. For the larger pinhole sizes, the samples were measured twice only. In all cases, the average number of fluorophores in the effective volume was adjusted to lie between 1 and 10. The obtained results are shown in table 5.1.

λ_{exc} [nm]	Pinhole diameter [µm]	ω_0 [nm]	ω_z [nm]
481	30	235 ± 32	1022 ± 200
633	30	239 ± 28	1584 ± 550
481	50	265 ± 25	1386 ± 210
633	50	319 ± 33	1925 ± 371
481	75	311 ± 33	2694 ± 603
633	75	360 ± 28	3623 ± 1240

Table 5.1: Summary of $1/e^2$ half axes of MDF obtained by FCS.

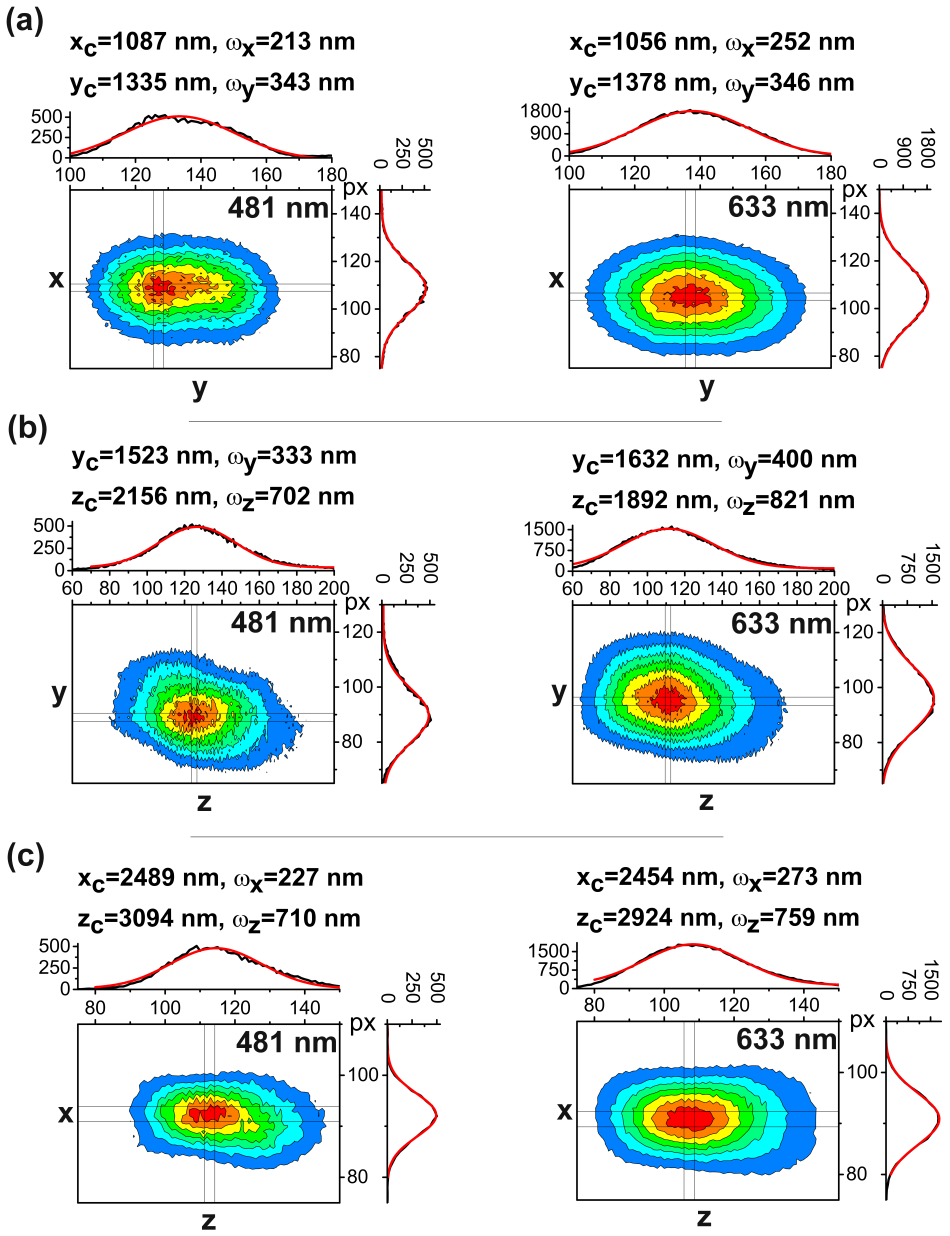

Figure 5.3: (a) xy-, (b) yz- and (c) xz- PSF cross-sections for both excitation wavelengths (left: 481 nm, right: 633 nm, resolution smaller than 20 nm per pixel side in all cases). Peak positions of Gaussian distributions (red line) fitted to contour-profile data points (black line) are denoted as $[x,y,z]_c$, corresponding $1/e^2$-radii as $\omega_{x,y,z}$.

Within the error limits, the radial extent of the MDF determined by FCS coincides with ω_x obtained by bead imaging. Taking into account the rather large error of ω_z obtained by FCS, it is reasonable to say that it at least lies in the same order of magnitude as the axial extent determined with the help of the fluorescent beads. As expected from the purpose of the pinhole to act as a spatial filter along the beam propagation axis, the MDF gets more elongated with increasing pinhole diameter.

MDF volume overlap

The overlap of the MDF volumes for the two different laser excitation wavelengths can be assessed roughly by depicting the MDF volumes as ellipsoids with half axis ω_x and ω_z as determined by FCS. The relative shift of the ellipsoid centers is determined by the parameter $[x,y,z]_c$ obtained by bead imaging. The results are shown in figure 5.4. In the case of the 30 µm pinhole, roughly 20 % of the blue volume don't overlap with the red volume, whereas around 50 % of the red volume don't overlap with the blue volume. Obviously, considering the 75 µm pinhole the complete blue volume lies inside the red volume, but only 50 % of the red volume coincide with the blue one. Concerning FRET-measurements employing the larger pinhole this means that no severe MDF volume mismatch has to be corrected for. However, employing PIE to check for coincident bursts, the amount of single-labeled acceptor molecules is probably over-estimated. Additionally, very few donor-only molecules might be considered double-labeled erroneously. However, this picture does not take into account any photo-physical properties of the fluorophores used and should just serve as an illustration.

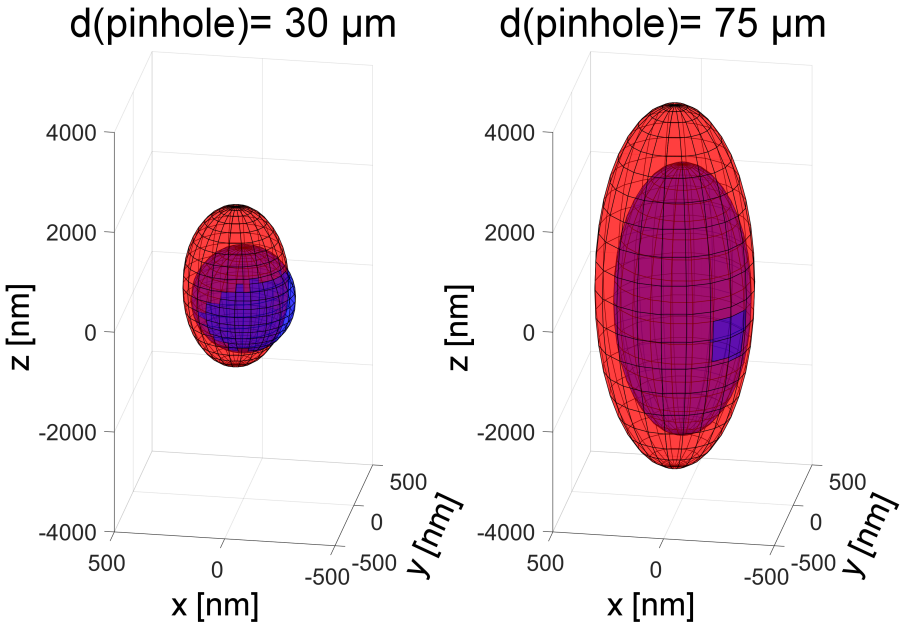

Figure 5.4: Ellipsoidal approximations of MDF volumes for 481 nm (shaded blue) and 633 nm laser (shaded red) for different pinhole sizes.

5.2 Temporal resolution of the MT200: the instrument response function (IRF)

As already mentioned in section 4.1.1, a convenient way to determine the IRF of the detection system is to quench a fluorophore with the help of a fully saturated potassium iodide solution and to measure the corresponding TCSPC histogram. In this work, all samples are labeled with AL488 or AL647, hence the obvious choice with respect to spectral similarity of IRF and sample would be to quench these dyes. However, AL647 is not sufficiently quenched by KI, hence solutions of quenched AL488 and AT655 are used here instead.

The peak-normalized IRFs measured with the help of the potassium iodide-AL488/AT655 solutions are shown in figure 5.5. The obtained FWHM values of 900 ps indicate that the system was not optimally aligned, as FWHM of 600 ps can be achieved in the optimal case. Interestingly, although the same type of SPAD is used, the IRF profiles for the first and second detector are not identical. Hence, especially with respect to TRA measurements it is important that both IRFs are determined. As a rule of thumb it is said that

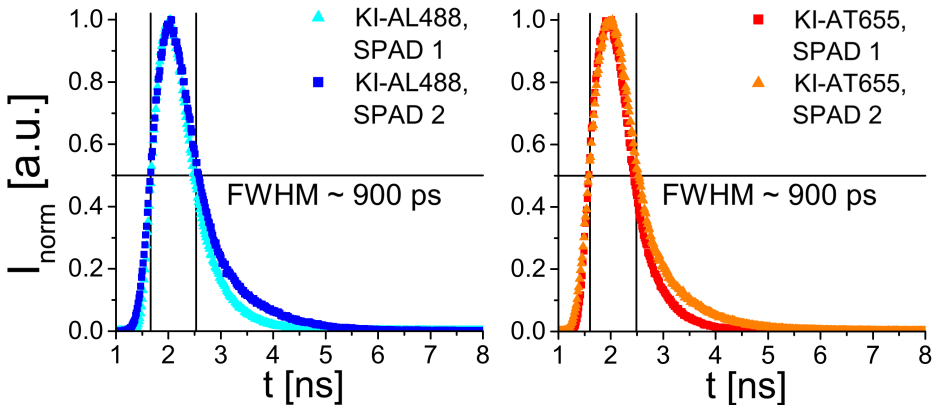

Figure 5.5: IRFs of detection system measured with quenched solutions of AL488 and AT655. For both colors, the FWHM of the IRF lies around 900 ps.

in the optimal case fluorescence lifetimes of $1/10$ of the width of the IRF are resolvable via iterative re-convolution [128]. Consequently, with respect to the confocal setup used in this work, the shortest determinable lifetime lies around 100 ps.

5.3 Determination of depolarization corrections factors

As discussed in section 4.4, the use of a high NA objective (UPLSAPO 60XW considered here) potentially leads to depolarization artifacts in the measured time-resolved anisotropy (TRA) decays. Hence, the TCSPC histograms acquired for the parallelly and perpendicularly polarized fluorescence emission components have to be analyzed with the models given in equation 4.63, which correct for depolarization effects with the help of the parameters k_1 and k_2. In this section, a short protocol shall be given that allows for a reliable determination of k_1 and k_2.

As a first step, a suitable calibration sample has to be found. Having a closer look at equation 4.63, it is clear that a model equation with as little as possible free fitting parameters provides the most reliable results for k_1 and k_2. Therefore, a sample with a mono-exponential lifetime decay in combination with a mono-exponential anisotropy decay has to be found, which makes the freely diffusing fluorophore AL488 one reasonable choice. As a next step, an appropriate solvent has to be selected. In water, the rotational correlation time of AL488 lies around 100 ps, which is close to the temporal resolution limit of the setup (see previous section for details). Additionally, an anisotropy decay with a short rotational correlation time contributes with less photons to the overall decay than a decay with a longer rotational correlation time, which makes a precise determination of its prefactor less likely. On the other hand, the rotational correlation time should

not be too long, as then the available observation window limited by the fluorescence lifetime might be insufficient to determine it accurately. To find the optimal range of rotational correlation times providing the most reliable results of k_1 and k_2, a set of Glycerol solutions (0, 6, 10, 14, 22, 29, 37, 44, 51, 58 wt. % Glycerol added to water) is prepared. Glycerol is a commonly used viscosity enhancer, so its addition to water increases the rotational correlation time of AL488. For each Glycerol concentration the corresponding TRA decays for AL488 are measured, demanding a number of at least 100000 photon counts in the peak of the TCSPC histogram of the parallel component for each data set. It is worth to mention that the size of the employed pinhole does not play a role here. The distance between the upper cover slip surface and the nominal focus position was fixed to 10 µm in all cases.

The optimal parameters k_1 and k_2 are then obtained by fitting the appropriate model 4.63 to the measured TRA decays. It is important to mention that the fundamental anisotropy has to be fixed during the fitting procedure. Here, it was fixed to a value of 0.38 [129]. All other parameters were kept free during the fitting procedure but were limited to reasonable intervals. In all cases, the G-factor was found to lie between 1 and 1.1. The error limits of k_1 and k_2 are determined with the help of a support-plane-analysis (SPA) [43]. This means that the fitting parameter of interest (k_1, k_2) is fixed to an offset value distinct from its optimum while the fitting procedure is run through again. Hence, the other parameters are adjusted until a new minimum of the goodness-of-fit parameter (χ^2_{red}) is found. If the ratio of this new minimum to the optimal minimum does not exceed a specific threshold (F_χ), the offset value is said to be consistent with the data. Then, the parameter of interest is set to another offset value with a larger distance from its optimum and the procedure is repeated. Obviously, the set of offset values consistent with the data defines the confidence interval of the parameter of interest. It should be mentioned that the assessment of the appropriate threshold F_χ is not unequivocally clear [43]. Taking the value predicted by the F_χ-statistic, depending on the number of independent data points and fitting parameters, the threshold value would lie below 1.001 here. However, it is not clear whether all data points contributing to the time-resolved decays are completely independent. Additionally, the error limits obtained using this threshold value appear to be unrealistically small. Here, two confidence intervals are calculated for each parameter, one corresponding to F_χ= 1.005 and one corresponding to F_χ= 1.01, which allows an estimation of the influence of the threshold on the obtained error limits.

Before coming to the experimental results, additionally the theoretical prediction of k_1 and k_2 should be discussed. According to reference [38], k_1 and k_2 can be calculated with the help of the convergence/divergence angle of the laser beam (α) and the maximum angle of photon collection (β). Knowing the NA of the objective and the refractive index n of the solution, β is given by:

$$\beta = \arcsin\left(\frac{NA}{n}\right) \tag{5.1}$$

As the objective is under-filled, α does not coincide with β but has to be determined by means of the beam waist of the focused laser beam. The beam waist can be calculated with the help of the software PSF lab [130]. PSF lab is able to realistically predict the shape of the EID by taking into

account the physical parameters of the objective, for instance its NA and the extent of under-filling of its back-aperture, and the refractive indices of the layers the excitation light passes. Consequently, ω_0 is found to lie around 280 nm. Then, α can be calculated according to [98]:

$$\alpha = \arctan\left(\frac{\lambda_{exc}}{n\pi\omega_0}\right) \tag{5.2}$$

With α and β at hand, the calculation of k_1 and k_2 is straightforward.

The obtained experimental and theoretical values for k_1 and k_2 are shown in figure 5.6, plotted as a function of the respective refractive index of the glycerol solution.

NA	n	k_1	k_2
1.2	1.33	0.54 ± 0.03	-0.31 ± 0.02
	1.37	0.56 ± 0.03	-0.31 ± 0.02
	1.40	0.58 (0.55) ± 0.03	-0.31 (-0.20) ± 0.02
0.3	1.33	0.82 ± 0.03	-0.37 ± 0.03
	1.40	0.82 (0.80) ± 0.03	-0.37 (-0.39) ± 0.03
1.35	1.40	0.53 ± 0.03	-0.29 ± 0.02

Table 5.2: Experimentally obtained depolarization factors for different objectives and solvent refractive indices. The error limits correspond to an SPA threshold of F_χ= 1.01. For the low NA objective, k_1 and k_2 coincide with the values expected for a standard, parallel beam setup. Values in brackets obtained for AT647N in 50 wt. % glycerol.

For n smaller than 1.37 ($\hat{=}$ 29 wt. % Glycerol added), the experimentally determined k_1 and k_2 values have very large error limits and are not reliable. As distinct from that, for n larger than 1.37 the obtained k_1 and k_2 values have sufficiently small error bars. Comparing the theoretical prediction with the measured results, a systematic offset is observed. This is not surprising, as the models used for the calculations do not take into account any experimental imperfections like reflections at interfaces, for instance. Nevertheless, for both correction parameters the theoretical and experimental data points show the same trend. Adding in both cases the same constant offset to the theoretical results to force them to coincide with the stable experimental results, reliable estimations of k_1 and k_2 for n smaller than 1.37 are possible. In table 5.2, the correction parameters are summarized and complemented by k_1 and k_2 obtained for the two other objectives mentioned in section 3.1.

The theoretically predicted depolarization factors for the 633 nm laser deviate from the reported ones by less than 1 % for all numerical apertures considered. Repeating the calibration procedure with AT647N (r_0= 0.37, measured) in a 50 wt. % glycerol solution, for the low NA of 0.3 the obtained k_1 and k_2 values coincide with the ones obtained for AL488 (see table 5.2). As distinct from that, for a numerical aperture of 1.2, only k_1 is consistent with the other value, whereas k_2 is significantly smaller. Hence, although not expected from a theoretical point of view [38], the calibration procedure has to be performed for both spectral ranges.

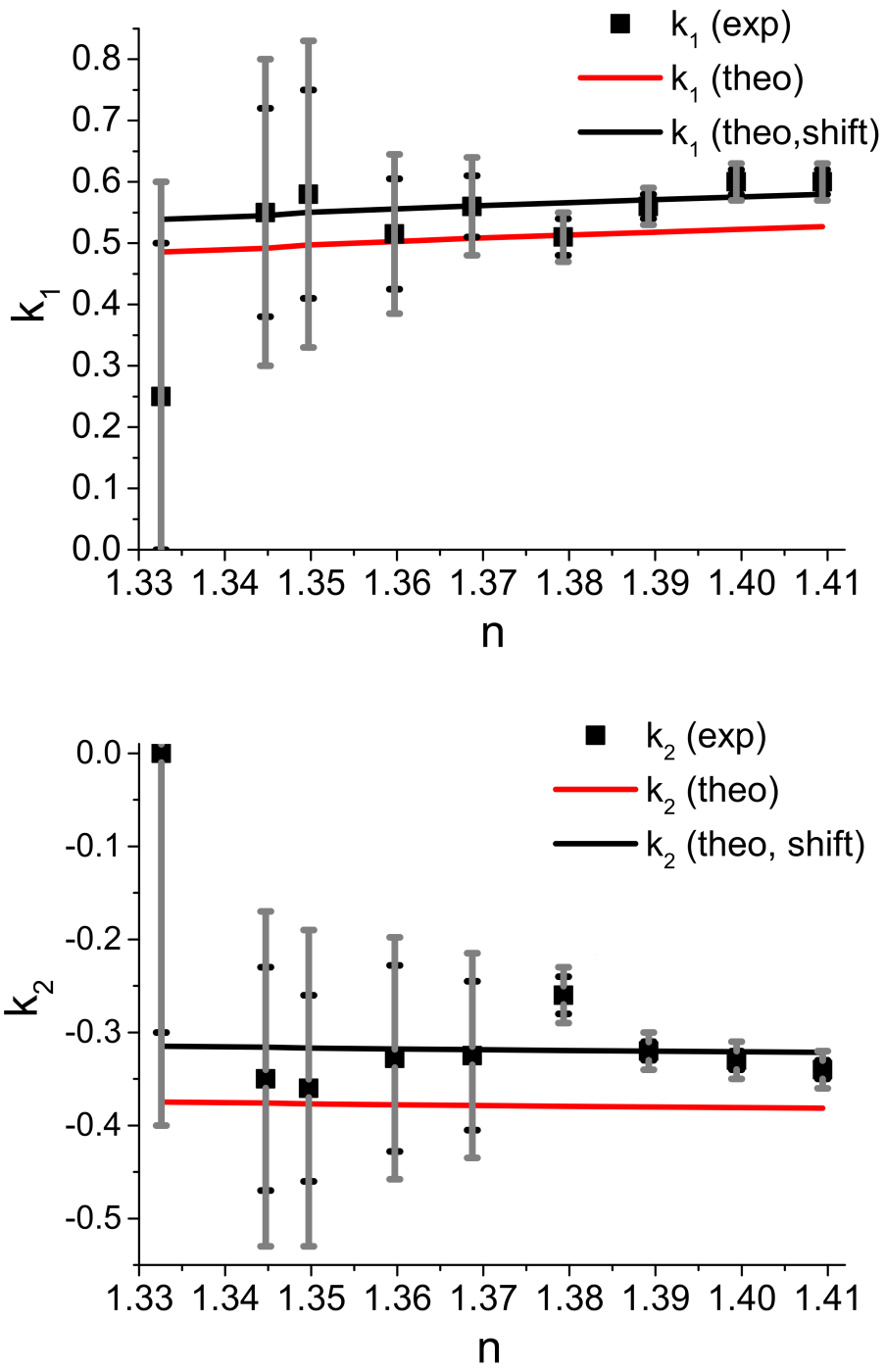

Figure 5.6: Experimental (black squares) and theoretical (red solid line) k_1 and k_2 values as a function of refractive index. Error bars of experimental data correspond to SPA confidence intervals obtained for threshold values of 1.005 (black) and 1.01 (gray). Forcing the theoretical curve to coincide with the experimental results (black solid line), reliable predictions of k_1 and k_2 for n smaller than 1.37 are obtained.

5.4 Quantum yield determination by low-intensity FCS (liFCS)

5.4.1 Theoretical fundamentals of the liFCS approach

The determination of the quantum yield of a sample relative to that of a fluorescent standard with a similar spectrum is based on the comparative measurement of a physical quantity linked to the quantum yield, for instance the integrated fluorescence intensity at identical optical densities (see section 4.1.2). Here, the physical quantity used is the already mentioned molecular brightness (MB), defined as the fluorescence count rate per molecule obtained for a given optical setup, determined in the limit of low-excitation intensities. Assuming that the sample concentration is spatially homogeneous throughout the detection volume, the MB is given by [131]:

$$MB = g \int_V k_{fl,cw/p}(\vec{r}) CEF(\vec{r}) dV \tag{5.3}$$

Here, g denotes the transmission/detection efficiency of the setup at hand, taking into account the spectral transmission functions of all optical elements, the solid angle of emission collection of the objective as well as the detection characteristics of the single-photon avalanche diodes. CEF($\vec{r}$) is the already introduced collection efficiency function of the setup. Lastly, $k_{fl}(\vec{r})$ denotes the spatial fluorescence count rate distribution of a single fluorophore, with subscripts cw and p indicating continuous or pulsed excitation. It can be calculated according to [99, 132]:

$$k_{fl,cw}(\vec{r}) = \frac{\phi_{fl}\sigma_{\lambda_{ex}} I_0 EID(\vec{r})}{1 + \tau_{fl}\sigma_{\lambda_{exc}} I_0 EID(\vec{r}) \left(1 + \frac{k_{isc}}{k_{ph}}\right)} \tag{5.4}$$

$$k_{fl,p}(\vec{r}) = \frac{\phi_{fl} k_{10} \kappa}{1 + \left(\frac{k_{isc}}{k_{ph}}\right) \kappa} \tag{5.5}$$

Here, ϕ_{fl} is the fluorescence quantum yield, $\sigma_{\lambda_{exc}}$ is the absorption cross section at the laser excitation wavelength and EID($\vec{r}$) is the (volume) normalized excitation intensity distribution of the laser beam. I_0 denotes the photon flux of excitation which is determined by the applied laser power. Further on, τ_{fl} indicates the fluorescence lifetime, whereas k_{isc} and k_{ph} are the inter-system crossing and the triplet state depletion rate. The parameter κ is defined as [132]:

$$\kappa = \frac{k_e T_p}{k_s T_r} + \frac{k_e^2}{k_s^2 T_r k_{10}} \frac{[1 - \exp(-k_s T_p)]\,[1 - \exp(-k_{10}\Delta T)]}{[1 - \exp(-k_{10} T_r - k_e T_p)]} \tag{5.6}$$

with the short-hand notations given by:

$$k_e = \sigma_{\lambda_{exc}} I_0 EID(\vec{r}) \qquad k_s = k_e + k_{10} \qquad \Delta T = T_r - T_p \tag{5.7}$$

Here, T_p and T_r are the pulse duration and repetition period of the excitation laser, whereas k_{10} is the effective emission rate already mentioned in section 4.1.1.

In figure 5.7, the theoretically predicted MB of a fluorophore is plotted as a function of the applied laser power for the cases of pulsed and continuous

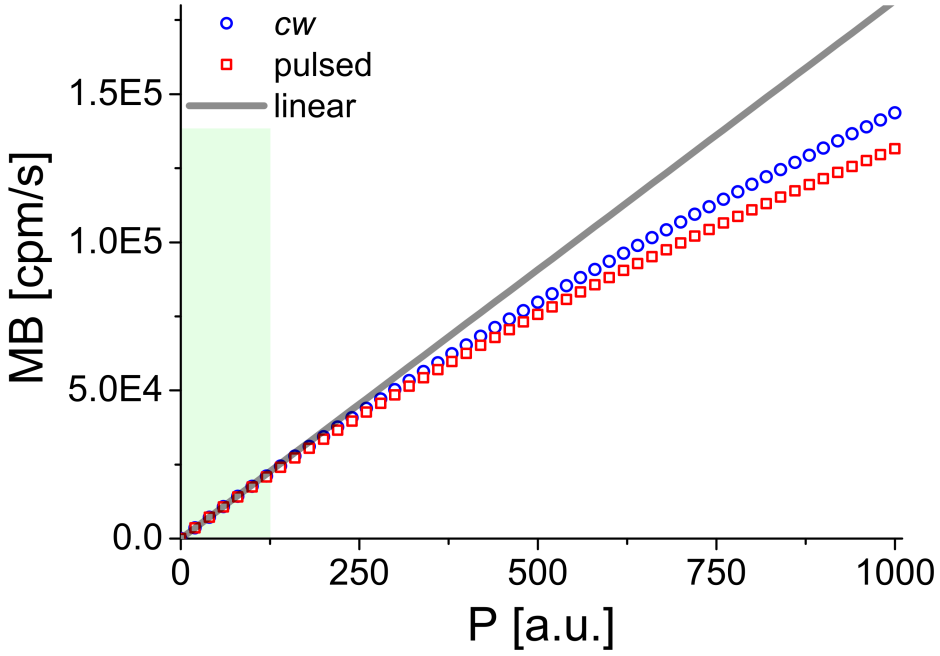

Figure 5.7: MB of AL488 in PBS as a function of excitation power (see equation 5.3). Low excitation intensities (interval shaded light green): curves for continuous (blue bordered circles) and pulsed (red bordered squares) excitation coincide with linear line (grey). Parameters used: τ_{fl}=4.1 ns, $\sigma_{\lambda_{exc}}$=2.79 · 10^{-16} cm^2, ϕ_{fl}= 0.92.

excitation. The inserted fluorescence lifetime, absorption cross-section and quantum yield value coincide with the manufacturer's specifications for AL488 in PBS and are indicated in the figure caption. The ratio of the intersystem-crossing to the triplet depletion rate is fixed to 10, which is equal to or higher than the values expected for the dyes used in this work [131, 133, 134]. The transmission efficiency parameter g is set to 0.1, which is, as shown later, comparable to the values expected for the setup at hand. The EID is approximated by a Gaussian laser beam intensity distribution [98]. In accordance with the value introduced in section 5.3, the beam waist ω_0 is assumed to be ≈ 280 nm. The laser power is converted into a photon flux using the conversion factor (λ_{exc}=481 nm) determined in section 5.1.2. The CEF($\vec{r}$) is calculated with the help of a semi-geometric approach [99, 101], inserting a pinhole diameter of 30 µm, an NA of 1.2 and a magnification of 60 (values for default objective). T_p is fixed to 70 ps and T_r to 50 ns, corresponding to an excitation frequency of 20 MHz. To make the results of pulsed and *cw*-excitation comparable, the pulsed laser power is corrected by a factor T_r/T_p.

As shown in figure 5.7, in a regime of low excitation intensities (shaded in light green) the curves for *cw* and pulsed excitation coincide and depend linearly on the applied laser power according to:

$$\lim_{I_0 \to 0} MB = \left[g \phi_{fl} \sigma_{\lambda_{exc}} \int_V MDF(\vec{r}) dV \right] I_0 \tag{5.8}$$

Here, the product of EID($\vec{r}$) and CEF($\vec{r}$) is substituted by the already mentioned molecule detection function, MDF($\vec{r}$). The parameters in square brackets form the slope of the linear curve, in the following denoted as m. Comparing this slope to the slope obtained for a reference sample with a

similar spectrum, the unknown quantum yield can be determined according to:

$$\boxed{\phi_{fl,s} = \frac{m_s}{m_r}\frac{g_r}{g_s}\frac{\epsilon_{\lambda_{exc},r}}{\epsilon_{\lambda_{exc},s}}\frac{MDF_{int,r}}{MDF_{int,s}}\phi_{fl,r}} \tag{5.9}$$

Here, subscript r indicates the reference sample, whereas subscript s denotes the sample of unknown ϕ_{fl}. The absorption cross-section is replaced by the molar absorption coefficient according to equation 4.12.

5.4.2 liFCS approach: experimental realization

Determination of the molecular brightness

The slope m of the MB-curve is obtained by linear least-squares fitting. Experimentally, the MB-curve is determined by taking the ratio of the background corrected mean fluorescence count rate of a sample, $\bar{F}_c$, to the background corrected mean number of fluorescent particles present in the detection volume, $\bar{n}_c$. $\bar{F}$ is obtained by means of the binned fluorescence intensity time trace (see figure 5.8). The influence of background is taken into account

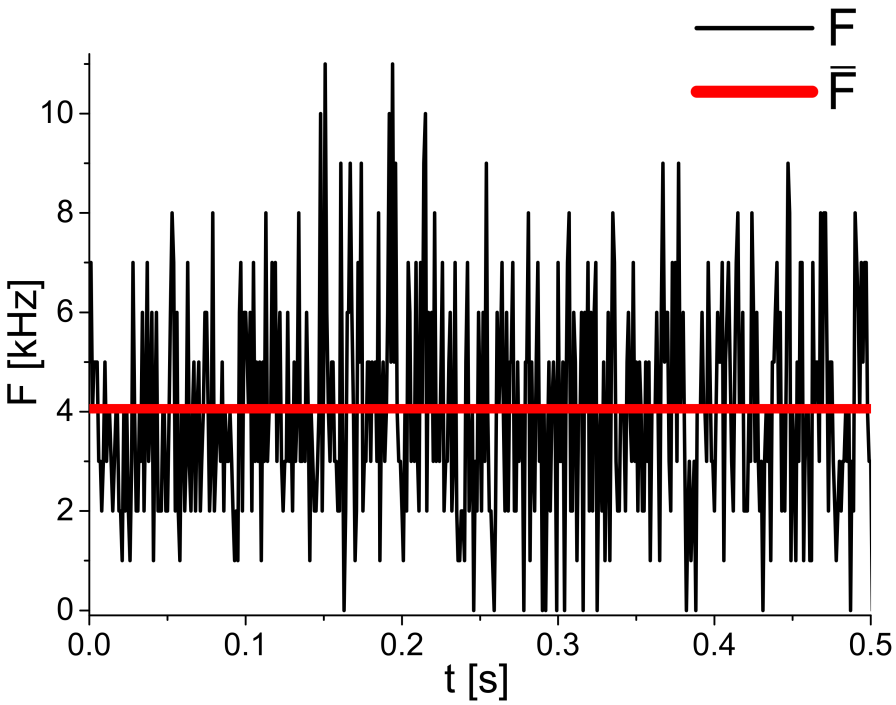

Figure 5.8: Time trace of Fluorescein in 0.1 M NaOH. Mean fluorescence count rate $\bar{F}$ shown in red.

according to:

$$\bar{F}_c = \bar{F} - \bar{BG} \tag{5.10}$$

The mean background count rate $\bar{BG}$ is obtained by measuring pure solvent, applying the same excitation intensity used to measure the actual sample. The parameter $\bar{n}$ is determined by FCS. Again, the influence of the mean background count rate $\bar{BG}$ has to be taken into account [97, 135]:

$$\bar{n}_c = \frac{\bar{n}}{(1 + \frac{\bar{BG}}{\bar{F}_c})^2} \tag{5.11}$$

The MB is then given by:

$$MB = \frac{\bar{F}_c}{\bar{n}_c} \tag{5.12}$$

Obviously, the reliability of the determined MB depends on the reliability of the determined $\bar{F}_c$ and $\bar{n}_c$. Hence, systematic concentration drifts due to unspecific sticking of the specimen to the coverslip surface should be avoided by using appropriate surface preparation protocols (see section 2.5). Additionally, $\bar{n}$ should not be biased by systematic discrepancies between fitted model and experimental data, meaning that the Gaussian approximation of the MDF-volume has to be valid. According to previous findings [97], the combination of an under-filled objective back-aperture and a small pinhole diameter is the one that most likely meets this condition, consequently all liFCS measurements are performed with a 30 µm pinhole. Another problematic issue is the correlation between $\bar{n}$ and the triplet fraction parameter T. Its dependency on the excitation intensity is given by [43]:

$$T = \frac{\sigma_{\lambda_{exc}} \left(\frac{I_0}{\pi\omega_0^2}\right) k_{isc}}{\sigma_{\lambda_{exc}} \left(\frac{I_0}{\pi\omega_0^2}\right) (k_{isc} + k_{ph}) + k_{ph}(k_{isc} + k_{10})} \tag{5.13}$$

The triplet fraction as a function of the excitation power and the ratio k_{isc}/k_{ph} is shown in figure 5.9, using the parameters of AL488 in PBS (see figure caption for details). The beam waist is fixed to ω_0=280 nm as before. The ratio of k_{isc} to k_{ph} is fixed to 10 and 40 to show its impact on the corresponding triplet fraction buildup. Applying excitation powers below 100 a.u., the calculation shows that triplet fractions below 10 % are obtained even in the (extreme) case when k_{isc} is fourty times larger than k_{ph}. As a matter of fact, in the more realistic case of a ratio of 10, the triplet fraction lies below 3 %. Hence, the triplet fraction showing up in the low-excitation intensity FCS curves is hardly visible by eye and can, when treated as a free parameter during the fitting procedure, fluctuate strongly in terms of its fitting value. As a consequence, the correlated parameter $\bar{n}$ (and concurrently the MB) can be significantly biased. This problem can be circumvented by limiting the range of values of T or even fixing T to one specific value during the fitting procedure. Alternatively, the FCS curves can be analyzed without taking into account any triplet fraction using a model function describing pure diffusion only 4.53. Since the difference in the outcome parameter $\bar{n}$ lies below 1%, the latter option is preferred in this work. An exemplary fitting result is shown in figure 5.10 for Fluorescein in 0.1M NaOH.

An exception to the previously mentioned rule are samples containing fluorophores belonging to the family of carbocyanine dyes like Cy5 or AL647, as these are prone to a mechanism called photo-induced cis/trans-isomerization [136]. Continuously flipping from a dark cis into a fluorescent trans state on a µs timescale, it has been shown that the kinetic rates but not the absolute dark state fractions depend on the impinging photon flux [137]. Consequently, even for FCS-curves originating from low-excitation intensity measurements, a constant dark-state fraction shows up which is clearly visible by eye and well-separated from the diffusion-related part of the curve. Therefore, all FCS-curves of cyanine dyes are fitted without any constraints using the model function given by equation 4.55. Although this model is primarily intended to fit FCS curves with triplet transitions, it is sufficient to determine $\bar{n}$ also in this case.

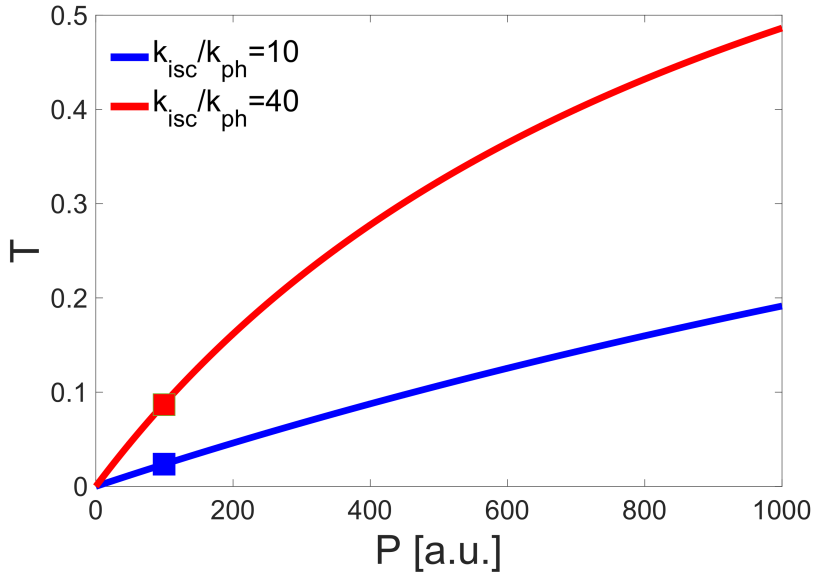

Figure 5.9: Triplet state fraction T as a function of the excitation power for the case of AL488 in PBS. The ratio of k_{isc} to k_{ph} is varied from 10 to 40. At an excitation power of 100 a.u. (highlighted by squares) , corresponding to the upper limit of the predicted low intensity/linear regime, the triplet fraction is smaller than 10 % for a ratio of 40, and even smaller than 3 % for a ratio of 10. Parameters used: k_{10}=2.44 10^8 1/s, $\sigma_{\lambda_{exc}}$=2.79 $\cdot$ 10^{-16} cm^2.

Finding the linear regime experimentally

In this section, the theoretical prediction of the linear regime (see section 5.4.1) is compared to experimental values. For that, MB-values obtained for AL488 and AL647 in PBS and AT488 and AT655 in water are plotted against the applied laser power. The results are shown in figure 5.11, overlaid with the corresponding linear responses shown as solid lines. The discrepancy between the slopes for *cw* and pulsed excitation for AL488 and AT488 are due to different conversion factors for continuous and pulsed excitation (see section 5.1.2 for details). Obviously, in all cases an upper limit of even $\approx$ 150 a.u. would still be sufficient to validate the use of equation 5.9. However, throughout this work an upper limit of 100 a.u. is specified, avoiding errors when measuring fluorophores with longer lifetimes or higher k_{isc} to k_{ph} ratios as assumed in section 5.4.1. Additionally, comparing the slope of the theoretically predicted MB-curve of AL488 shown in figure 5.7 with the slope of the experimentally determined curve depicted in figure 5.11, an overall quantum detection efficiency of $\approx$ 4 % can be assessed.

Determination of the absorption coefficient

In terms of the determination of the absorption coefficient $\epsilon_{\lambda_{exc}}$, *cw*- and pulsed excitation have to be considered individually. However, the first step to be taken in both cases is to measure the absorption spectrum of the sample of interest and to normalize the obtained spectrum to a maximum value of one. Subsequently, the normalized spectrum has to be multiplied by the maximum absorption coefficient $\epsilon_{\lambda_{max}}$ known from the literature. Then, this product spectrum is multiplied by the area normalized spectral profile of the irradiating laser. Integration of the obtained result provides the desired

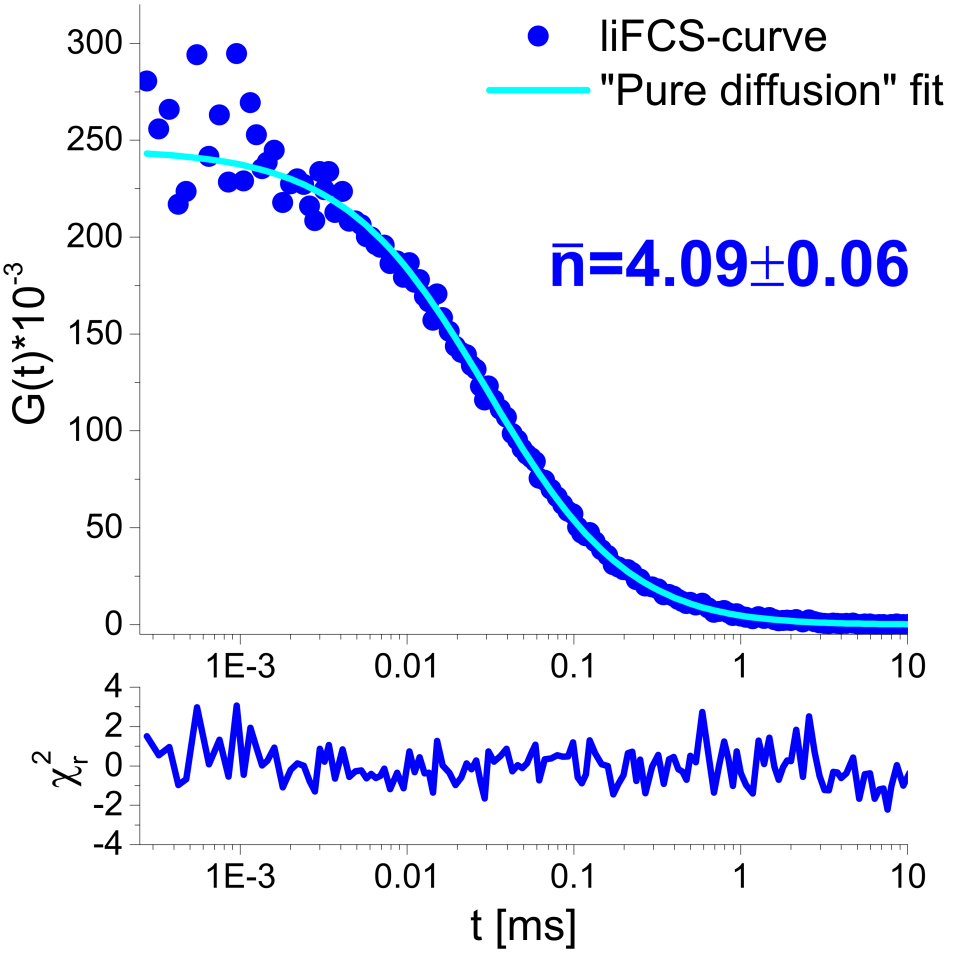

Figure 5.10: Top: Correlation-curve of Fluorescein in 0.1 M NaOH (laser power= 30 a.u.) analyzed using the pure diffusion model 4.53. The fitted model curve is given in cyan. Bottom: Weighted reduced residuals.

value of $\epsilon_{\lambda_{exc}}$. In the case of *cw*-excitation, the profiles of the lasers used in this work have a spectral width smaller than one nm. Therefore, simply determining the relative OD-value of the normalized absorption spectrum at the maximum of the laser excitation profile and multiplying it with $\epsilon_{\lambda_{max}}$ provides an adequate approximation of the real $\epsilon_{\lambda_{exc}}$. An exemplary result is depicted in figure 5.12 for AL488 in PBS, assuming $\epsilon_{\lambda_{max}}$=73000 $M^{-1}cm^{-1}$. The values for $\epsilon_{\lambda_{exc}}$ obtained in the two previously discussed ways differ by less than one permille in the case of *cw*-excitation. As distinct from that, using pulsed excitation the laser profile gets broader and the real and the approximated value differ by $\approx 2\,\%$, which was considered to be sufficiently accurate throughout this work.

Determination of the transmission/detection efficiency parameter

As a first step, the photon collection efficiency of the objective (CEO) is determined. As long as it is free to rotate on the timescale of emission, an excited molecule can be treated as a an isotropic emitter. This means that the radiated energy is homogeneously distributed over the surface of a unit sphere surrounding the emitter. Knowing that all of the energy covers an area of 4π, the fraction of energy that gets collected by the objective is

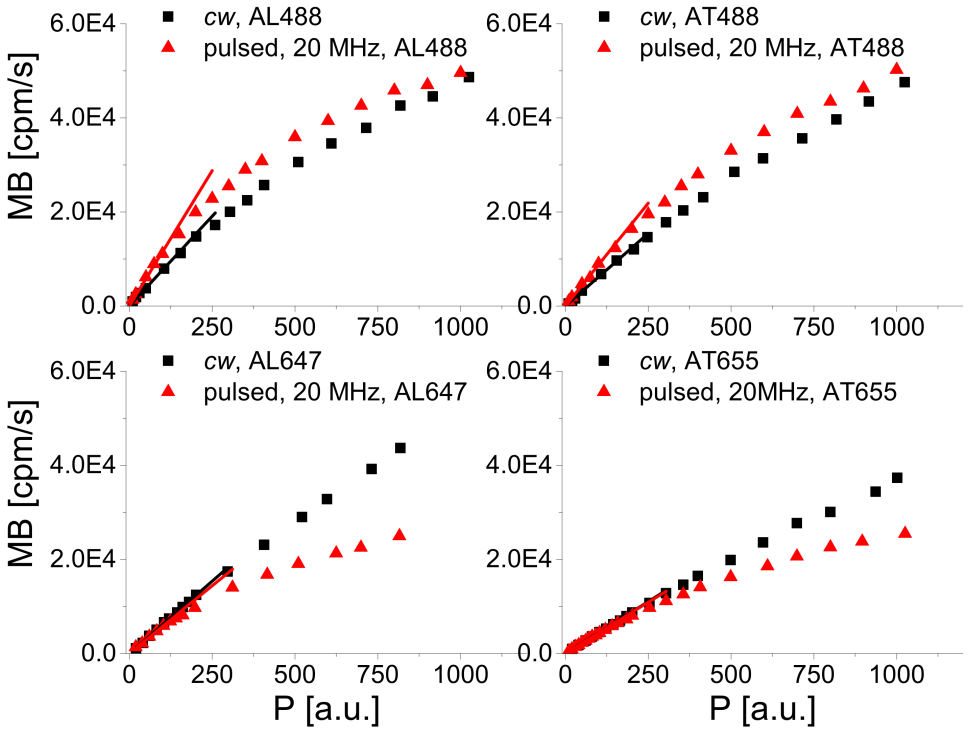

Figure 5.11: MB of AL488 and AL647 in PBS (left side) and AT488 and AT655 in water (right side) as a function of applied laser power (Red triangles: pulsed excitation, 20 MHz. Black squares: *cw*-excitation). Red and black solid lines represent the corresponding linear approximations. An upper power limit of ≈ 100 a.u. guarantees the validity of the linear approximation.

determined by the solid angle limited by its NA. Therefore, the CEO can be calculated according to:

$$CEO = \frac{2\pi\left[1 - \cos(\arcsin(\frac{NA}{n}))\right]}{4\pi} \tag{5.14}$$

For the UPLSAPO60XW, the CEO equals 0.28, meaning that ≈ 30 % of the emitted photons are collected by the objective.

To which extent the collected fluorescence emission is attenuated by the components downstream the light path is determined by the respective wavelength dependent transmission/detection efficiency spectra having values between 0 and 1. By multiplying the transmission/detection efficiency spectra of all components with each other, a system specific overall transmission/efficiency spectrum T_λ can be calculated. Additionally, the fluorescence spectrum of the respective fluorescent sample has to be measured and normalized to an integrated intensity of one. The normalized spectrum is then multiplied with the transmission/efficiency spectrum T_λ. Finally, the resulting product is integrated over all wavelengths. To calculate the overall transmission/detection efficiency parameter g, the integral value has to be multiplied with the CEO.

Exemplarily, the complete determination of g is depicted in figure 5.13 for AL488 in PBS. The obtained value of g ≈ 11 % does not coincide with the overall quantum detection efficiency of ≈ 4 % determined in section 5.4.2. This is not surprising, as other sources of photon loss like reflection at interfaces or slightly misaligned components are not taken into account

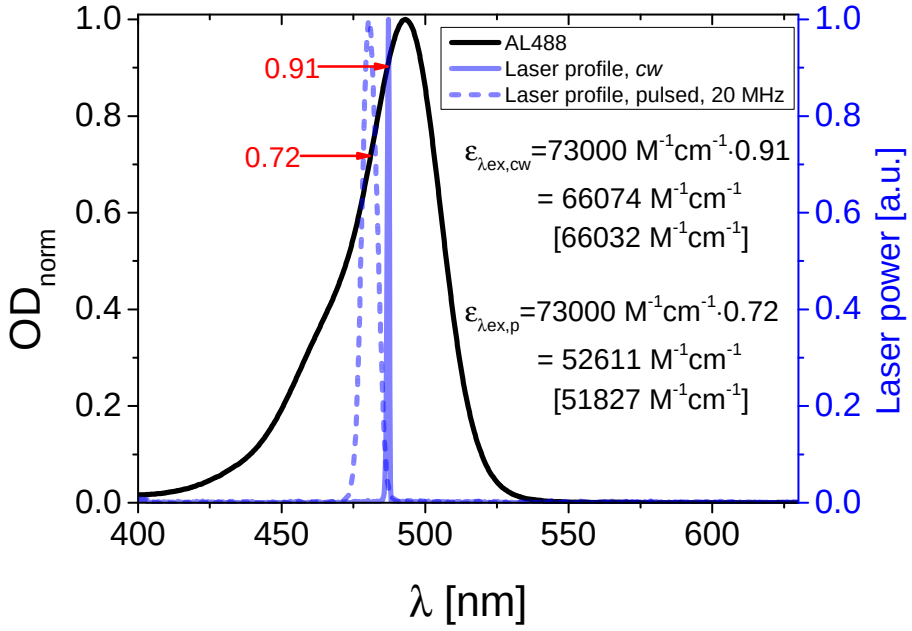

Figure 5.12: Determination of the absorption coefficient $\epsilon_{\lambda_{exc}}$ for AL488 in PBS. The solid black line depicts the normalized absorption spectrum, the laser profiles are shown as semi-transparent blue dashed (pulsed) and solid (*cw*) lines. In square brackets, $\epsilon_{\lambda_{exc}}$ obtained by taking into account the actual laser profile is given. $\epsilon_{\lambda_{exc}}$ obtained by multiplication of the relative OD-value (at λ_{exc}) with $\epsilon_{\lambda_{max}}$ are shown above.

here. However, as reference and sample are measured using the same setup, these effects are negligible as they cancel out.

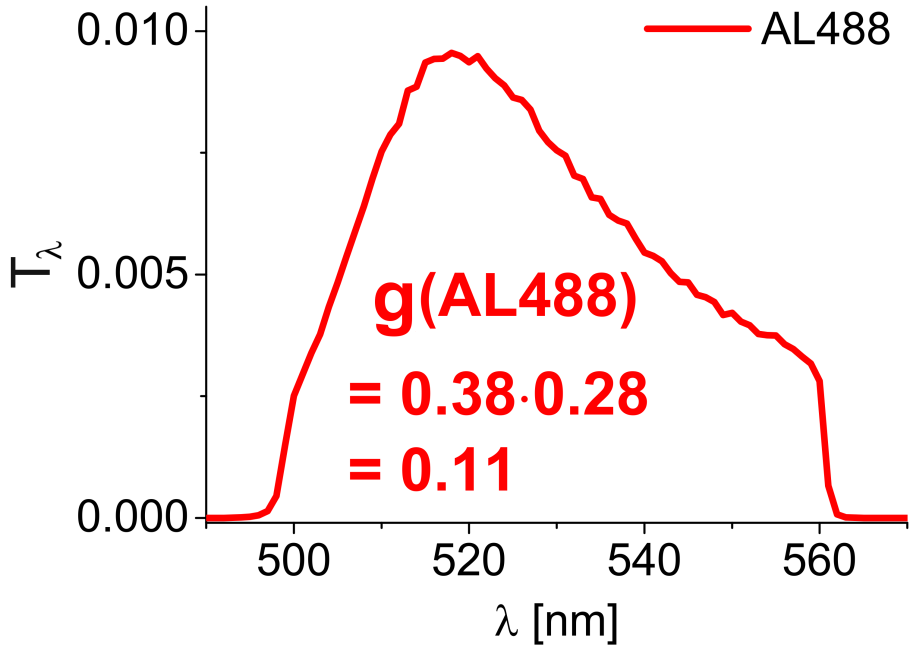

Figure 5.13: Product of transmission function T_λ and normalized fluorescence emission spectrum of AL488 in PBS (red solid line). Integrating the product and multiplying it with the CEO, the parameter g is obtained.

5.4.3 The MDF: case differentiation

The last parameter entering equation 5.9, the integrated molecule detection MDF_{int}, has to be discussed considering two different situations. The first situation is given when reference and sample solution have a refractive index of around 1.33, which is the solvent refractive index most confocal microscopes equipped with water-immersion objectives are designed for (design conditions). Hence, again assuming that the objective is under-filled and the pinhole size is small, the MDF volume is well-approximated by a Gaussian distribution and the obtained liFCS curves are likely to provide reasonable results. Additionally, as reference and sample have similar spectra and are measured employing the same setup, the corresponding integrated MDF-values are equal and cancel out in equation 5.9:

$$\boxed{\phi_{fl,s} = \frac{m_s}{m_r}\frac{g_r}{g_s}\frac{\epsilon_{\lambda_{exc},r}}{\epsilon_{\lambda_{exc},s}}\phi_{fl,r}} \tag{5.15}$$

Consequently, in this case the quantum yield determination is straightforward.

Refractive index mismatch and EID: theoretical insights

In the second case, the sample of interest is assumed to have refractive index different from 1.33 (non-design conditions). As the objective is not designed for this mismatch, it can potentially induce a severe distortion of the MDF [52]. To get an impression of the extent of this distortion, xz-cross-sections of the EID are calculated with the help of the already mentioned software PSF lab [130]. Again, in addition to the objective parameters, the thickness and the refractive index of each layer the excitation light passes are considered in all calculations. Here, the refractive indices of the immersion medium and the cover slip are assumed to match the design conditions, just as the coverslip thickness. The latter assumption is justified by the use of high precision cover slips in all measurements (thickness= 170 $\pm$ 5 µm) and a thorough adjustment of the correction collar of the objective to further compensate for variations in thickness. Consequently, only the solvent refractive index and the nominal focus position are varied, the latter being equal to the distance of the non-aberrated focus location to the cover slip surface along the z-axis. The obtained results for the blue laser are depicted in figure 5.14. Refractive indices of n= 1.333 and n= 1.40 and nominal focus positions of 10 or 20 μm are considered. The origin of the calculated two-dimensional xz-contour plots always coincides with the assumed nominal focus position. For n=1.333, the actual focus position corresponds to the nominal one (design conditions, no aberration effects), whereas the refractive index mismatch leads to a relative shift of the actual focus position away from the cover slip surface. Naturally, this effect is enhanced with increasing nominal focus positions. The radial extent of the intensity distribution is rather unaffected by the refractive index mismatch and still shows a good agreement with the fitted Gaussian profile (red line in the contour profile plots). As distinct from that, the Gaussian distributions fitted to the Lorentzian intensity profiles along the z-axis indicate that the axial extent is significantly enhanced with increasing refractive index and cover slip-focus distance.

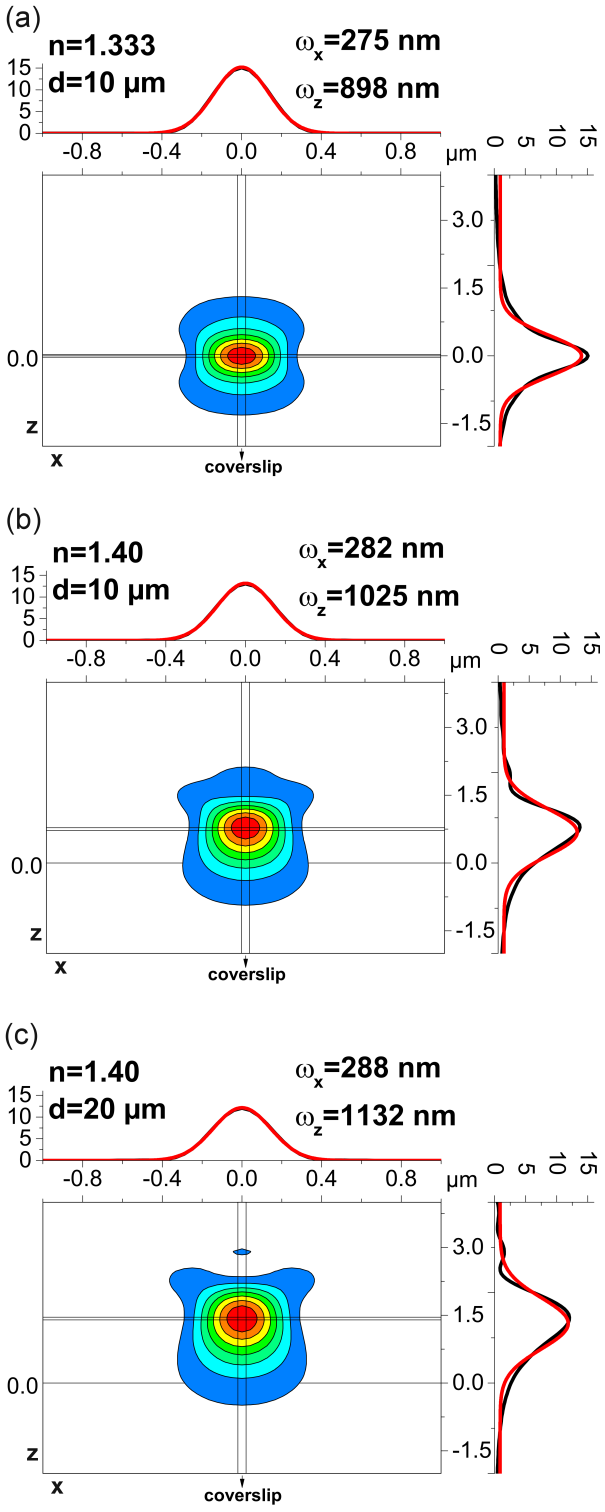

Figure 5.14: Calculated EID xz-cross-sections for λ_{exc}= 487 nm; $\omega_{x,z}$ denote the $1/e^2$-radii of Gaussian distributions (red line) fitted to contour-profile data points (black line). (a): non-aberrated EID. (b) Solvent refractive index of n=1.40. Focus position of 10 µm leads to slight increase in axial extension, whereas radial extension does not change significantly. (c) Solvent refractive index of n=1.40. Focus position of 20 µm enhances the refractive index mismatch effect, specifically axial extension of EID is significantly increased as compared to aberration-free conditions.

As the MDF is determined not only by the EID, the calculated results shall only provide a qualitative demonstration of the effects of a refractive index mismatch. However, it is clear that, to minimize the effects of the refractive index mismatch, the cover slip-focus distance has to be kept to the shortest experimentally reasonable value.

Refractive index mismatch and *MDF*: experimental results

The next step now is to show experimentally that the liFCS curves obtained under these non-ideal conditions are still analyzable assuming a Gaussian shaped volume without a significant deterioration of the goodness-of-fit. Only then it is likely that the obtained fitting parameters are still reliable. Following the previous theoretical considerations, a nominal focus position of 10 µm is selected for all liFCS measurements, and again a pinhole with a small diameter of 30 µm is employed. As a test sample, AL488 in solutions with different amounts of Glycerol added is selected. Besides its already mentioned versatility as a viscosity enhancer, Glycerol simultaneously severely affects the refractive index of aqueous solutions. To determine the radial and axial extension of the effective liFCS volume, the diffusion coefficient of AL488 in each of the Glycerol solutions has to be known [138]. As the diffusion coefficient depends on the solvent viscosity, an equation is needed that predicts the diffusion coefficient as a function of the viscosity.

According to the Einstein-equation, the translational diffusion coefficient of a particle is related to its mobility µ according to [139]:

$$D_t = k_B T \mu \tag{5.16}$$

Replacing µ by the inverse of the friction coefficient known from Stokes-law [140], the Stokes-Einstein equation is obtained:

$$D_t = \frac{k_B T}{6\pi\eta r_h} \tag{5.17}$$

Here, η is the solvent viscosity and r_h is the hydrodynamic radius of the tracer molecule. On the other hand, the relation between the solvent viscosity and the rotational diffusion coefficient is described by the Stokes-Einstein-Debye-Equation [139]:

$$D_r = \frac{k_B T}{8\pi\eta {r_h}^3} \tag{5.18}$$

Obviously, equation 5.17 provides the needed relation between D_t and η. η is easily determined by measuring the refractive index of the Glycerol solution and employing the refractive index versus viscosity table given in [141]. However, it should be noted that equations 5.17 and 5.18 are only valid under two assumptions. First, the tracer particle should have a close to spherical shape. Secondly, the surrounding solvent should be a continuum, an assumption that becomes reasonable if the components of the solvent are smaller than the tracer molecule. According to observations in our lab, the rotational diffusion of a tracer molecule is more sensitive to deviations from these assumptions than the translational diffusion. Therefore, time-resolved anisotropy measurements are performed to determine the rotational diffusion coefficient of AL488 as a function of the viscosity of each Glycerol solution. TRA is a specifically useful measurement technique in this respect,

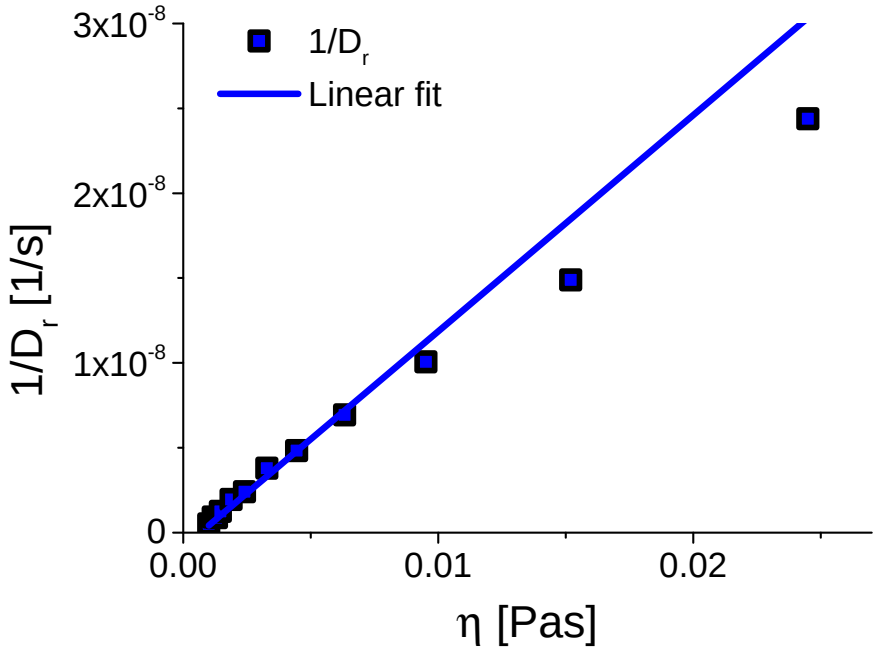

Figure 5.15: Inverse rotational diffusion coefficients of Al488 in solutions glycerol solutions, plotted as a function of solvent viscosity. The linear relationship between $1/D_r$ and η predicted by equation 5.18 is valid up to $\approx$ 10 mPas.

as it is independent from the MDF. The results are depicted in figure 5.15. Verifying that the measured rotational diffusion coefficients obey the Stokes-Einstein-Debye equation is a strong indication that also the Stokes-Einstein equation should be applicable to calculate the required translational diffusion coefficients of AL488 in Glycerol solutions. As is shown in figure 5.15, up to a viscosity $\approx$ ten-times higher than the one of pure water the obtained $1/D_r$-values obey equation 5.18. This is not surprising, as the size of Glycerol (r=0.3 nm, MW=92 Da) is small as compared to AL488 (r=0.6 nm, MW=643 Da) as is required for a continuous solvent. With the help of the slope of the fitted linear curve, a hydrodynamic radius of r_h=(0.59 $\pm$ 0.01) nm is obtained for AL488, which coincides with a reference value of r_h=0.58nm found in the literature [142]. Hence, the viscosities of the Glycerol solutions appear to be determined correctly. With the help of equation 5.17, the corresponding translational diffusion coefficients of AL488 are calculated. These are summarized in table B.1 in the Appendix.

With the help of the obtained D_t values, the liFCS curves of AL488 in Glycerol are analyzed. The goodness of fit stays constant in the course of the measurements, meaning that the assumption of a Gaussian volume is still valid. Additionally, the geometric extent of the liFCS effective volume quantified by the parameters ω_0 and κ is determined. The results are shown in figure 5.16. Obviously, within the error limits ω_0 and κ stay constant over the whole refractive index regime considered here. Comparing these results to the ones obtained for the calculated EID distributions discussed in section 5.4.3, not surprisingly the introduction of the small pinhole appears to suppress the axial elongation introduced by the refractive index mismatch. In summary, it can be said that using a pinhole with a diameter of 30 µm and measuring at a nominal focus position of 10 µm, the refractive index mismatch is negligible in terms of the geometric extent and shape of the

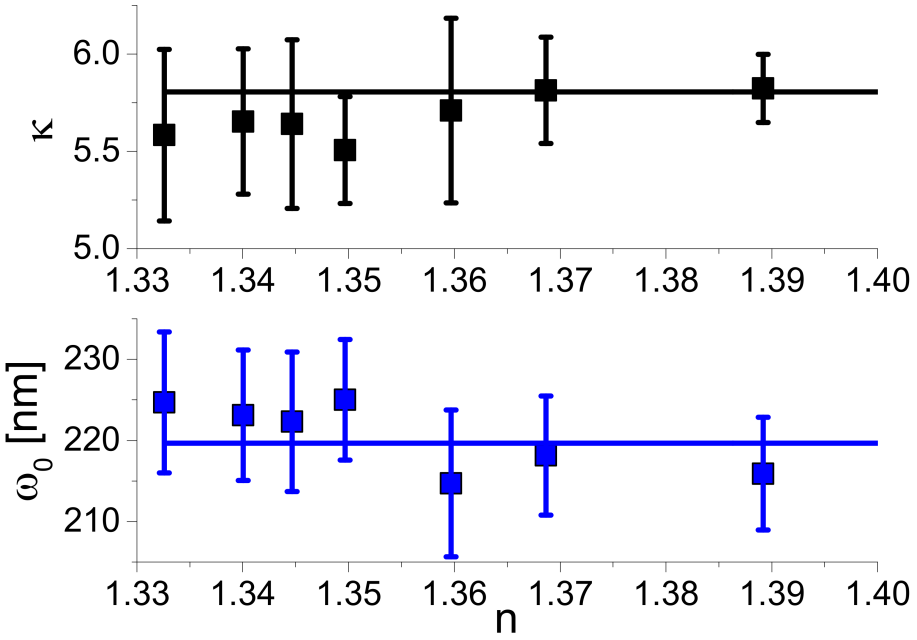

Figure 5.16: ω_0 and κ, determined with the help of AL488 in glycerol solution, as a function of the refractive index the solvent refractive index. Within the given error limits both parameters stay constant over the considered refractive index regime.

MDF-volume.

Refractive index mismatch and *MB*: experimental results

As is shown in figure 5.14, a refractive index mismatch leads to a diminished peak excitation intensity in the focus region. Hence, although the same laser power is set up, the sample gets less efficiently excited. Obviously, this leads to a decrease of the obtainable MB. To take into account all processes leading to a loss of photons, the integrated MDF is replaced by an effective integrated molecule detection function, further on abbreviated as MDF^*_{int}. Re-arrangement of equation 5.9 then leads to a quantification of the $MDF^*_{int,s}$ obtained under non-ideal conditions in relation to the $MDF^*_{int,r}$ obtained under design conditions:

$$\frac{MDF^*_{int,s}}{MDF^*_{int,r}} = \frac{\phi_{fl,r}}{\phi_{fl,s}} \frac{m_s}{m_r} \frac{g_r}{g_s} \frac{\epsilon_{\lambda_{exc},r}}{\epsilon_{\lambda_{exc},s}} \tag{5.19}$$

To determine this ratio experimentally, AL488/AL647 dissolved in water is selected as reference sample measured under design conditions and AL488/AL647 dissolved in Glycerol solutions is taken as sample measured under non-ideal conditions. Obviously, to calculate equation 5.19 the quantum yield of each sample has to be known beforehand. Here, it is determined with the help of the standard method (see section 4.1.2 for details). All other parameters entering equation 5.19 are obtained following the protocols given in section 5.4.2. The determined ratios are depicted in figure 5.17. Apparently, MDF^*_{int} decreases with increasing refractive indices for both excitation colors, but the effect is stronger for the blue laser. As no spectral dependency is expected, this is probably a result of the pinhole alignment. However, the obtained results have very large error-bars, so inserting them into equation 5.9 as a kind of calibration factor leads to large errors in the quantum

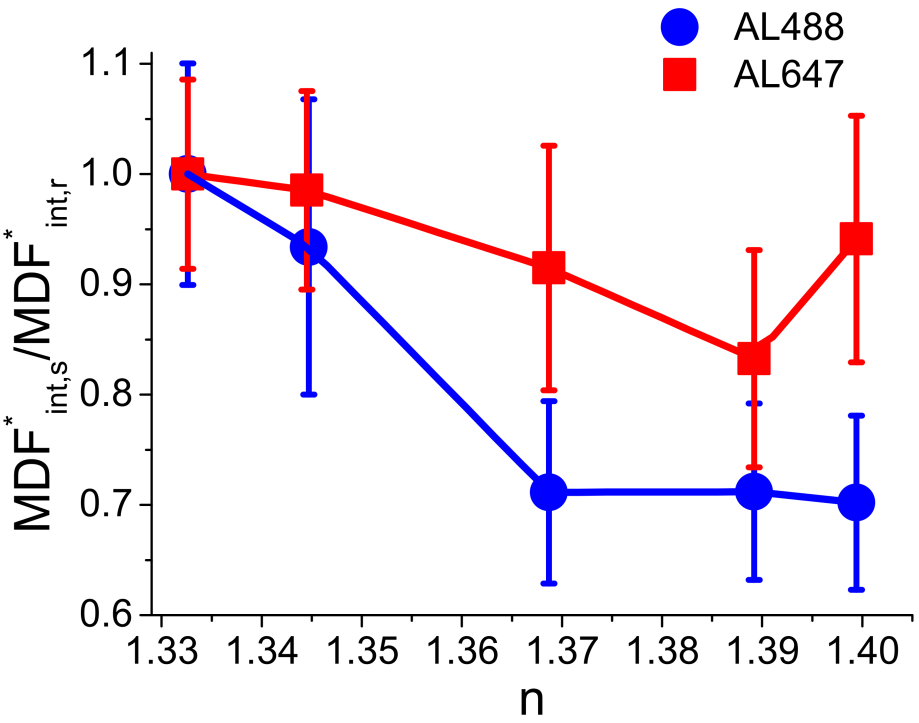

Figure 5.17: Ratio of $MDF^*_{int,s}$ to $MDF^*_{int,r}$, determined using glycerol solutions of AL488 and AL647, as a function of the solvent refractive index. In both cases, MDF^*_{int} decreases with increasing n, but the effect is more pronounced for the blue laser.

yield determination. Therefore, a more reasonable strategy is to measure sample and reference in solvents of same refractive index, leading to the applicability of equation 5.15 also under non-design conditions. As their corresponding quantum yields have been determined already, AL488 and AL647 in glycerol solutions are used as reference samples in this work. The quantum yields are summarized in table 5.3.

Within the refractive index regime considered here, the quantum yield of AL488 stays constant within the given error limits. As distinct from that, AL647 shows a significant increase of ϕ_{fl} with increasing amounts of Glycerol added to the solution. This is most probably a consequence of the already mentioned cis-trans isomerisation commonly found in the family of cyanine-dyes, which shows a dependency on the solvent viscosity. As the rate describing the transition from the fluorescent trans to the dark cis state appears to be more reduced by an enhanced viscosity than the back-reaction, the average occupation of the dark state decreases and the fluorescence quantum increases [143].

5.4.4 Experimental validation of the liFCS approach

In this section, a series of proof-of-principle measurements is performed to validate the liFCS based quantum yield determination. For measurements under design conditions, Fluorescein (FLUO) in 0.1 M NaOH and Atto 655 (AT655) in water are chosen as reference fluorophores to determine the quantum yields of AL488 and AL647 in PBS and AT488 in water. While the other samples appeared to be stable at least for a few days, fluorescein

wt. % Glycerol	n	ϕ_{fl} AL488	ϕ_{fl} AL647
0	1.333	0.92±0.0	0.33±0.0
6	1.340	0.93±0.02	0.35±0.01
10	1.345	0.92±0.02	0.37±0.01
14	1.350	0.92±0.02	0.39±0.01
22	1.360	0.93±0.02	0.43±0.01
29	1.369	0.93±0.02	0.41±0.01
37	1.379	0.92±0.02	0.45±0.01
44	1.389	0.91±0.02	0.44±0.01
51	1.399	0.94±0.02	0.45±0.02
58	1.409	0.94±0.02	0.47±0.02

Table 5.3: Fluorescence quantum yields of AL488 and AL647 in glycerol solutions, determined with the standard method.

solutions were not stable over time and were prepared freshly before each measurement [144]. Under non-design conditions, AL488 and AL647 in glycerol solutions (n=1.34 and n=1.37) are selected as reference fluorophores, facilitating the specification of the quantum yields of AT488 and AT655 in the same solvent.

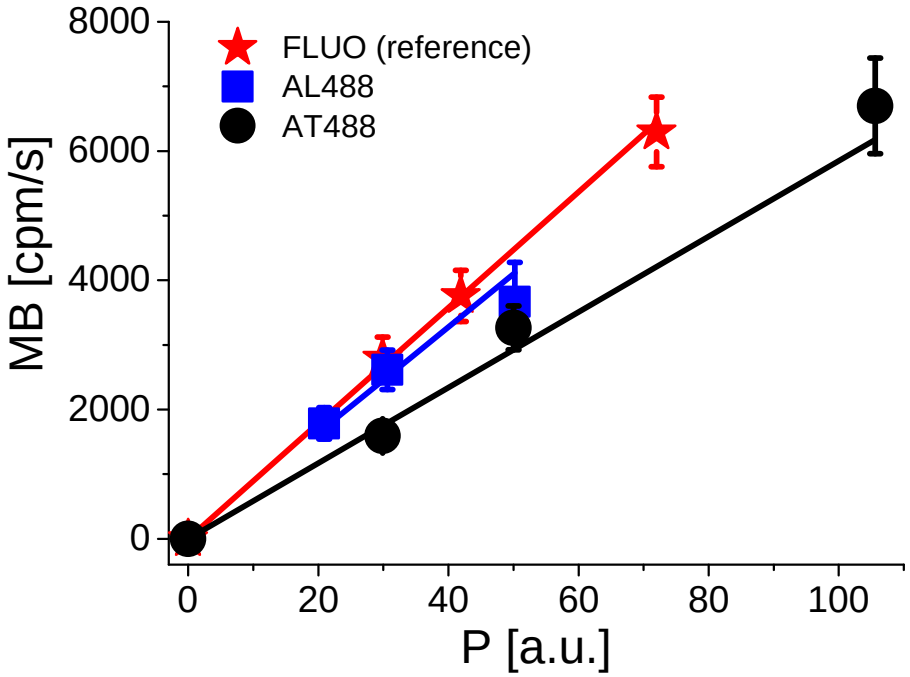

Figure 5.18: liFCS MB-curves for FLUO in 0.1 M NaOH, AL488 in PBS and AT488 in water. Error bars are calculated according to error propagation. Based on average values observed over many measurements, an absolute error of $\Delta\bar{n}$ = 0.3 and a relative error of $\Delta\bar{F}$ = 5 % are assumed.

At first, the measurements under design conditions shall be considered here. Stepping through the experimental protocol given in section 5.4.2, the liFCS MB-curves are determined. In this respect, the overall measurement time is desired to be minimal, but still long enough to obtain a sufficiently accurate value for ϕ_{fl}, which means that the liFCS approach should be at

least as strong as other commonly employed bulk methods with an average error of ≈ 10 % [46–48]. Here, the measurement time per applied excitation power is fixed to 1.5 min and the MB is determined for three to four different power values lower than ≈ 100 a.u., using *cw*-excitation. The concentration of each solution is adjusted to yield an average of five to ten fluorophores in the effective volume. Exemplarily, the obtained liFCS MB-curves for the three cyan/green dyes (FLUO, AL488, AT488) are shown in figure 5.18. The corresponding absorption, fluorescence and transmission spectra for the cyan/green dyes are shown in Appendix A A.2,A.3,A.4. The resulting parameters required for the evaluation of equation 5.14 and the obtained values for ϕ_{fl} are summarized in table 5.4. All determined ϕ_{fl}-values coincide with the nominal values stated by the manufacturer. The relative error lies below/around 10 % for all dyes, which is considered to be sufficient here. However, the relatively large error is mainly a consequence of the uncertainty of the slope of the MB-curves and can be minimized by using more different excitation power points and measuring each MB-value several times to obtain more precise average and standard deviation values. However, for both spectral ranges and under design-conditions the liFCS-approach has been validated within the scope of the desired accuracy.

Sample	**m** [cpm/sau]	$\epsilon_{\lambda_{exc}}$ [$M^{-1}cm^{-1}$]	**g**	$\phi_{fl,nom}$	ϕ_{fl}
FLUO	89.4 ± 5.2	73797 ± 738	0.106	0.92 ± 0.04	-
AL488	82.0 ± 4.7	66233 ± 662	0.107	0.92 ± 0.04	0.93 ± 0.08
AT488	58.5 ± 2.3	55908 ± 559	0.109	0.80 ± 0.03	0.77 ± 0.05
AT655	40.8 ± 1.3	88452 ± 885	0.118	0.30 ± 0.01	-
AL647	81.0 ± 8.6	175424 ± 1754	0.121	0.33 ± 0.01	0.29 ± 0.03

Table 5.4: Parameters needed for the liFCS approach along with the obtained quantum yield values. $\phi_{fl,nom}$ denotes the nominal quantum yield. Within the error limits, experimental ϕ_{fl}-values coincide with $\phi_{fl,nom}$-values. The relative error lies below 10 % for AL488 and AT488 and around 10 % for AL647.

As a next step, the results obtained under non-design conditions will be evaluated by comparing the liFCS quantum yields of AT488 and AT655 in glycerol solution to the ones obtained with the standard method. For the liFCS approach, the same measurement time and sample concentration as mentioned before are used. The obtained results are shown in figure 5.19. Within the error limits, the quantum yields determined by liFCS and the standard approach coincide, validating that the liFCS is also working reliably in solutions of refractive indices higher than the one of water.

5.4.5 Comparison of liFCS approach with lifetime-based method

As given by equation 4.7, the fluorescence quantum yield of a fluorophore can be defined as the ratio of its fluorescence lifetime to its natural lifetime. According to the rule of Strickler-and-Berg, the natural lifetime can be estimated through [145]:

$$\tau_n = 3.4722 \cdot 10^{-10} \cdot \frac{1}{n^2} \cdot \langle \bar{\nu}^{-3} \rangle \left[\int \frac{\epsilon(\bar{\nu}) d\bar{\nu}}{\bar{\nu}} \right]^{-1} \tag{5.20}$$

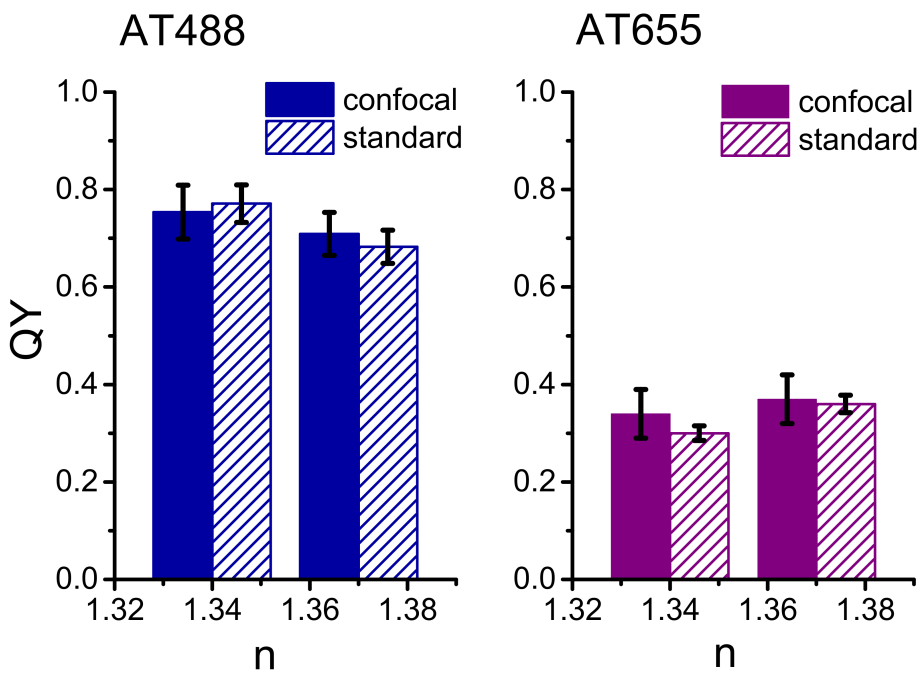

Figure 5.19: Quantum yield values of AT488 and AT655 in glycerol solutions obtained with liFCS and standard approach. Within the error limits the obtained results coincide, validating the applicability of the liFCS approach under non-design conditions. AL488 and AL647 in Glycerol solutions of same refractive index served as reference samples.

$\bar{\nu}$ is the wavenumber and $\epsilon(\bar{\nu})$ the corresponding absorption spectrum. It should be mentioned that the derivation of equation 5.20 is based on several assumptions, among others the absolute rigidity of the ground and excited state of the fluorescent molecule and the absence of interaction with the solvent. Clearly, in many real systems these assumptions are not met and therefore the predicted τ_n can differ significantly from the measured one [146, 147]. However, assuming that the natural lifetimes of reference and sample coincide, the sample quantum yield can be determined according to:

$$\phi_{fl,s} = \frac{\tau_{fl,s}}{\tau_{fl,r}} \cdot \phi_{fl,r} \tag{5.21}$$

Again, subscript s denotes the sample and subscript r the reference. With another look at equation 5.20 it gets clear that the natural lifetime of sample and reference can only be similar when the spectral properties of the two are alike. Therefore, in most cases the same fluorophore is used as reference and sample, in the first case freely diffusing in some solvent, in the latter case attached to some bio-molecule of interest.

Although the quantum yield determination based on the fluorescence lifetime is very convenient, it is tainted with several disadvantages. On the one hand, it is not sensitive to the so-called static quenching of the fluorophore. During this process, the fluorophore forms a non-fluorescent ground-state complex with the quencher. A well-known dynamic and static quencher of the fluorescence of AL488 is the amino acid tryptophane (TRP) [148]. To demonstrate that the liFCS approach is sensitive to static quenching whereas the lifetime method is not, specific amounts of TRP are added to PBS solutions of AL488 and the corresponding quantum yields are determined.

The results are depicted in figure 5.20. As discussed, the fluorescence quan-

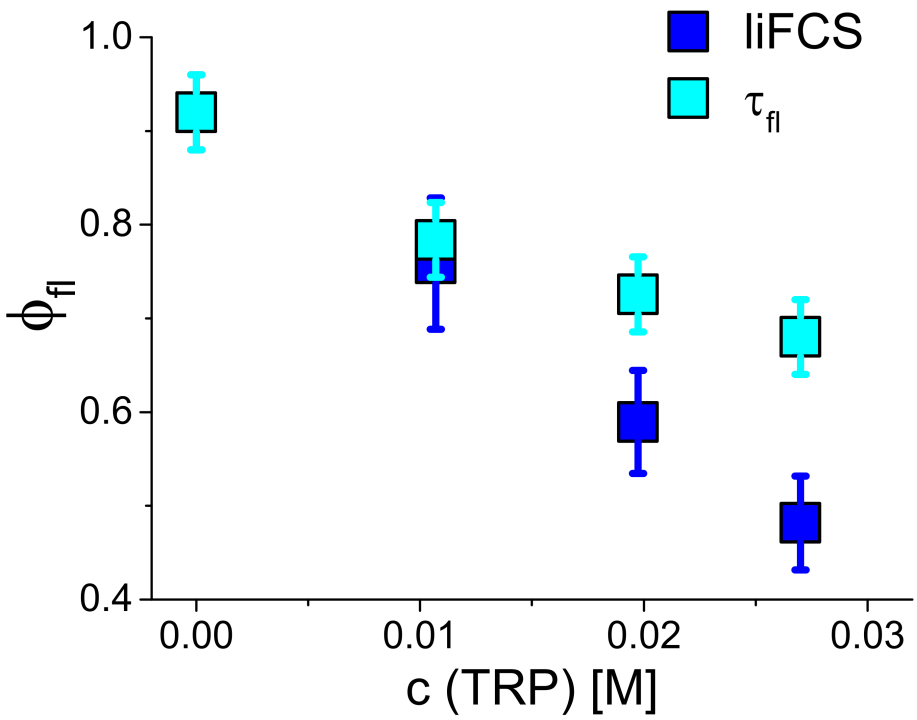

Figure 5.20: AL488 quantum yields obtained by liFCS (dark blue squares) and lifetime method (cyan squares) as a function of tryptophane (TRP)-concentration .

tum yields determined by the lifetime method and the liFCS approach do not coincide as a result of the static quenching detected by the liFCS approach but not by the lifetime method. However, combining both approaches, information about the underlying quenching constants can be obtained. Plotting the ratio of the lifetime of the unquenched dye to the lifetime under quenching conditions against the applied quencher concentration, a linear curve is obtained with a slope equal to the dynamic Stern-Volmer constant K_D, as given by [43]:

$$\frac{\tau_{fl,0}}{\tau_{fl}} = 1 + K_D \cdot [TRP] \tag{5.22}$$

The obtained results are shown in figure 5.21 (a). The determined dynamic Stern-Volmer constant is in perfect agreement with the literature value of K_D= 14.2 M^{-1} [149]. On the other hand, the ratio of the liFCS quantum yield of the un-quenched dye to the liFCS quantum yield of the quenched dye is described by [43]:

$$\frac{\phi_{fl,0}}{\phi_{fl}} = (1 + K_D \cdot [TRP]) \cdot (1 + K_S \cdot [TRP]) \tag{5.23}$$

Inserting equation 5.22 into equation 5.23, the following linear relationship is obtained:

$$\frac{\phi_{fl,0}}{\phi_{fl}} \cdot \frac{\tau_{fl}}{\tau_{fl,0}} = 1 + K_S \cdot [TRP]) \tag{5.24}$$

Therefore, plotting the ratio of the two relations as a function of TRP according to equation 5.24, again, the slope of the linear curve equals the Stern-Volmer constant, but now quantifying the process of static quenching.

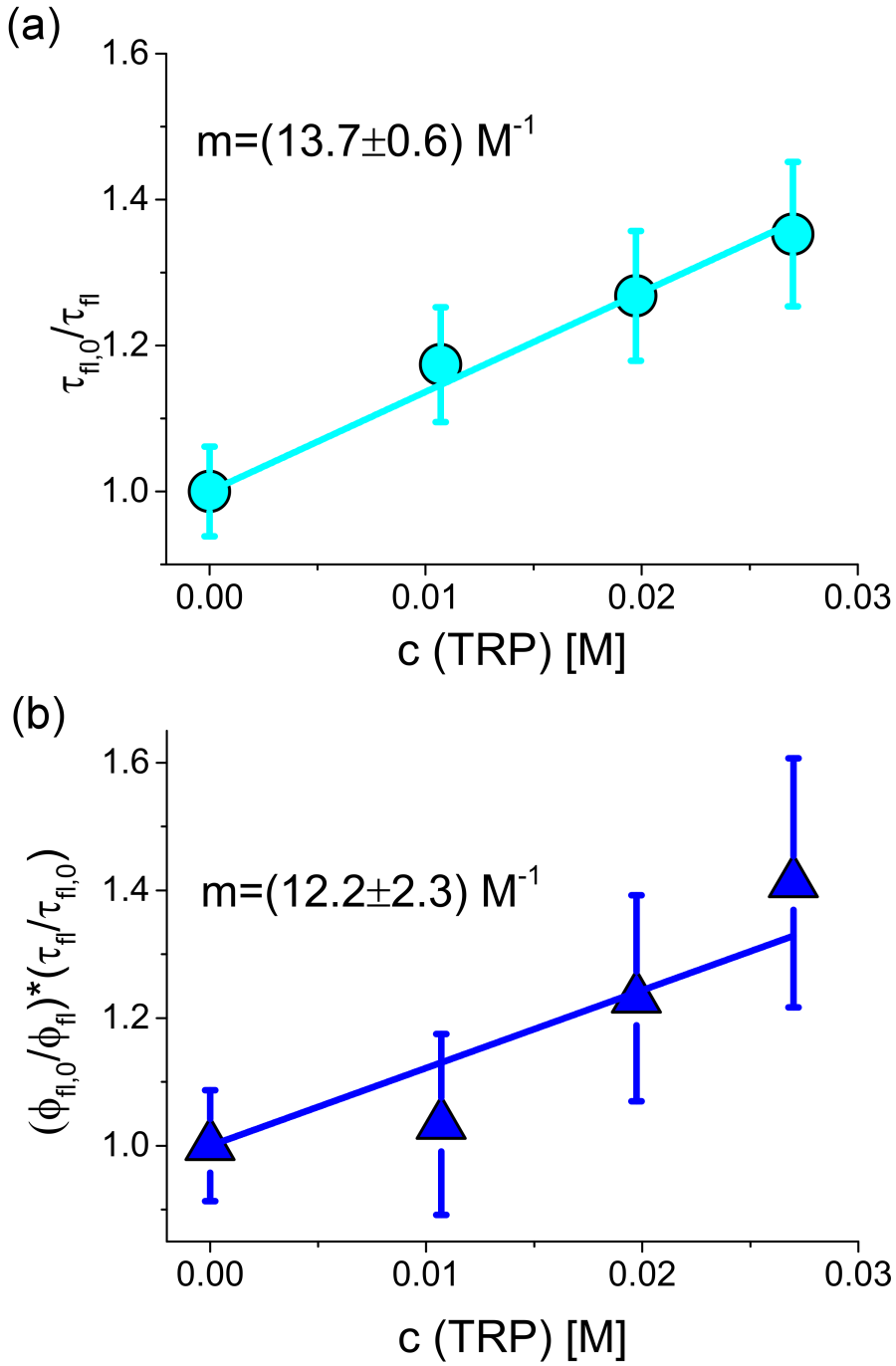

Figure 5.21: (a) Ratio of lifetime of AL488 in the absence of to its lifetime in the presence of TRP as a function of TRP-concentration. The dynamic Stern-Volmer constant equals the slope of the curve. (b) Ratio of the liFCS quantum yields of un-quenched and quenched AL488 divided by the lifetime ratio used to determine the dynamic quenching constant as a function of the TRP concentration. The static Stern-Volmer constant equals the slope of the curve.

The obtained result is shown in figure 5.21 (b). In this case, taking into account the larger error limits, the determined static Stern-Volmer constant does not perfectly coincide with the literature value of K_S=14.9 M^{-1} but lies in close proximity. Hence, although the fluorescence lifetime is not sensitive

to static quenching and therefore an inappropriate indicator of the fluorescence quantum yield of a sample, it is a valuable tool to obtain information about the local environment of the fluorophore. In combination with the liFCS approach, the quenching mechanisms influencing a given system can be evaluated in detail.

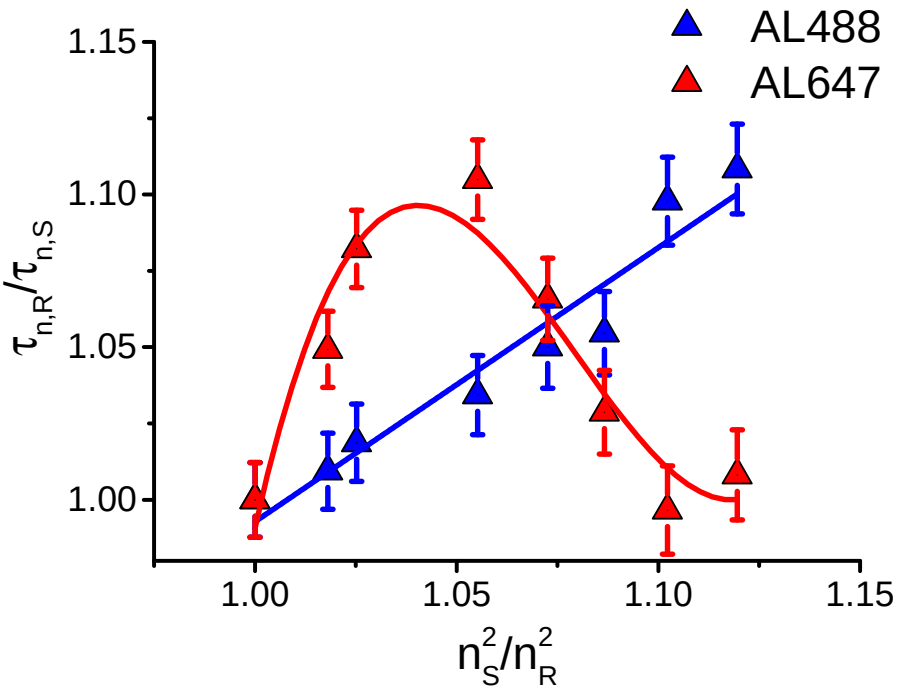

Figure 5.22: Ratio of the natural lifetime of AL488 and AL647 in water to the natural lifetimes in glycerol solutions plotted as a function of the ratio of the refractive indices squared.

Besides its intrinsic insensitivity to static quenching, the use of the fluorescence lifetime to determine quantum yields bears other risks. As already mentioned before, in general the same fluorophore is used as reference and sample of interest to fulfill the criterion of matching natural lifetimes. However, the natural lifetime depends on the local environment of the fluorophore (as already clear from its connection to the spectra), meaning that it can drastically change in response to different solvent properties or interactions with macro-molecular surfaces. This is also shown in figure 5.22, where the ratio of the natural lifetime of AL488 and AL647 in water to their natural lifetimes in glycerol solutions is plotted as a function of the square of the ratio of the refractive index of glycerol solutions to water. Obviously, the two fluorophores react completely different to the new environment. While the natural lifetime of AL488 behaves somewhat predictable, namely in accordance with the previously introduced rule of Strickler-Berg 5.20 and therefore showing a linear dependency on the squared refractive index ratio, the ratio of the natural lifetimes of AL647 shows a close to parabolic shape. The latter is probably a result of the concurrent influences of solvent viscosity and refractive index on the lifetime of AL647. However, even in this simple example using a fluorophore in water as the reference and the same fluorophore in a different solvent as the sample of interest, an *a priori* prediction of the behavior of the natural lifetime appears difficult. Hence,

simply stating that it most likely stays constant under changed environmental conditions seems to be precarious.

5.5 smFRET measurements in additive-enriched solutions

5.5.1 Physical properties of employed solvents

In this section, focus is set on the impact of the solvent environment on the characteristics of the fluorescent markers and concurrently on the obtained smFRET efficiencies. To begin with, the most important physical properties of the solvents employed in the following are summarized in table 5.5. Especially the dielectric constant, the ionic strength and the Debye length are of importance for the sections about the estimation of electrostatic donor-acceptor interactions and their impact on the obtained inter-dye distance.

Solvent	n	η [mPas]	ϵ_r	I [M]	κ^{-1} Å
DNA buffer	1.33	1.06	≈ 80	0.15	7.9
+ 1 M NaCl	1.34	1.13	≈ 65	1.15	2.6
+ 4 M GdnHCl	1.40	1.34	≈ 40	4.15	1.1
+ 50 wt.% Glycerol	1.40	6.33	≈ 65	0.15	7.1
PGK buffer	1.33	1.06	≈ 70	0.08	10.1
+ 1 M GdnHCl	1.35	1.11	≈ 65	1.08	2.6
+ 1.5 M GdnHCl	1.36	1.13	≈ 45	1.58	1.8
+ 4 M GdnHCl	1.40	1.34	≈ 40	4.08	1.1
+ 6 M GdnHCl	1.44	1.69	-	6.08	-

Table 5.5: Properties of solvents used in this section. Here, n is the refractive index and η the dynamic viscosity of the solvent. The relative permittivity is denoted as ϵ_r and the ionic strength as I. Lastly, κ^{-1} is the Debye length. Refractive indices are measured and used to estimate the corresponding viscosity [61, 68]. The relative permittivity values are taken from literature sources [60, 65]. The ionic strength and Debye-length are calculated according to references [60, 150].

5.5.2 FRET studies of rigid DNA-oligonucleotides

Sample introduction

In this section, double-stranded, double-labeled DNA (dsDNA) oligonucleotides with donor and acceptor linkers attached at a distance of 10 bp or 17 bp are employed as test specimen. Here, AL488 is used as donor and AL647 is used as acceptor fluorophore. As solvents, DNA buffer and buffer with either 1 M NaCl, 4M GdnHCl, or 50 wt. Glycerol added are used. The 3D structure of the structurally rigid (length $\approx$ 16 nm, persistence length $\approx$ 50 nm) dsDNA constructs in DNA buffer and the corresponding so-called accessible volume (AV) clouds of the donor and acceptor fluorophore are shown in figure 5.23. AV calculations, based on simple geometrical search algorithms, are a common approach to predict the sterically accessible space of a fluorescent marker attached to a specific macro-molecule [29]. As compared to the linker attachment position distances, it has been shown that inter-dye distances predicted by AV-calculations are in much better agreement with the experimentally determined smFRET inter-dye distances, in particular for double-labeled DNA oligonucleotides [151]. A more detailed description of the AV calculations will be given in the context of the theoretical assessment

of potential electrostatic interactions of the fluorescent markers, see section 5.5.3.

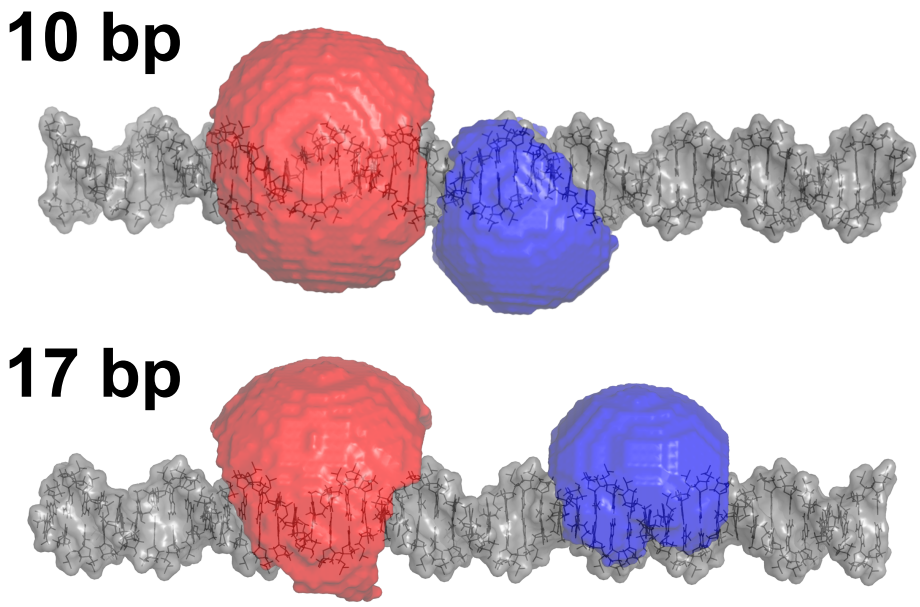

Figure 5.23: 3D structures of dsDNA oligonucleotides. 10 bp and 17 bp are the distances in between linker attachment points. In red, the sterically accessible volume (AV) of the acceptor is shown. The AV of the donor is depicted in blue. AV-clouds are calculated with the FRET positioning and screening (FPS) software [28]. The 3D structures of the constructs are generated using 3D-DART [152]. Molecular visualization is carried out via Pymol.

Fluorescent markers: directly solvent-induced changes only

As a first step, the fluorescence emission and absorption spectra of the labeled DNA oligonucleotides in the different solvents are compared. Although the DNA sample shows a pronounced bathochromic shift going from pure buffer to GdnHCl and Glycerol (see figure A.5 in the Appendix), the same shift is observed for the sole fluorescent markers in the same solvents. This indicates that the spectra simply change in response to the varied solvent conditions and not in response to a structural change in the local fluorophore environment. The coincidence of the emission spectra of attached and unattached AL488 and AL647 is depicted in figure 5.24 for the case of Glycerol as additive.

Assessment of the the orientation factor κ^2

To calculate the Förster radius, the value of the orientation factor κ^2 has to be evaluated. Therefore, TRA measurements are performed to determine the rotational mobility of the linker-dye unit. All anisotropy decays were fitted with the wobbling-in-a-cone model 4.60. The obtained results are given in table 5.6. Under the assumption that donor and acceptor reorientate randomly on a time-scale much faster than the one of FRET, the so-called dynamic averaging regime can be assumed [153]. Referring to TRA measurements, this means that the rotational correlation times have to be

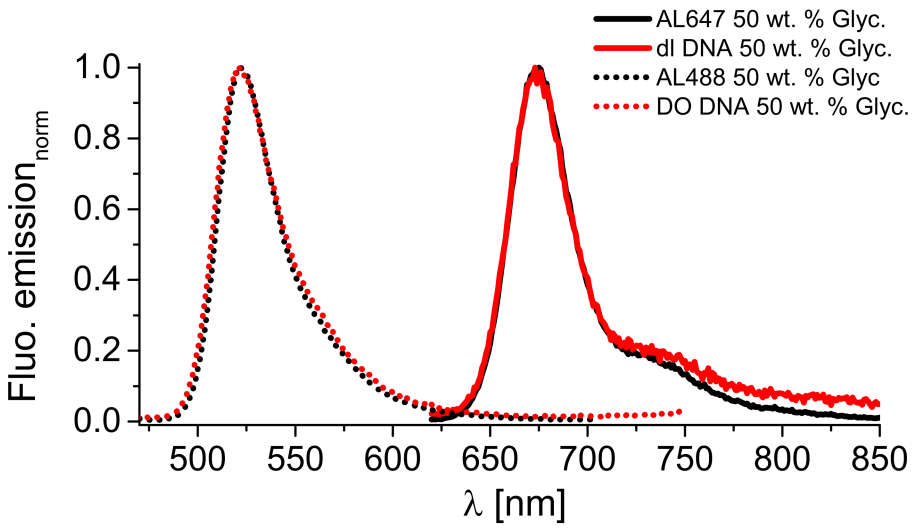

Figure 5.24: Peak-normalized fluorescence emission spectra of unattached and 10 bp DNA-bound AL488 and AL647 in DNA buffer with 50 wt. % Glycerol added.

10/17 bp DNA-construct	AL488		AL647	
Solvent	θ_r [ns]	θ_{max} [°]	θ_r [ns]	θ_{max} [°]
DNA buffer	0.6 ± 0.1	47 ± 1	0.9 ± 0.1	50 ± 1
+ 1 M NaCl	0.7 ± 0.1	55 ± 1	1.0 ± 0.1	51 ± 1
+ 4 M GdnHCl	1.1 ±0.1	48 ± 1	1.5 ± 0.1	58 ± 1
+ 50 wt. % Glycerol	2.6/3.1 ±0.3	43/51 ± 2	5.1 ± 0.4	52 ±1

Table 5.6: Rotational correlation (θ_r) times and semi-cone angle (θ_{max}) for dsDNA oligonucleotides obtained by TRA measurements. Values before slash correspond to 10 bp sample, values after slash to 17 bp sample. If only one value is given, both values coincide.

smaller than the inverse energy transfer rate. For pure buffer, 1 M NaCl and 4 M GdnHCl this condition is fulfilled. Then, although the orientation distributions of donor and acceptor are not strictly isotropic here, κ^2 can be replaced by its average value ($\langle\kappa^2\rangle$) of two-thirds [151]. For the glycerol solution, the rotational correlation times are close to the time-scale of FRET, which makes an estimation of κ^2 more difficult. However, for a FRET-pair of ATTO-dyes dissolved in an even higher concentrated glycerol solution, MD-simulations showed that it is also appropriate to use $\langle\kappa^2\rangle$ =2/3 [67]. Hence, in the following, all Förster radii are calculated using this value. It is worth to mention that, with the exception of the donor in glycerol, the relevant anisotropy parameters do not change significantly going from the 10 bp to the 17 bp construct. Consequently, κ^2 should be similar in both cases, enabling to monitor relative distance changes correctly even if κ^2 is estimated erroneously.

Determination of FRET calibration parameters

The quantum yields of the labeled DNA oligonucleotides in each of the solvents are determined with the help of the liFCS approach. Here, value and error limit correspond to the mean and the standard deviation of three

different measurement series. The obtained results are given in table 5.7, together with the respective transmission/detection efficiency parameter g.

10/17 bp DNA-construct	AL488		AL647	
Solvent	ϕ_{fl}	g	ϕ_{fl}	g
DNA buffer	0.85 ± 0.04	0.10	0.35 ± 0.02	0.11
+ 1 M NaCl	0.85 ± 0.04	0.10	0.43 ± 0.02	0.11
+ 4 M GdnHCl	0.79 ±0.04	0.09	0.62 ± 0.03	0.10
+ 50 wt. % Glycerol	0.94 ±0.05	0.09	0.53 ± 0.03	0.09

Table 5.7: Quantum yields and transmission/detection efficiency parameters for the double-stranded, double-labeled DNA oligonucleotides in all solvents.

Single-molecule measurements: optimal excitation intensity

To find the optimal excitation intensity for the sample at hand, signal-to-background (SBR) and corresponding signal-to-noise (SNR) ratios are determined (see section 4.2.2 for details). The obtained results for the donor of the 10 bp dsDNA are shown in figure 5.25. Here, pulsed excitation with a frequency of 20 MHz is used. Obviously, the MB increases with increasing

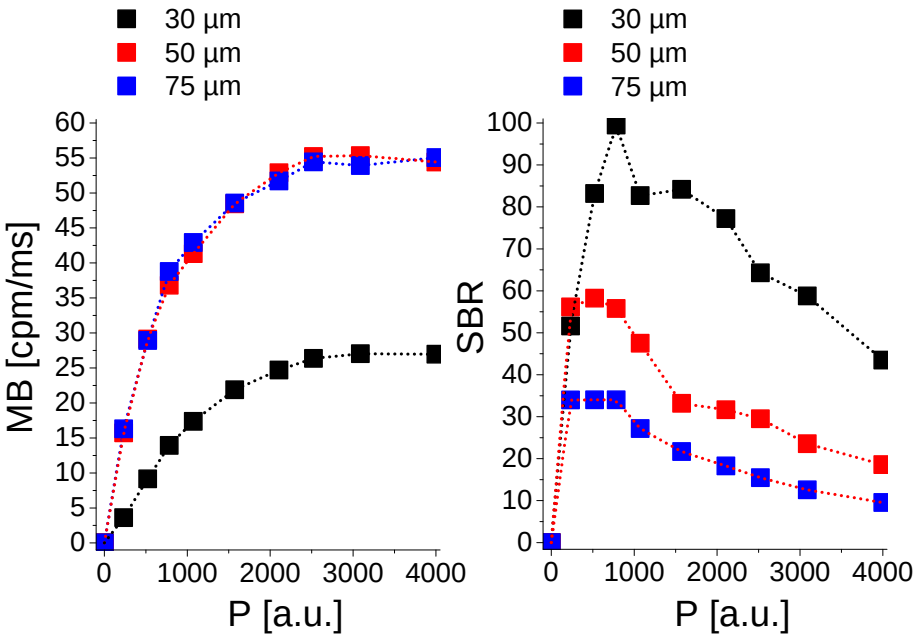

Figure 5.25: Left: Molecular brightness of donor of the 10 bp dsDNA construct for varying pinhole sizes as a function of excitation power. The highest MB-values are obtained for pinholes of 50 and 75 µm. Right: Corresponding signal-to-background ratios. In the regime from 200 a.u. to 700 a.u., the SBR are maximal for all pinhole sizes.

excitation power until optical saturation, the occupancy of triplet states and bleaching effects counteract this rise [99]. The maximal molecular brightness is obtained by employing the 50 or 75 µm pinholes. The employment of the smaller 30 µm pinhole obviously blocks too much of the signal to allow high MB values. On the contrary, the obtained SBR values decrease with increasing pinhole size, as more scatterers contribute to the overall signal.

With respect to the applied laser power, the highest SBR values lie in the range between 200 a.u. and 700 a.u. for all pinhole sizes.

Although SBR values are useful to some extent, the more important quantities are the corresponding SNR values. These are shown in figure 5.26 for the three different pinhole sizes and increasing laser powers. Referring

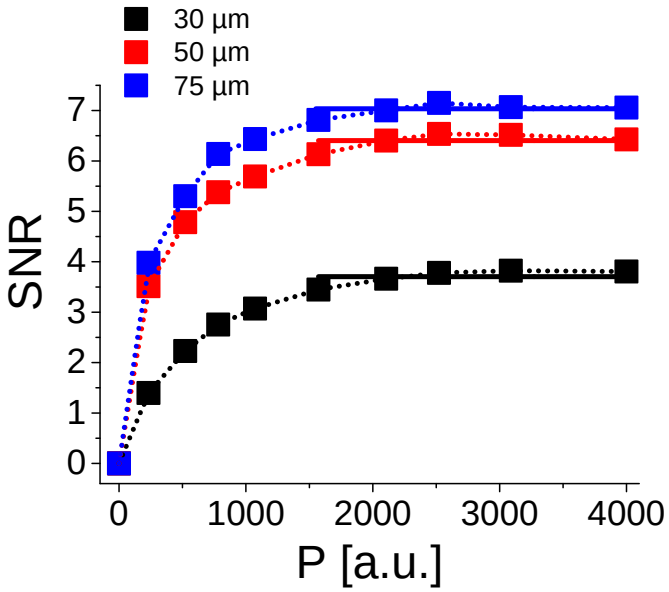

Figure 5.26: Signal-to-noise ratios (SNR) of donor of the 10 bp dsDNA construct for varying pinhole sizes as a function of excitation power. Duration Δt is adjusted to MDF volumes and estimated as $\approx$ 1 ms for the largest pinhole, $\approx$ 0.8 ms for the 50 μm pinhole and $\approx$ 0.6 ms for the smallest pinhole. The best SNR is achieved with the 75 µm pinhole, the worst with the 30 µm pinhole. Applying a laser power of 1500 a.u., the maximal SNR is reached in all three cases.

to figure 5.26, the employment of a 75 µm pinhole in combination with a laser power of 1500 a.u. provides the optimal SNR and therefore the optimal measurement conditions for the sample at hand. Cranking up the laser further does not improve the SNR and additionally enhances the probability of photo-destruction. Especially considering single-molecule FRET measurements, a dependence of the amount of acceptor bleaching on the intensity of the donor-excitation light has been reported. Although the light used for donor-excitation does not significantly excite the ground state of the acceptor directly, its interaction with the FRET-induced excited state of the acceptor presumably opens alternative bleaching pathways [133].

smFRET measurements

Single-molecule measurements are performed as explained in detail in section 4.2.3. Employing PIE, the donor is excited applying a laser power of 1500 a.u., whereas the acceptor is excited applying a laser power of 400 a.u.. The time-window sizes for the burst selection are adjusted to the dwell-times in the effective volume obtained by FCS: around 1 ms for the DNA constructs in buffer and in buffer with salt and denaturant, and around 2 ms in buffer with glycerol added. Only FRET-bursts with more than 80 (buffer, salt, denaturant) or 100 (Glycerol) photons are used to calculate FRET efficiencies. For both DNA constructs and in all solvents the amount of double-labeled

DNA roughly estimated by coincidence analysis lies around 10 % only, as the ratio of donor to acceptor single strands put together for hybridization was not optimal. In the optimal case, a double-labeled fraction up to 30 % can be expected.

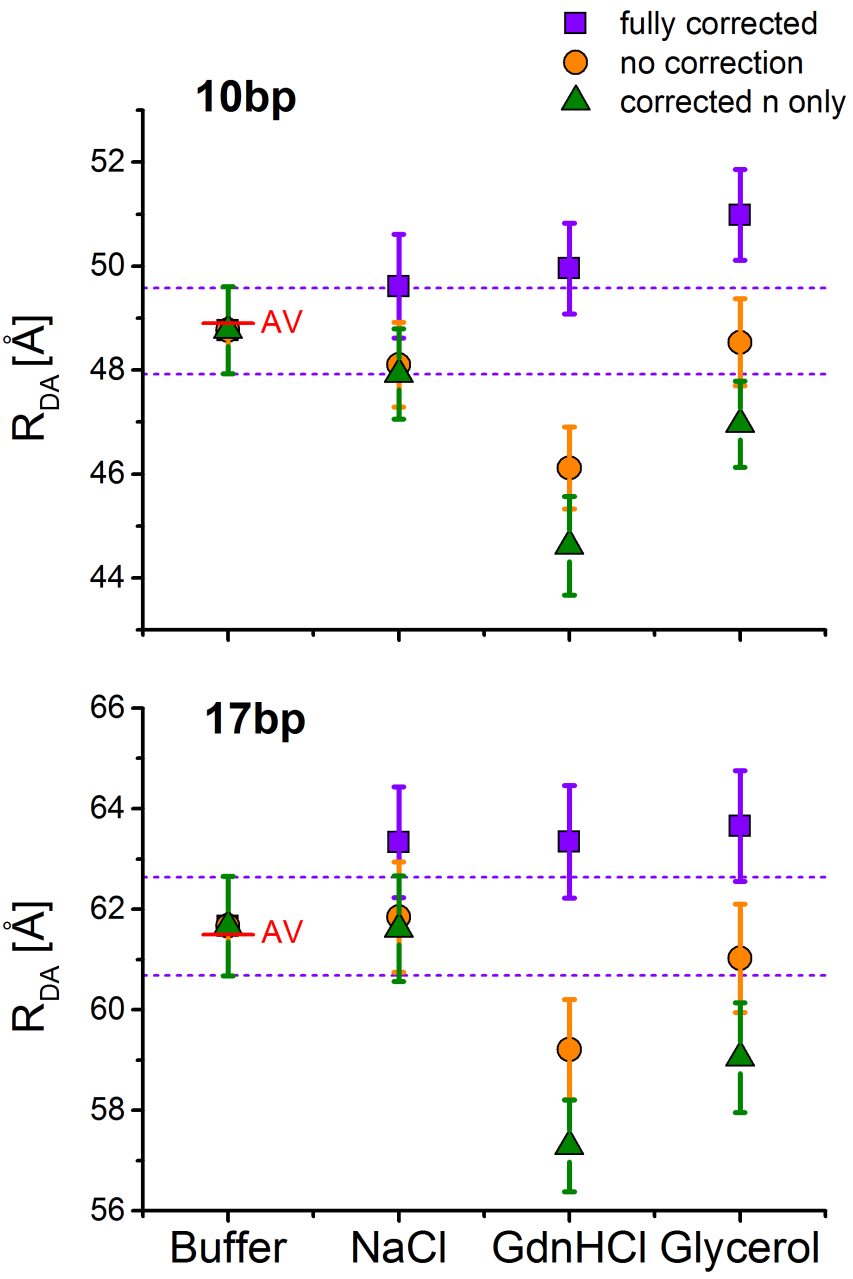

Figure 5.27: Mean inter-dye distances R_{DA} of the 10 bp and 17 bp dsDNA constructs in different solvents [c(NaCl) = 1 M, c(GdnHCl) = 4 M, 50 wt.% glycerol]. In violet, fully corrected distances are shown. In green, R_{DA} calculated using uncorrected $\bar{E}$ and R_0 are depicted. In green, distances determined using uncorrected $\bar{E}$ and R_0 values, the latter corrected for solvent refractive indices, are shown. Error-bars are determined using the highest and lowest values of $\phi_{fl,A}$ and $\phi_{fl,D}$ in accord with the error-limits, calculating the corresponding E distributions, fitting them with a Gaussian distribution and calculating the upper and lower limit of R_{DA} using equation 4.23. The violet dashed lines represent the error limits for the measurements in buffer. The inter-dye distance obtained by AV-calculations is depicted by the short red line.

In Figure 5.28, the FRET efficiency histograms taking into account all solvent induced spectral and QY changes (corrected) are compared to the ones calculated with the parameters measured in DNA buffer (uncorrected). All histograms are fitted with a Gaussian distribution to determine the mean FRET efficiency. The deviation between corrected and uncorrected $\bar{E}$ values spans from 10 % to remarkable 35 % for 4 M GdnHCl (results in table B.2). Additionally, almost all uncorrected histograms show a misleading apparent increase of the transfer efficiency.

As a next step, the corresponding inter-dye distances (R_{DA}) are determined according to equation 4.36, which means that the Förster radius has to be known. As discussed in section 5.5.2, it is calculated with the orientation factor κ^2 set to its mean value of two-thirds in all cases. Then, three inter-dye distances calculated in different ways are considered: (i) the fully correctedR$_{DA}$ for different solvent compositions, taking into account all solvent-induced changes; (ii) R_{DA} calculated using the uncorrected FRET-efficiencies as well as the Förster radius measured in buffer; (iii) R_{DA} calculated from the uncorrected transfer efficiencies and using the Förster radius obtained with the overlap integral measured in buffer but taking into account the actual refractive index of the solvent. The obtained results are shown in figure 5.27, along with the inter-dye distance in pure buffer provided by AV-calculations. Additionally, Förster radii and R_{DA} values are summarized in tables B.3 and B.4.

As compared to pure aqueous buffer, the corrected values for all other environmental conditions exhibit marginally larger interdye distances. However, especially for the solvents containing large amounts of additives, we do observe significant differences between corrected and uncorrected inter-dye distances as high as 0.4 nm. Additionally, the uncorrected R_{DA} values lead to a misinterpretation of the experimental results, as the oligonucleotide constructs appear to become more compact instead of more expanded in the GdnHCl and glycerol solutions.

Interestingly, including the refractive index n of the solvent and concurrently neglecting any further corrections can lead to even stronger deviations from the fully corrected inter-dye distances than applying no corrections at all. Since the impact of the individual corrections can typically not be predicted *a priori*, the application of all corrections is mandatory in order to obtain reliable R_{DA} values.

5.5.3 Inter-dye distance calculations: electrostatic interactions

As AL488 and AL647 both are negatively charged at neutral pH (-2e and -3e, with e being the elementary charge), they interact electrostatically, with the extent of interaction depending on their distance and the properties of the solvent. Going from pure aqueous buffer to the other solvent environments, the dielectric constant as well as the Debye length decrease (see table 5.5 for details). Therefore, in this section focus is set on the impact of these two parameters on the electrostatic donor-acceptor repulsion and the resulting inter-dye distances obtained by FRET measurements. To be able to give quantitative estimations, the standard AV calculation is expanded.

As mentioned before, AV clouds are the product of a geometric search algorithm finding all positions within the linker length from the attachment point that do not cause steric clashes with the surface of the biomolecule [28].

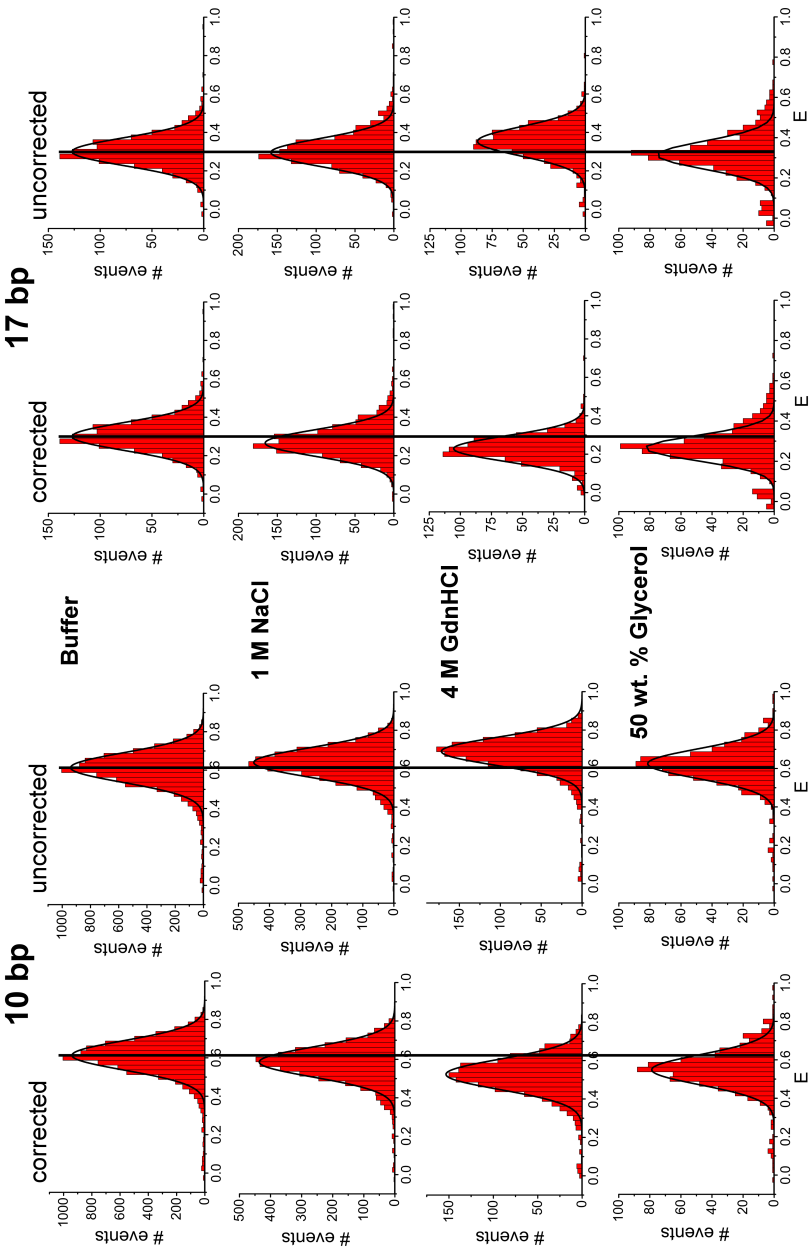

Figure 5.28: FRET-efficiency histograms of the two constructs in different solvents. The corrected histograms are calculated taking into account spectral and QY changes of the FRET pair, whereas the uncorrected histograms are calculated with the parameters determined for buffer. Black solid lines depict the Gaussian distributions best fitting the data. Deviations of up to 35 % are found along with a misleading apparent increase of $\bar{E}$ for the uncorrected data.

Besides the linker dimensions (width and height), obviously also the spatial extent of the dye has to be taken into account, which, for convenience, is modeled as a sphere. Having found all accessible positions for a specific dye-linker unit parameterization, the average inter-dye distance is found according to:

$$\bar{R}_{DA} = \int_{AV,A} \int_{AV,D} d\vec{r}_A d\vec{r}_D P(\vec{r}_A, \vec{r}_D) |\vec{r}_A - \vec{r}_D| \tag{5.25}$$

Here, $\vec{r}_A$ and $\vec{r}_D$ denote the position vectors of acceptor and donor and P($\vec{r}_A$, $\vec{r}_D$) describes the probability to find a specific configuration of $\vec{r}_A$ and $\vec{r}_D$. In the standard AV approach, each configuration is equally likely, hence P($\vec{r}_A$, $\vec{r}_D$) is a constant. The fact that the integration is over the accessible volume clouds of the acceptor and donor is indicated by AV,A and AV,D. To improve the accuracy of the inter-dye distance calculation, three different dye radii can be selected and the corresponding AV cloud for each radius can be determined. The inter-dye distance is then obtained by averaging over all positions available in all clouds. The radii, widths and lengths used in this work to describe the AL488/AL647-linker constructs are given in table 5.8 (for depiction of dye-linker structures and corresponding dye radii, linker width and length, see figure A.6): Now, in the expanded AV calculation,

Sample	Linker length [Å]	Linker width [Å]	Radius 1 [Å]	Radius 2 [Å]	Radius 3 [Å]
AL488	20	3	5	4.5	1.5
AL647	24	3	10.5	8.8	8

Table 5.8: Parameters used to describe the linker-fluorophore unit attached to the dsDNA constructs.

besides steric clashes the effect of the total charge of the dyes, including the screening of their mutual repulsion due to the solvent environment, is taken into account. In the course of this, each dye is considered as a solid colloid with a homogeneously distributed total charge. In this case, the energy between two charged colloids of radii R_A and R_D, located at $\vec{r}_D$ and $\vec{r}_A$, is given by [154, 155]:

$$U(r) = Z_A Z_D \frac{e^2}{4\pi\epsilon_0\epsilon_r} \frac{\exp(-\kappa(r - R_A - R_D))}{(1 + \kappa R_A)(1 + \kappa R_D)r} \tag{5.26}$$

if the distance r=|$\vec{r}_D$- $\vec{r}_A$| is larger than the sum of the two radii. Otherwise, U(r) equals infinity. Here, κ is the inverse of the Debye length, ϵ_0 is the vacuum permittivity and Z_A/Z_D is the charge of the acceptor/donor colloid. Then, the probability of a configuration with donor and acceptor located at $\vec{r}_D$ and $\vec{r}_A$ is given by [156]:

$$P(\vec{r}_A, \vec{r}_D) = C \exp\left(-\left(\frac{1}{k_B T}\right) U(\vec{r}_A - \vec{r}_D)\right) \tag{5.27}$$

The parameter C is a normalization factor, k_B is the Boltzmann constant and T is the absolute temperature.

The obtained inter-dye distances for the 10 bp dsDNA construct calculated with the help of the expanded AV approach are given in table 5.9.

Solvent	$\bar{R}_{DA}$ (AV,expanded) [$\AA$]	$\bar{R}_{DA}$ (AV,standard) [$\AA$]
DNA buffer	49	48.7
+ 1 M NaCl	48.7	-
+ 4 M GdnHCl	48.7	-
+ 50 wt. % Glycerol	48.9	-

Table 5.9: Average inter-dye distance of AL488 and AL647 attached to the 10 bp dsDNA construct calculated with the help of the AV-cloud of each dye and with (expanded) and without (standard) taking into account electrostatic dye-dye repulsions .

The resulting average inter-dye distances coincide for all considered solvent conditions, hence, being quite insensitive to electrostatic dye-dye repulsions. This is accordance with the experimental findings from the smFRET measurements of the dsDNA constructs discussed in the previous section 5.5.2. As shown in figure 5.27, for both distance regimes the increase of the inter-dye distance lies between 1 and 2 $\AA$ going from pure aqueous buffer to more complex solvent conditions. Comparing the additive-enriched solutions only, the resulting inter distances even coincide within their error-limits. Under the assumption that there is no antagonistic concurrent conformational change of the dsDNA constructs, the impact of electrostatic interactions on the inter-dye distance is therefore small. Additionally, the inter-dye distances increase in a similar manner for the 10 bp and 17 bp dsDNA construct going from buffer to the additive-enriched solutions, which should also not be the case if strongly distance dependent electrostatic interactions would play a role.

To assess the impact of electrostatic interactions over a broader distance interval, the inter-dye distance between a donor and an acceptor tethered by a linker to two fixed points in free space (distance d_c) are calculated. Only limited by the linker length, the corresponding AV clouds are spherical. Then, two different electrostatic scenarios are considered: (i) an isotropic scenario,in which the two linkers are flexible and thereby allow the dye to explore the complete spherical volume defined by a radius corresponding to the linker length. As before, the dyes are described by homogeneously charged colloids. (ii) an anisotropic scenario, in which the dye AV is described by a complete sphere defined by the linker length, but now the interaction energy corresponds to the most unfavorable case. This means that the whole charge is now concentrated in one point, situated at the intersection of the surface of each dye and the vector that joins their positions. In this case, which represents an overestimation of the electrostatic repulsion, the interaction energy is given by [154, 155]:

$$U_{ani}(r) = Z_A Z_D \frac{e^2}{4\pi\epsilon_0\epsilon_r} \frac{\exp(-\kappa(r - R_A - R_D))}{r - R_A - R_D} \tag{5.28}$$

if the distance $r=|\vec{r}_D - \vec{r}_A|$ is larger than the sum of the two radii. Otherwise, $U_{ani}(r)$ equals infinity. For visualization, both scenarios are depicted in figure 5.29. With the help of equation 5.25, the expected average inter-dye distances for both scenarios can be calculated. The results are depicted in figure 5.30 (a). As black dotted line, inter-dye distances calculated without

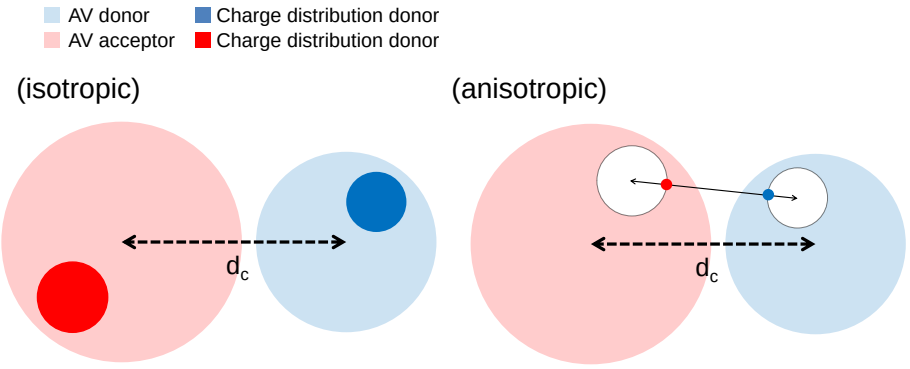

Figure 5.29: Schematic depiction of two different scenarios of electrostatic interaction. Donor and acceptor are tethered via a linker to two points in free space. These attachment points are separated by a distance d_c. In both scenarios, the linker is considered to be flexible, thereby giving each dye access to each position in a spherical volume (AV). Clearly, this spherical volume has a radius corresponding to the linker length. Donor and acceptor dye are visualized as spheres (depiction not to scale). In the isotropic case, the overall charge is assumed to be homogeneously distributed over the spherical volume of donor and acceptor. In the anisotropic case, the charge is assumed to be focused in one point. This point is chosen to be the intersection of the surface of the spheres with the vector connecting the positions of donor and acceptor.

any restrictions are given. Interestingly, these do not coincide with the centroid distances (solid black line) but show a constant positive offset. This mismatch is mainly due to the geometry of the clouds (see equation 5.25). Remarkably, it is present even in the absence of clashes and electrostatic repulsions. It does, however, vanish in the limit of large distances between the tethering points (data not shown here). Inter-dye distances calculated excluding steric clashes are very similar to the interdye distances obtained for NaCl and glycerol, calculated excluding sterical clashes and taking into account electrostatic interactions corresponding to the isotropic scenario. Clearly, the effect of sterical clashes outweighs the effect of electrostatic repulsions in our approximation. Additionally, the difference between the resulting $\bar{R}_{DA}$ values for NaCl and glycerol is smaller than 1 $\mathring{A}$ considering the whole distance regime. Furthermore, the anisotropic scenario is tested since it represents a kind of extreme case of electrostatic interaction and can give an idea of upper boundaries concerning interdye distance changes. Even here, the maximal difference between $\bar{R}_{DA}$ for NaCl and glycerol lies around 3 $\mathring{A}$.

As a last step, with the help of equation 4.23, one can define an average inter-dye distance by means of the average FRET efficiency. Here, $\bar{E}$ is calculated according to:

$$\bar{E} = \int_{AV,A} \int_{AV,D} d\vec{r}_A d\vec{r}_D P(\vec{r}_A, \vec{r}_D) \frac{1}{1 + \left(\frac{|\vec{r}_A - \vec{r}_D|}{R_0}\right)^6} \tag{5.29}$$

The obtained result can be compared to the directly calculated inter-dye distances, as is shown in figure 5.30 (b) assuming an isotropic charge distribution and NaCl and glycerol as solvents. Obviously, the inter-dye distances

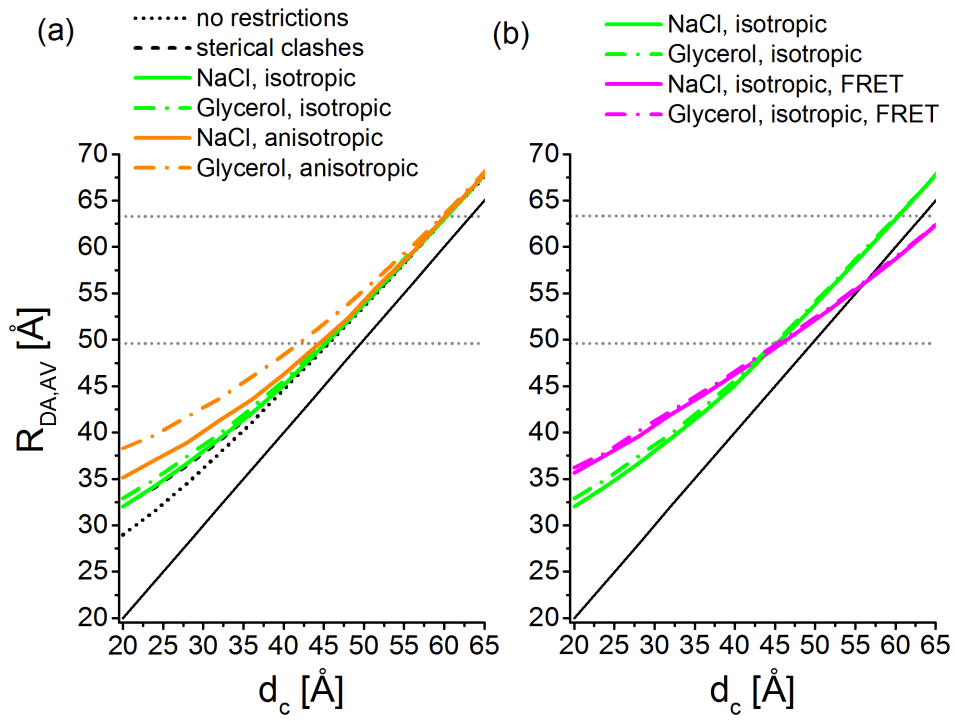

Figure 5.30: (a) Inter-dye distances plotted as a function of the distance d_c between the centroids of the spherical AVs of donor and acceptor. As black solid line, $\bar{R}_{DA} = d_c$ is depicted. The dotted black line shows the inter-dye distance calculated without any restrictions, whereas the dashed black line is calculated excluding steric clashes (partly hidden by solid green line). As green solid (NaCl) and dashed-dotted (glycerol) lines, the inter-dye distances corresponding to the isotropic electrostatic scenario are given, whereas the solid and dashed-dotted orange lines represent the results based on the anisotropic electrostatic scenario. (b) Directly calculated inter-dye distances (green) and FRET-efficiency based inter-dye distances (magenta) plotted as a function of the distance d_c. Electrostatic interactions correspond to the isotropic regime. Development and implementation of extended AV algorithm achieved and raw data provided by Simón Poblete.

taken from FRET efficiencies show a different pattern than the directly calculated ones. However, it is obvious that in this case the contribution of sole electrostatic interactions is even smaller than before.

Finally, using these rough approximations, it can be stated that even for short inter-dye distances around 30 $\AA$ a change of the solvent environment leads to a relative difference in $\bar{R}_{DA}$ of below 10 %. Nonetheless, additional effects such as solvent mediated interactions and higher resolution electrostatic contributions could still play a significant role and should be considered separately [67].

5.5.4 Coil-globule transition of Phosphoglycerate-Kinase

Sample introduction

In this section, the chemically induced unfolding of the two-domain protein Phosphoglycerate Kinase (PGK) will be studied. As before, AL488 and AL647 are chosen as donor and acceptor fluorophores, here attached to positions 1 and 135 of the N-terminal domain (see figure 5.31 for protein

structure and AV clouds). In addition to pure aqueous buffer, buffer solutions with high amounts of GdnHCl added (1, 1.5, 4, and 6 M) are employed.

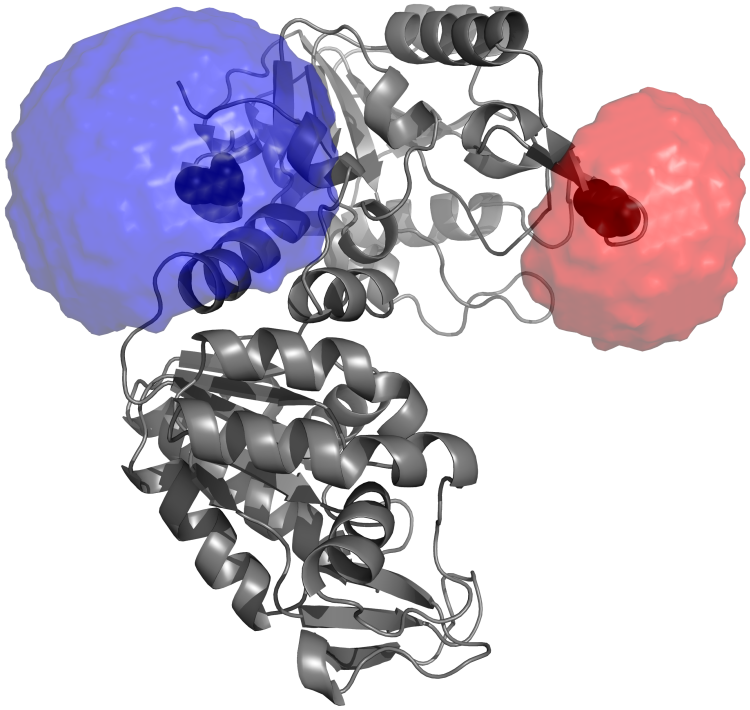

Figure 5.31: Crystal structure of PGK [PDB:1QPG] superimposed with the AVs of AL488 and AL647. Attachment positions at S1C (donor) and Q135C (acceptor) are shown as dark spheres.

Fluorescence lifetime analysis

As distinct from the previous case of the dsDNA oligonucleotides, the addition of high amounts of the denaturant GdnHCl is expected to cause the unfolding of the protein PGK. Hence, the properties of the fluorescent markers might not only be influenced by the solvent environment but also by variations in the protein-fluorophore-interaction.

To get a rough idea which process is the dominant one, the fluorescence lifetimes of the single-labeled single-mutants in the different solvents are determined. The obtained results are given in table 5.10. The donor fluorescence lifetime does not change with increasing denaturant concentration, but is in all cases significantly shorter than the lifetime of unattached AL488 ($\tau_{fl} \approx 4.1$ ns). Hence, it is rather a dye-protein than a dye-solvent interaction that causes this quenching of τ_{fl} of AL488. On the other hand, the acceptor lifetime is under all solvent conditions larger than the lifetime of unattached AL647 ($\tau_{fl} \approx 1.1$ ns), and increases going from pure buffer to 1 M GdnHCl to stay constant then. While the overall enhancement of the fluorescent lifetime appears to be independent from the solvent environment, the further increase going from 0 M to 1 M GdnHCl is an indirect solvent effect, as the lifetime reflects the interaction of the dye with the unfolded structure of the protein.

PGK S1C Solvent	AL488 τ_{fl} [ns]	AL647 τ_{fl} [ns]
PGK buffer	3.6 ± 0.1	1.5 ± 0.1
+ 1 M GdnHCl	3.6 ± 0.1	1.7 ± 0.1
+ 1.5 M GdnHCl	3.6 ± 0.1	1.7 ± 0.1
+ 4 M GdnHCl	3.6 ± 0.1	1.7 ± 0.1

Table 5.10: Fluorescence lifetimes of donor and acceptor attached to positions S1C and Q135C of PGK single mutants, measured in buffer with different amounts of GdnHCl added. No position dependency is observed, hence only one value is given for both mutants.

Assessment of the orientation factor κ^2

To assess the orientation factor κ^2, as before TRA measurements are employed. Here, the rotational mobility of donor and acceptor appears to trace the denaturant induced structural changes of PGK: the mobility of the dyes increases upon unfolding (which is reflected in both, the correlation time theta and the semi-cone angle alpha, see figure 5.32). For the donor, the obtained correlation times are smaller than the inverse FRET rate, whereas for the acceptor θ_r is on the time-scale of FRET in all cases. However, assuming that κ^2 can be replaced by its average value of 2/3, the determined inter-dye distance for PGK in aqueous buffer coincides with the distance predicted by AV calculations (see Figure 5.34). Therefore, the rather slow rotational correlation time of the acceptor does not seem to interfere with the assumption of dynamic orientational averaging. Consequently, all distances are determined using κ^2=2/3 (Förster radii in table B.7).

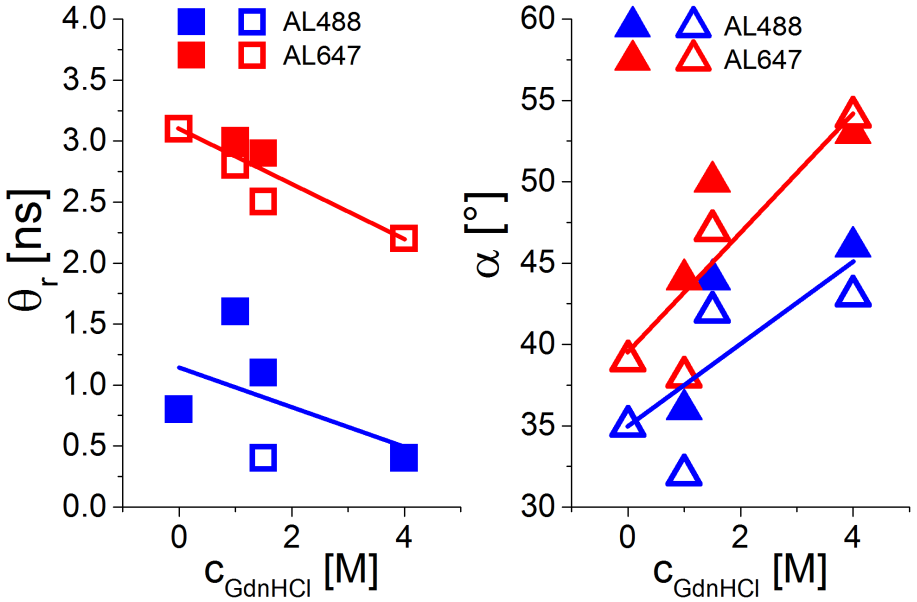

Figure 5.32: Rotational correlation time θ_r and semi-cone angle θ of PGK in GdnHCl solutions obtained by TRA measurements. Filled symbols represent the PGK mutant S1C, whereas empty symbols represent the mutant Q135C. With increasing denaturant concentrations, the rotational freedom of the fluorophores increases. The experimental values are reported in table B.5.

Determination of FRET calibration parameters

As before, the quantum yields of the labeled single mutants of PGK are determined with the help of the liFCS approach for each GdnHCl concentration. Again, value and error limit correspond to the mean and the standard deviation of three different measurement series. The obtained results are given in table 5.11, together with the respective transmission/detection efficiency parameter g.

PGK S1C/PGK Q135C	AL488		AL647	
Solvent	ϕ_{fl}	g	ϕ_{fl}	g
PGK buffer	0.87 ± 0.04	0.11	0.42 ± 0.02	0.12
+ 1 M GdnHCl	0.71 ± 0.04	0.10	0.50 ± 0.03	0.12
+ 1.5 M GdnHCl	0.77 ±0.04	0.10	0.61 ± 0.03	0.12
+ 4 M GdnHCl	0.81 ±0.04	0.09	0.54 ± 0.03	0.11
+ 6 M GdnHCl	0.77 ±0.04	0.08	0.55 ± 0.03	0.10

Table 5.11: Quantum yields and transmission/detection efficiency parameters for the single-labeled, single mutants of PGK in all solvents. As no position dependency is observed, only one value is given for both mutants.

smFRET measurements

Single-molecule measurements are performed as explained in detail in section 4.2.3. As distinct from the measurements of the dsDNA constructs, a photo-protection cocktail is used and the donor excitation intensity is set to ≈ 3000 a.u. [157]. The direct acceptor excitation power still lies around 400 a.u.. Again, PIE is employed and the burst selection time-window size T is fixed to 1 ms, adjusted to the molecule's dwell time in the effective volume obtained by FCS. Only FRET-bursts containing more than 80 photons are used to calculate transfer efficiencies. The fraction of double-labeled PGK, obtained by coincidence analysis, lies around 10 %.

The corresponding corrected and uncorrected FRET efficiency histograms are shown in figure 5.33. Strikingly, in all cases, the mean FRET-efficiencies of corrected and uncorrected histograms differ by more than 30 % (B.6). Furthermore, the widths of the histograms show relevant discrepancies. Especially at 1 M GdnHCl, the width of the corrected histogram shows a 40 % smaller deviation from the width of the shot-noise limited distribution than the corresponding width of the uncorrected histogram. This is of crucial importance for wide-spread analysis tools comparing variance of the data to get insight into the underlying molecular dynamics [12, 118]. In figure 5.34(a), the obtained inter-dye distances are depicted. As before, fully corrected distances, uncorrected distances, and n corrected distances are calculated. Here, only at 1.5 M GdnHCl significant differences between corrected and uncorrected R_{DA} - values show up (see also table B.8). Again, correcting for n only is not advisable. Although the protein is almost completely unfolded at 1 M GdnHCl with respect to secondary structure elements [86], an ongoing further expansion of the protein structure is observed in the regime from 1 M to 6 M GdnHCl. This phenomenon is well pronounced in the corrected as well as in the uncorrected R_{DA} values and was already observed for many other proteins (coil-globule transition going from high to low denaturant

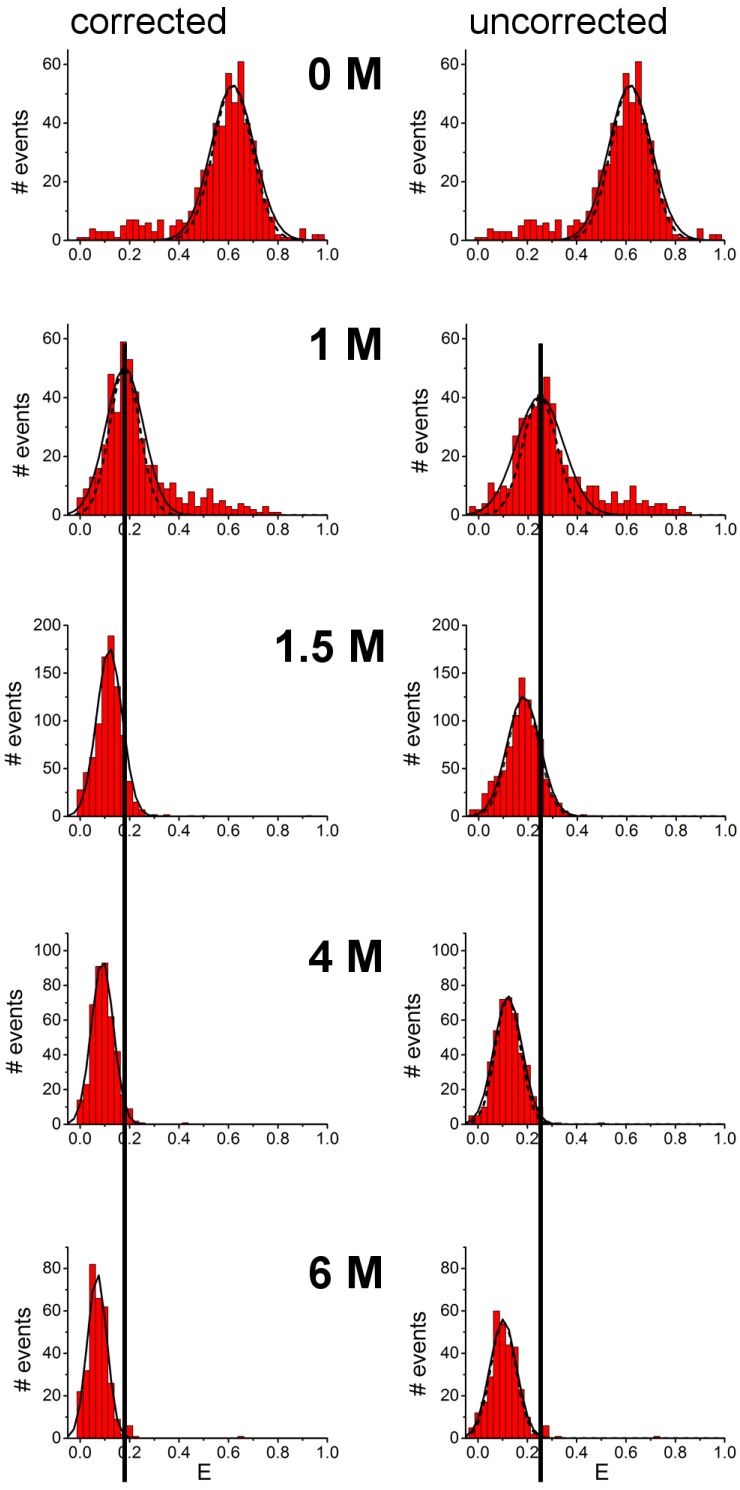

Figure 5.33: FRET-efficiency histograms of PGK in buffer with increasing amounts of GdnHCl added. The corrected histograms are calculated taking into account spectral and QY changes of the FRET pair, whereas the uncorrected histograms are calculated with the parameters determined for pure buffer. Black solid lines denote the Gaussian distributions best fitting the data. Black dashed lines depict the shot-noise limited distributions [112]. The vertical lines indicate the mean FRET-efficiency of the already unfolded state at 1 M GdnHCl. Measurements performed and raw data provided by Michele Cerminara.

concentrations [24–26, 73, 83]). In addition, (viscosity-corrected) hydrody-

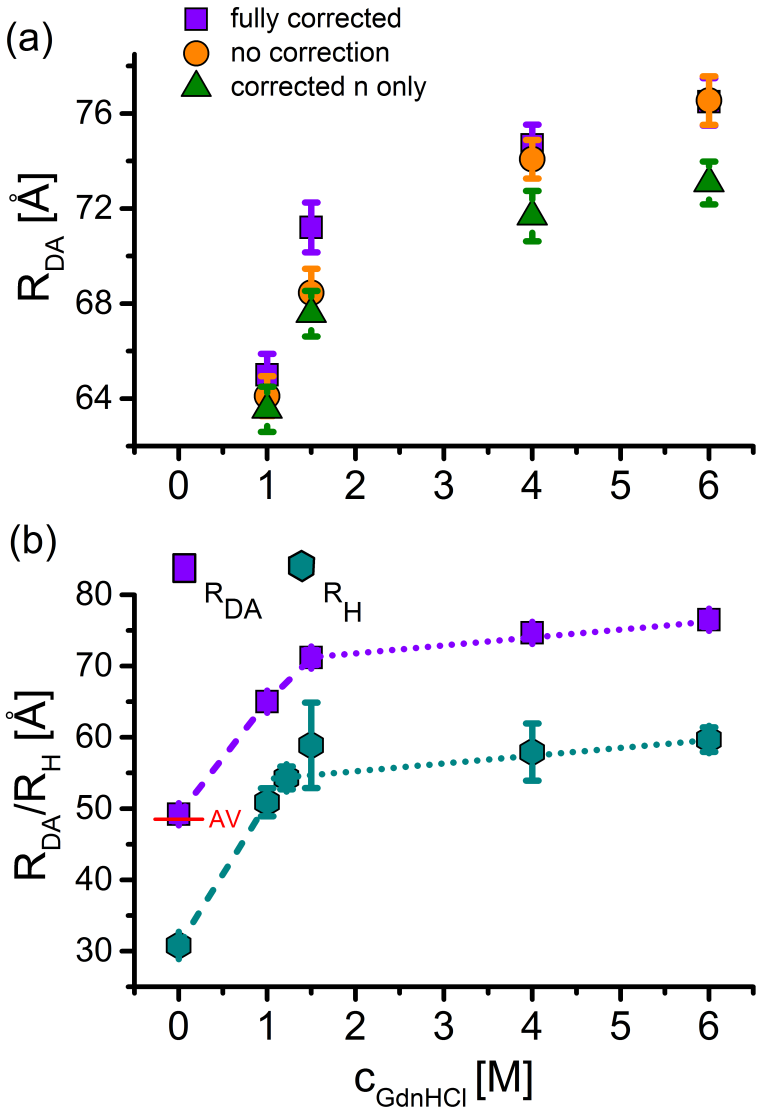

Figure 5.34: (a) Inter-dye distances (R_{DA}) of PGK at high GdnHCl concentrations: fully corrected (violet), uncorrected (orange) and corrected n only (green). (b) fully corrected R_{DA} values compared to hydrodynamic radii r_h from FCS data. The unfolding transition is indicated by a two-state fit with a mid-point at 0.7 M GdnHCl (dashed-lines), while the coil-globule transition is illustrated by the straight dotted lines. As red line, the inter-dye distance obtained by (standard) AV calculations is shown. Parameter used for AV calculation are given in table B.9.

namic radii r_h determined by FCS reflect exactly the same behavior (figure 5.34 (b), for details on viscosity determination see figure A.7). Although for the PGK mutant the overall impact of the applied corrections is small as compared to the dsDNA samples, now confidence about the development of the inter-dye distances for this protein structure under highly denaturing conditions is obtained. Clearly, the discrepancy between scattering and smFRET data concerning the coil-globule transition of the unfolded state (see figure 1.2) is not a result of potential artifacts due to solvent-induced changes of the properties of the fluorescent markers.

Chapter 6

Discussion/Outlook

6.1 Depolarization correction factors

To determine the depolarization factors for the setup at hand, the calibration procedure proposed by Koshioka et al. [158] was adjusted to detection systems with an IRF FWHM around 600 to 900 ps. For that, the rotational correlation time of the fluorophore AL488 was varied by adding increasing amounts of the viscosity enhancer glycerol to water. With the help of a support plane analysis (SPA) of the fitted k_1 and k_2 values and their corresponding confidence interval limits, it was shown that the rotational correlation time had to be increased by at least a factor of three ($\geq$ 37 wt. % glycerol added) to determine k_1 and k_2 with the required exactness. It is worth to mention that besides the fundamental anisotropy of AL488 no other fitting parameters had to be known in advance.

Using the theory by Fisz [38] to predict the values of k_1 and k_2 expected for the given measurement conditions, it was shown that the experimental values differed from the theoretical ones but, plotted as a function of the solvent refractive index, showed the same trend. The offset between theory and experiment was explained by the fact that no technical imperfections like polarization leakage of the polarizer cube, polarization bias due to the dichroic mirror [159] or reflections at interfaces were taken into account in the calculations. Forcing the obtained theoretical curve to coincide with the experimentally determined one, precise values of k_1 and k_2 (n(solvent)$\geq$1.38), the depolarization correction factors for measurements in solvents of refractive indices close to water could be figured out. Within the given error limits the results obtained for n=1.33, 1.37 and 1.40 coincided.

Comparing the determined values of k_1 and k_2 to values obtained in other works for objectives of similar numerical apertures is not reasonable. On the one hand, the amount of objective under-filling has to be known, on the other hand, the optical components built in play a significant role. This is also directly clear by the fact that in this work k_2 shows a dependency on the considered spectral regime which is theoretically not expected. It is important to mention that the asymmetry between convergence and divergence angle, caused by the objective under-filling, decreases the extent of depolarization significantly. Hence, although the detection angle is larger than 60°, the addition of the parallelly and perpendicularly polarized emissions component does not lead to a completely un-polarized fluorescence lifetime decay as might be expected [38].

Referring to ensemble measurements with no need of spatial confinement, the precise knowledge of k_1 and k_2 is rather redundant, as the high NA objective can simply be exchanged with a low NA objective eradicating

the depolarization difficulty. However, with respect to measurements at low or even single-molecule concentrations the employment of a high NA objective is essential to achieve the required signal-to-noise ratio, which makes the determination of k_1 and k_2 obligatory. Among others, single-molecule anisotropy measurements can be used to determine the mean mobility of the fluorescent markers used for single-molecule FRET. Hence, sub-populations showing different transfer efficiencies due to hindered rotational diffusion of donor or acceptor and not due to real (conformational) distance changes can be identified [23, 160].

6.2 Quantum yield determination by liFCS

To facilitate a fast quantum yield determination of samples at low ((sub)-nM) concentrations, the confocal microscopy based liFCS approach was developed and validated in this work. By proof-of-principle measurements it was demonstrated that the quantum yield values predicted by the liFCS approach coincided with the expected nominal values within the determined error limits of below $\pm$ 10 %. With the help of theoretical and experimental considerations, potential pitfalls due to a refractive index mismatch [51, 52] between objective design and actual solvent conditions were evaluated and overcome. In this regard, it was demonstrated that using specific measurement settings the impact of the refractive index mismatch on the effective FCS volume can be minimized. Then, only one calibration of the effective volume in a solvent of arbitrary refractive index is sufficient to analyze data sets obtained in other solvents. Consequently, by sticking to the appropriate measurement conditions, FCS measurements can be used to determine diffusion coefficients of fluorescent molecules in additive-enriched/crowded environments reliably, circumventing the need of more complex dual-focus FCS approaches [161].

To get an impression of the minimal sample amount needed for the liFCS-approach, the example of AL488 in PBS with a maximal absorption coefficient of ϵ_{max}=73000 $cm^{-1}M^{-1}$ shall be considered. Additionally, the obtained result is compared to the amount needed for the commonly employed standard method (see section 4.1.2). The minimal sample amount needed for the liFCS approach is the one that enables the measurement of a reliable absorption spectrum. Reliable in this respect means that noise fluctuations of the optical density (OD) should not bias the determination of the relative OD at the laser excitation wavelength. A standard steady-state absorption spectrometer has a baseline standard deviation of ΔOD$\approx$0.0002. Aiming for a high signal-to-noise ratio of 50 for the maximal OD ensures that also the OD at the laser excitation wavelength a bit off the maximum value is still well-defined. Generally, the needed amount of fluorophore, n_{min}, equals:

$$n_{min} = \frac{OD_{max} \cdot V}{\epsilon_{max} \cdot d} \tag{6.1}$$

Here, V is the sample volume and d is the cuvette path length. Assuming the use of a cuvette with a 5 cm path length and a volume of 3.5 ml and an OD_{max} around 0.01, the needed amount of AL488 equals 82 pmol. Using a micro-spectrophotometer with a path length of 0.1 cm and a sample volume of 2 µl, the needed amount further decreases to 2.7 pmol. With respect to

the standard approach, the ODs of the dilution series have to be determined as precise as possible, therefore the use of a cuvette with a 5 cm path length is recommended. The fluorescence intensity depends linearly on the OD up to a value of around 0.05, therefore the amount of sample needed for the dilution series lies between $\approx$ 80 and 300 pmol. However, using the micro-spectrophotometer is not possible in the standard approach. Measuring an OD of $\approx$ 0.05 with the spectrophotometer requires a concentration of around 6.8 µM. Using a standard fluorescence cuvette with a path length of 1 cm as recommended for the standard method, the OD of the sample would lie around 0.5>0.05. Consequently, the standard approach is not compatible with the use of a micro-spectrophotometer. Hence, the liFCS approach works with an at least 30 times smaller sample amount than the standard method, which is of specific importance considering applications where only very small amounts of sample are available or where the sample tends to aggregate using higher concentrations. Obviously, a confocal microscopy based determination of the absorption cross section would reduce the needed sample amount further. Assuming a sample concentration of approximately 5 nM, an effective volume of 0.5 fl and a sample volume of 20 µl, the needed amount of substance would lie around 0.07 pmol. In this regard, one possibility to assess the absorption cross section is to determine the triplet fraction and relaxation time in an excitation intensity dependent manner and to globally fit the obtained curves, with the absorption cross section being one of the fitting parameters [131]. Unfortunately, the absorption cross section values obtained in this way have large relative error limits lying between 20 and 40 %, which is much too inaccurate with respect to the liFCS quantum yield determination.

As distinct from the frequently employed quantum yield determination based on fluorescence lifetime measurements [43], it was shown that the liFCS approach is sensitive to static and dynamic fluorescence quenching. This is of specific importance for fluorescent markers attached to biomolecules, as specific amino acids (like Tryptophane or Histidine) or nucleobases are known to exhibit a combination of dynamic and static quenching with respect to certain fluorophores [148, 162]. The fundamental assumption underlying the lifetime based quantum yield determination is that the natural lifetimes of reference and sample coincide. Indeed, the natural lifetime depends on the fluorophore environment, among others on the refractive index, the viscosity and the pH [145, 163, 164]. This was also demonstrated in this work by monitoring the natural lifetime of two dyes in glycerol solutions of increasing viscosity and refractive index, pointing out that the natural lifetime reacts highly sensitive but rather unpredictable to its surroundings. Consequently, considering additive-enriched solutions the fluorescence lifetime based quantum yield determination appears doubtful, supporting the need of a more reliable, confocal microscopy based approach like the one introduced in this work.

Another recently proposed, more elaborate lifetime based approach for the quantum yield determination employs a confocal microscope equipped with a custom-built nano-cavity [57, 58]. The outstanding strength of the method lies in the fact that quantum yield values of specific components of a mixture of fluorophores are obtained even if the different sub-populations have overlapping spectra. Without depreciating the superiority of the method with respect to heterogeneous samples, it is clear that the impact of

static quenching on the quantum yield would be missed also in this case.

With regard to samples containing several fluorescent sub-populations, it is important to mention that the liFCS approach only works for samples characterized by a single brightness value. Even for the simplest case of a bi-molecular sample with two different MB-values, the apparent number of particles in the effective volume is given by [43]:

$$\bar{n}_{app} = \frac{\bar{n}_1 MB_1 + \bar{n}_2 MB_2}{\bar{n}_1 MB_1{}^2 + \bar{n}_2 MB_2{}^2} \tag{6.2}$$

Here, $\bar{n}_{1,2}$ are the average numbers of species one and two in the effective volume and MB_1 and MB_2 are the corresponding brightness values of each species. Consequently, the determination of the MB of one species is coupled to the knowledge of the MB of the other species and the exact number distribution of the complete sample. This is experimentally impossible without a prior assessment of the sample or the use of any other complementary technique like PCH [165] for instance.

Finally, it is worth to mention that, as distinct from the cuvette based standard method, the liFCS approach facilitates a more reliable quantum yield determination in terms of the underlying sample quality. This is due to the fact that, using an FCS based method, the sample diffusion coefficient or even the raw intensity time trace indicate the existence of larger oligomeric structures or aggregates otherwise potentially overseen. If these artifact structures induce changes of the quantum yield by quenching or any other mechanism, the standard method will provide an average quantum yield of the monomeric and the oligomeric/aggregated population. Using the liFCS approach, samples with aggregates can simply be excluded from further analysis steps.

6.3 smFRET measurements in additive-enriched solutions

It was demonstrated that high amounts of additives can significantly alter the properties of aqueous solutions, which potentially has an impact on the characteristics of the fluorescent markers used as FRET pair. In this respect, it was shown that in particular the explicit determination of correct quantum yields for all attachment positions and for all environmental conditions is essential, which underlines the usefulness of the liFCS approach.

In particular for smFRET studies of proteins, the attached dyes are not only affected by the specific solvent properties but also by potential interactions with the local polypeptide chain environment. This can lead to a drastic deviation of their quantum yields as compared to those typically known for the free fluorophores in aqueous buffer solutions. Therefore, a simple interpolation between values obtained at low and at high co-solvent concentrations would likely be erroneous, meaning that each value at each environmental condition has to be measured explicitly. From the magnitude of the individually observed parameters ($\phi_{fl,A}$,$\phi_{fl,D}$,R_0) it is not straightforward to estimate the magnitude of the overall correction in terms of R_{DA}. Beyond that, the application of corrections for only one or a few parameters can be hazardous because it can give rise to even stronger deviations from the fully corrected R_{DA}-values.

A special case of interest where potential artifacts and required corrections in smFRET results play an important role is given by the question which structural properties unfolded proteins develop upon increasing denaturant concentrations beyond the unfolding transition. A clear answer is not only of relevance concerning the process of protein folding, but also for the function of the myriad of intrinsically disordered proteins [166]. Just recently, a detailed description of the conformational ensemble of denatured ubiquitin was obtained by comparing smFRET data with ensembles computed using NMR/SAXS restrains, confirming the occurrence of the coil-globule transition [166]. However, since for many single domain proteins such an ongoing expansion with increasing denaturant concentrations is not observed by small-angle X-ray scattering (see [167] and references therein), the question arises whether in smFRET studies methodical deficiencies systematically bias the obtained results. From the presented analysis of a mutant of PGK a clear coil-globule transition behavior at elevated GdnHCl concentrations is observed. This result gives, on the one hand, additional reliability qualified by the application of a thorough parameter correction and, on the other hand, by an independent measure of the hydrodynamic radii under identical sample conditions.

Possible inter-dye interactions caused by electrostatics between charged dyes (acceptor and donor carry net-charges) and modified by different types of solvent (with different dielectric permittivity and ionic strength) were shown to have no impact on the obtained results. In reference measurements of dsDNA constructs with inter-dye distances of 49 $\mathring{A}$ and 61 $\mathring{A}$, only small differences in inter-dye distances between pure buffer and buffer of high GdnHCl concentration were observed. Consequently, electrostatic dye-dye repulsions do not explain the GdnHCl induced increase of inter-dye distances determined for PGK. In contrast to the PGK mutant considered here, most of the other proteins for which a pronounced coil-globule transition was observed were much smaller and therefore, the native inter-dye distance was also smaller (i.e. well below the Förster radius of around 50 $\mathring{A}$). However, for the unfolded states, the observed inter-dye distances with transfer efficiency values between 0.4 and 0.7 fell into the same distance regime as considered in the example of dsDNA. Consequently, also in these cases one can be confident that electrostatic dye-dye interactions are negligible.

Additionally, it can be stated that the presented methodical approaches are not only applicable to the rather simple buffer solutions which were investigated in this thesis, but also to more complex buffer compositions consisting of macromolecular crowding agents or even cytosolic solutions. In this regard, the contribution of auto-fluorescence to the measured signal is a severe issue, which can potentially be minimized by bleaching [168]. However, efficient bleaching is mainly achieved by using very small amounts of sample (µl range) that are exposed to strong laser beams, which underpins the relevance of the proposed confocal microscopy based calibration/characterization schemes once more.

Appendix A

Appendix

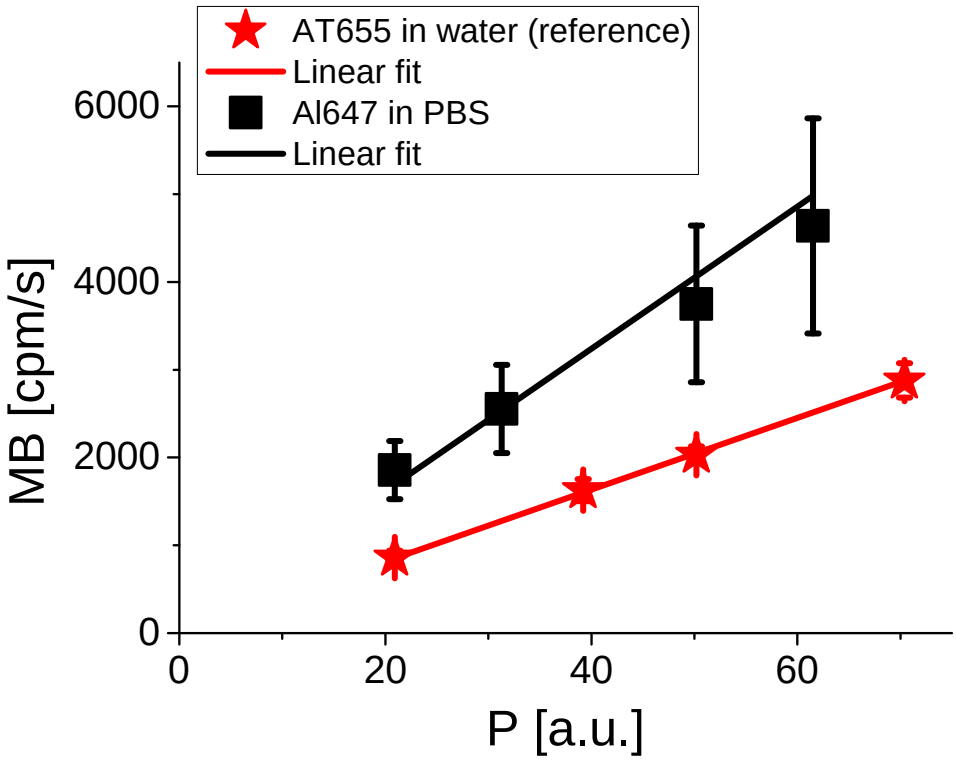

Figure A.1: *MB*-curves of AL647 in PBS and AT655 in water.

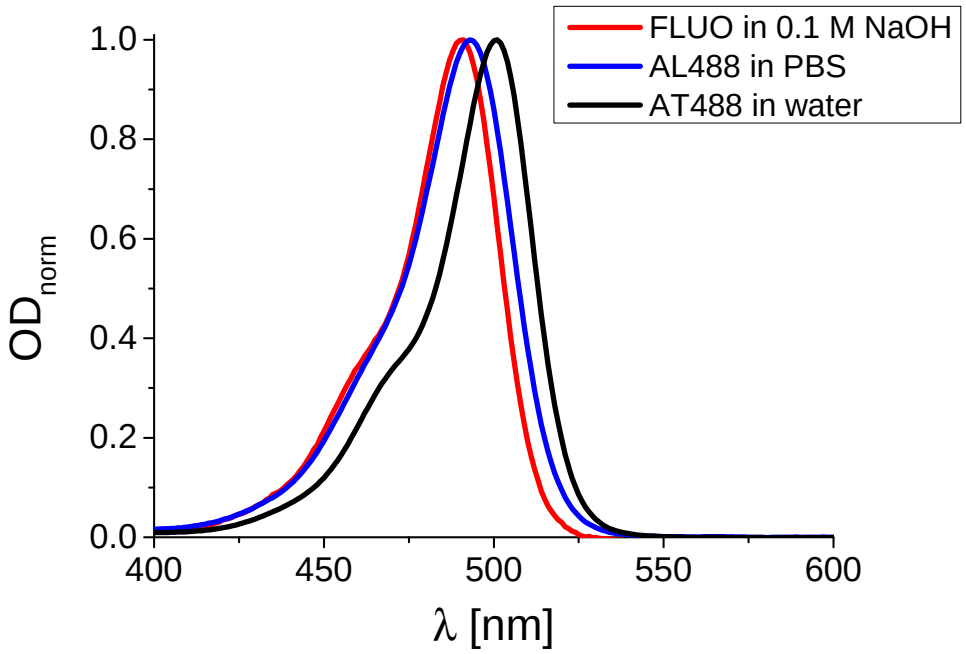

Figure A.2: Absorption spectra of FLUO in 0.1 M NaOH, AL488 in PBS and AT488 in water.

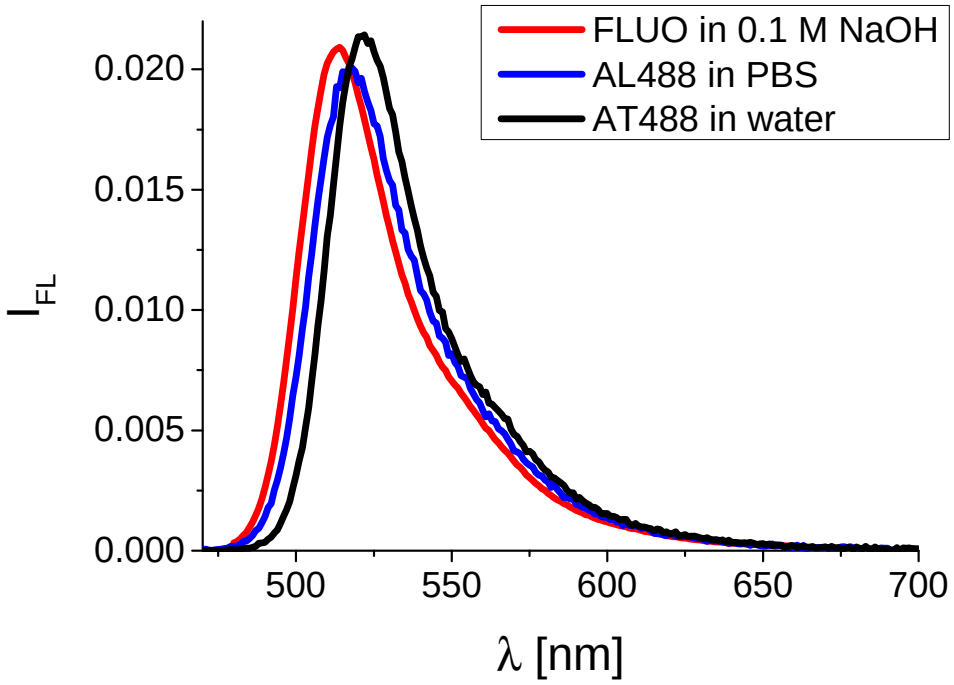

Figure A.3: Fluorescence emission spectra of FLUO in 0.1 M NaOH, AL488 in PBS and AT488 in water.

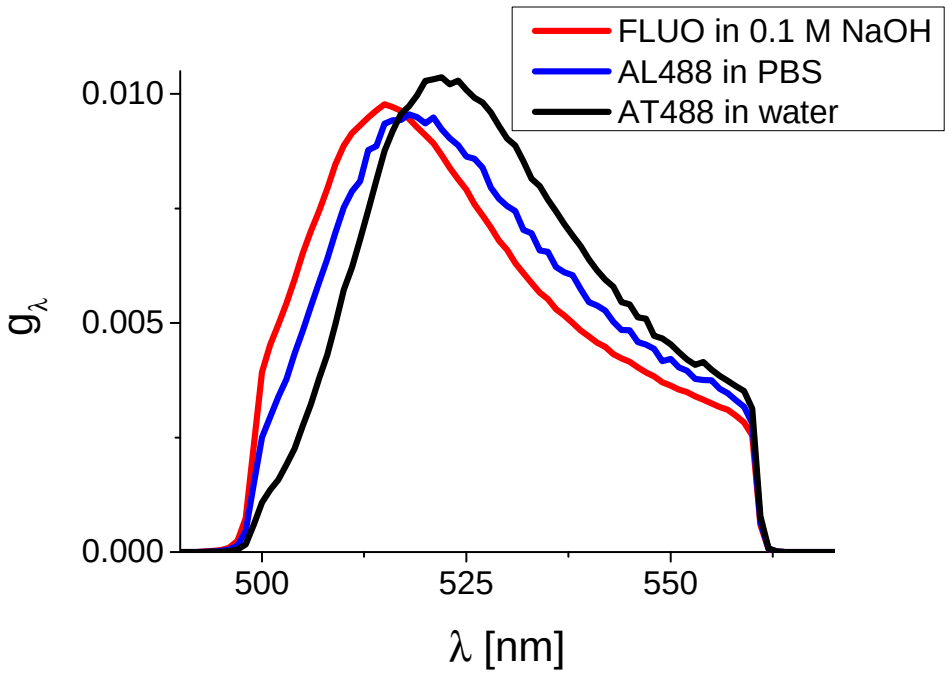

Figure A.4: Transmission function for FLUO in 0.1 M NaOH, AL488 in PBS and AT488 in water.

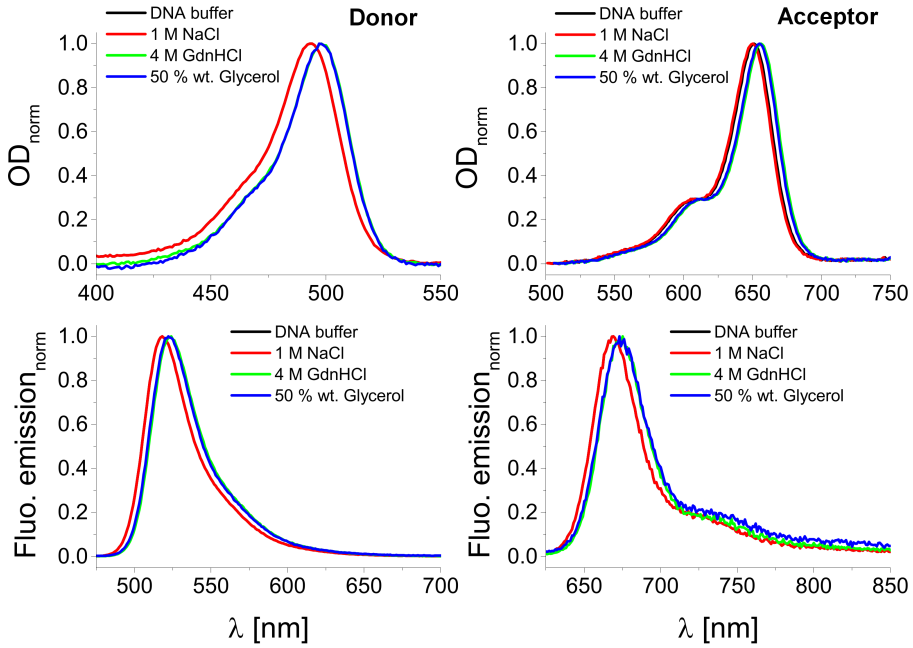

Figure A.5: Left side: Absorption and emission spectra of AL488 (donor) labeled 10 bp DNA oligo-nucleotides in different solvents. Right side: Corresponding spectra for the DNA construct labeled with AL647 (acceptor). Spectra measured in buffer and in buffer with 1 M NaCl added coincide in all cases.

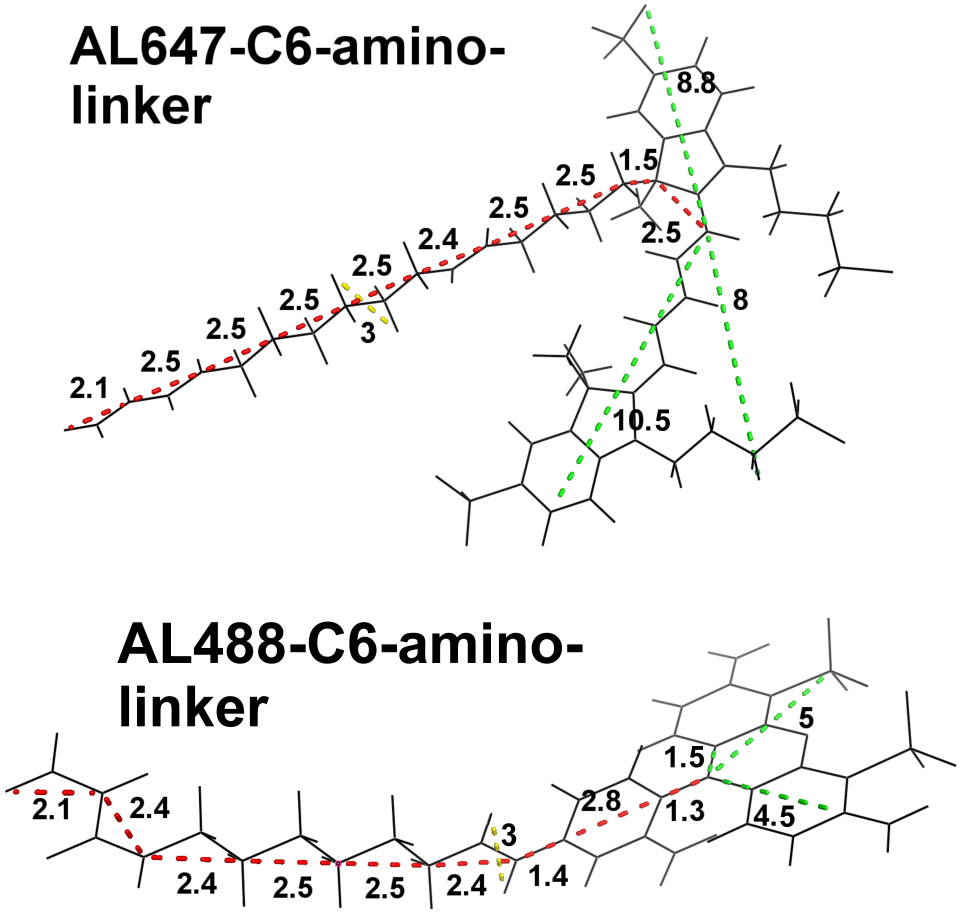

Figure A.6: AL647/AL488-C6-amino-linker structure. Dye radii indicated by green dashed lines. Linker lengths equal the rounded sum of all red fragments, linker width depicted as yellow dashed line. All distance labels in $\mathring{A}$.

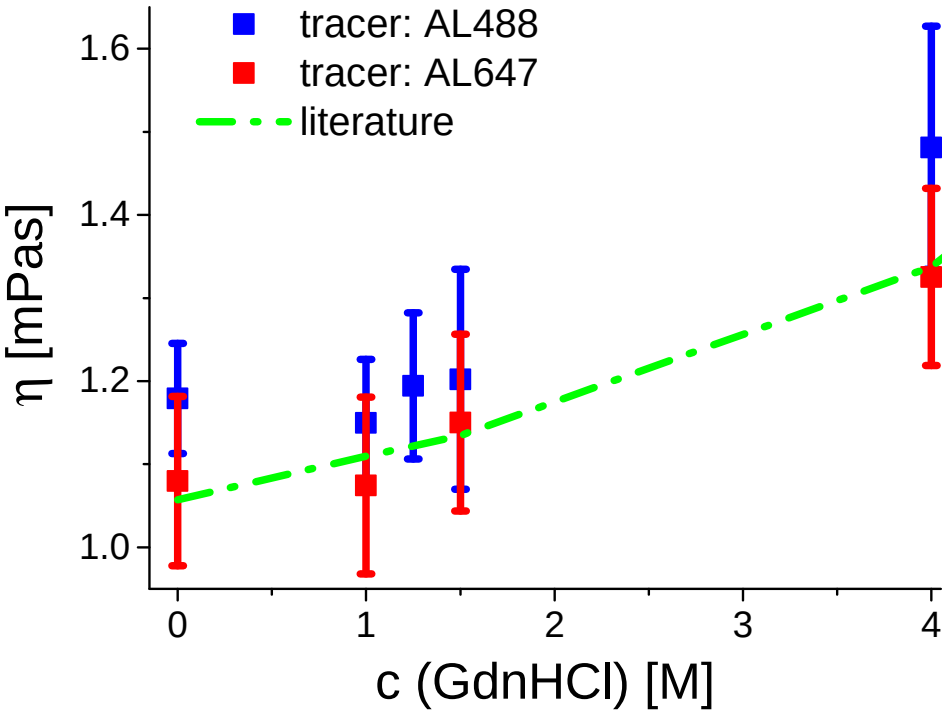

Figure A.7: Dynamic viscosity η plotted as a function of the concentration of GdnHCl. As green dashed-dotted line, an empirical relation known from the literature is depicted [61]. Red and blue squares correspond to experimentally determined viscosity values. In the latter case, the diffusion coefficients of AL488 and AL647 dissolved in pure water and in buffer solutions with increasing amounts of GdnHCl added are determined by FCS. All measurements are performed at a temperature of 22° C. Assuming that the hydrodynamic radius of the fluorophores is not affected by GdnHCl and equivalent to the one obtained in water, equation 5.17 can be employed to determine the unknown viscosities. Experimental and theoretical results show reasonable agreement.

Appendix B

Appendix

wt. % Glycerol	n	η [mPas]	D_t [$\frac{\mu m^2}{s}$]
0	1.333	1.01	362 ± 6
6	1.340	1.18	309 ± 5
10	1.345	1.31	278 ± 4
14	1.350	1.46	249 ± 4
22	1.360	1.88	194 ± 3
29	1.369	2.41	151 ± 2
37	1.379	3.28	111 ± 2
44	1.389	4.45	82 ± 1
51	1.399	6.33	58 ± 1
58	1.409	9.52	38 ± 1

Table B.1: Refractive indices n and dynamic viscosities η of Glycerol solutions and the corresponding translational diffusion coefficients D_t as predicted by the Stokes-Einstein equation. The hydrodynamic radius of AL488 equals r=0.59 $\pm$ 0.01 as was shown by complementary time-resolved anisotropy measurements.

10 bp DNA-construct		
Solvent	$\bar{E}_{corr}$	$\bar{E}_{uncorr}$
DNA buffer	0.613	0.613
+ 1 M NaCl	0.586	0.632
+ 4 M GdnHCl	0.528	0.689
+ 50 wt. % Glycerol	0.549	0.620
17 bp DNA-construct		
Solvent	$\bar{E}_{corr}$	$\bar{E}_{uncorr}$
DNA buffer	0.3	0.3
+ 1 M NaCl	0.266	0.296
+ 4 M GdnHCl	0.229	0.353
+ 50 wt. % Glycerol	0.266	0.313

Table B.2: Corrected and uncorrected mean FRET efficiencies for the dsDNA oligonucleotides. Uncorrected FRET efficiencies are calculated using the calibration parameters determined for pure buffer.

10 bp DNA-construct		
Solvent	R_{0corr} [Å]	$R_{0n,corr}$ [Å]
DNA buffer	52.7	52.7
+ 1 M NaCl	52.6	52.5
+ 4 M GdnHCl	50.9	51.0
+ 50 wt. % Glycerol	52.7	51.0
17 bp DNA-construct		
Solvent	R_{0corr} [Å]	$R_{0n,corr}$ [Å]
DNA buffer	53.4	53.4
+ 1 M NaCl	53.5	53.3
+ 4 M GdnHCl	51.7	51.8
+ 50 wt. % Glycerol	53.7	51.8

Table B.3: Fully corrected and refractive index corrected Förster radii for the dsDNA constructs in different solvents.

10 bp DNA-construct			
Solvent	R_{DAcorr} [Å]	$R_{DAuncorr}$ [Å]	$R_{DAn,corr}$ [Å]
DNA buffer	48.8 ± 0.8	48.8 ± 0.8	48.8 ± 0.8
+ 1 M NaCl	49.6 ± 1.0	48.1 ± 0.8	47.9 ± 0.9
+ 4 M GdnHCl	50.0 ± 0.9	46.1 ± 0.8	44.6 ± 1.0
+ 50 wt. % Glycerol	51.0 ± 0.9	48.5 ± 0.8	47.0 ± 0.8
17 bp DNA-construct			
Solvent	R_{DAcorr}	$R_{DAuncorr}$	$R_{DAn,corr}$
DNA buffer	61.7 ± 1.0	61.7 ± 1.0	61.7 ± 1.0
+ 1 M NaCl	63.3 ± 1.1	61.8 ± 1.1	61.6 ± 1.1
+ 4 M GdnHCl	63.3 ± 1.1	59.2 ± 1.0	57.3 ± 0.9
+ 50 wt. % Glycerol	63.7 ± 1.1	61.0 ± 1.1	59.0 ± 1.1

Table B.4: Corrected, uncorrected and refractive index corrected inter-dye distances for the dsDNA constructs in different solvents.

PGK S1C/Q135C	**AL488**		**AL647**	
Solvent	θ_r **[ns]**	θ_{max} [°]	θ_r **[ns]**	θ_{max} [°]
PGK buffer	0.8 ± 0.1	35 ± 1	3.1 ± 0.1	39 ± 1
+ 1 M GdnHCl	1.6 ± 0.1	$36/32 \pm 1$	$3.0/2.8 \pm 0.1$	$44/38 \pm 1$
+ 1.5 M GdnHCl	$1.1/0.4 \pm 0.1$	$44/42 \pm 1$	$2.9/2.5 \pm 0.1$	$50/47 \pm 1$
+ 4 M GdnHCl	0.4 ± 0.1	$46/43 \pm 1$	2.2 ± 0.1	$53/54 \pm 1$

Table B.5: Rotational correlation (θ_r) times and semi-cone angle (θ_{max}) for labeled PGK single mutants obtained by TRA measurements. Values before slash correspond to mutant S1C, values behind slash to mutant Q135C. If only one value is given, both values coincide.

10 bp DNA-construct		
Solvent	$\bar{E}_{corr}$	$\bar{E}_{uncorr}$
PGK buffer	0.617	0.617
+ 1 M GdnHCl	0.180	0.248
+ 1.5 M GdnHCl	0.118	0.181
+ 4 M GdnHCl	0.090	0.122
+ 6 M GdnHCl	0.069	0.102

Table B.6: Corrected and uncorrected mean FRET efficiencies for the double-labeled PGK mutant S1C Q135C. Uncorrected FRET efficiencies are calculated using the calibration parameters determined for pure buffer.

Solvent	R_{0corr} [$\mathring{A}$]	$R_{0n,corr}$ [$\mathring{A}$]
PGK buffer	53.3	53.3
+ 1 M GdnHCl	50.5	52.8
+ 1.5 M GdnHCl	50.9	52.6
+ 4 M GdnHCl	50.8	51.5
+ 6 M GdnHCl	49.5	50.9

Table B.7: Fully corrected and refractive index corrected Förster radii for the PGK mutant S1C Q135C labeled with AL488 and AL647.

Solvent	R_{DAcorr} [$\mathring{A}$]	$R_{DAuncorr}$ [$\mathring{A}$]	$R_{DAn,corr}$ [$\mathring{A}$]
PGK buffer	49.2 ± 1	49.2 ± 1	49.2 ± 1.0
+ 1 M GdnHCl	65.0 ± 0.9	64.1 ± 0.8	63.5 ± 1.0
+ 1.5 M GdnHCl	71.2 ± 1.1	68.5 ± 1.0	67.6 ± 1.0
+ 4 M GdnHCl	74.7 ± 0.9	74.1 ± 0.8	71.7 ± 1.1
+ 6 M GdnHCl	76.5 ± 1	76.5 ± 1.0	73.1 ± 0.9

Table B.8: Corrected, uncorrected and refractive index corrected inter-dye distances for PGK S1C Q135C in different solvents.

Sample	**Linker length** [$\mathring{A}$]	**Linker width** [$\mathring{A}$]	**Radius 1** [$\mathring{A}$]	**Radius 2** [$\mathring{A}$]	**Radius 3** [$\mathring{A}$]
AL488	15.9	4.5	5	4.5	1.5
AL647	11.5	3	10.5	8.8	8

Table B.9: Parameters used to describe the linker-fluorophore unit attached to PGK.

Bibliography

[1] B. Huang, M. Bates, and X. Zhuang. "Super-Resolution Fluorescence Microscopy". In: *Annual Review of Biochemistry* 78 (2009), pp. 993–1016.

[2] F. Balzarotti et al. "Nanometer resolution imaging and tracking of fluorescent molecules with minimal photon fluxes". In: *Science* (2016).

[3] M. Orrit, T. Ha, and V. Sandoghdar. "Single-molecule optical spectroscopy". In: *Chemical Society Reviews* 4 (2014), pp. 963–1340.

[4] W. E. Moerner and L. Kador. "Optical detection and spectroscopy of single molecules in a solid". In: *Phys. Rev. Lett.* 62 (21 1989), pp. 2535–2538.

[5] W. E. Moerner and L. Kador. "Finding a single molecule in a haystack". In: *Analytical Chemistry* 61.21 (1989), 1217A–1223A.

[6] M. Orrit and J. Bernard. "Single pentacene molecules detected by fluorescence excitation in a p-terphenyl crystal". In: *Phys. Rev. Lett.* 65 (21 1990), pp. 2716–2719.

[7] E. B. Shera et al. "Detection of single fluorescent molecules". In: *Chemical Physics Letters* 174.6 (1990), pp. 553 –557.

[8] R. Rigler and U. Mets. "Diffusion of single molecules through a Gaussian laser beam". In: *Proc. SPIE* 1921 (1993), pp. 239–248.

[9] P. Tinnefeld and M. Sauer. "Branching Out of Single-Molecule Fluorescence Spectroscopy: Challenges for Chemistry and Influence on Biology". In: *Angewandte Chemie International Edition* 44.18 (2005), pp. 2642–2671.

[10] C. Eggeling et al. "Data registration and selective single-molecule analysis using multi-parameter fluorescence detection". In: *Journal of Biotechnology* 86.3 (2001), pp. 163 –180.

[11] W. E. Moerner and D. P. Fromm. "Methods of single-molecule fluorescence spectroscopy and microscopy". In: *Review of Scientific Instruments* 74.8 (2003), pp. 3597–3619.

[12] J. P. Torella et al. "Identifying Molecular Dynamics in Single-Molecule FRET Experiments with Burst Variance Analysis". In: *Biophysical Journal* 100.6 (2011), pp. 1568 –1577.

[13] P. G. Wolynes, J. N. Onuchic, and D. Thirumalai. "Navigating the folding routes". In: *Science* 267.5204 (1995), pp. 1619–1620.

[14] T. Förster. "Energiewanderung und Fluoreszenz". In: *Naturwissenschaften* 33.6 (1946), pp. 166–175.

[15] T. Förster. "Zwischenmolekulare Energiewanderung und Fluoreszenz". In: *Annalen der Physik* 437.1-2 (1948), pp. 55–75.

[16] S. Weiss. "Measuring conformational dynamics of biomolecules by single molecule fluorescence spectroscopy". In: *Nature Structural Molecular Biology* 7.9 (2000), pp. 724–729.

[17] L. Stryer and R. P. Haugland. "Energy transfer: a spectroscopic ruler". In: *Proceedings of the National Academy of Sciences* 58.2 (1967), pp. 719–726.

[18] A. A. Deniz et al. "Single-pair fluorescence resonance energy transfer on freely diffusing molecules: Observation of Förster distance dependence and subpopulations". In: *Proceedings of the National Academy of Sciences* 96.7 (1999), pp. 3670–3675.

[19] Ashok A. Deniz et al. "Single-molecule protein folding: Diffusion fluorescence resonance energy transfer studies of the denaturation of chymotrypsin inhibitor 2". In: *Proceedings of the National Academy of Sciences* 97.10 (2000), pp. 5179–5184.

[20] B. Schuler, E. A. Lipman, and W. A. Eaton. "Probing the free-energy surface for protein folding with single-molecule fluorescence spectroscopy". In: *Nature* 419.6908 (2002), pp. 743–747.

[21] E. Rhoades, E. Gussakovsky, and G. Haran. "Watching proteins fold one molecule at a time". In: *Proceedings of the National Academy of Sciences* 100.6 (2003), pp. 3197–3202.

[22] Z. Wang, L.A. Campos, and V. Muñoz. "Chapter Fourteen - Single-Molecule Fluorescence Studies of Fast Protein Folding". In: *Single-Molecule Enzymology: Fluorescence-Based and High-Throughput Methods*. Ed. by M. Spies and Y. R. Chemla. Vol. 581. Methods in Enzymology. Academic Press, 2016, pp. 417 –459.

[23] M. Margittai et al. "Single-molecule fluorescence resonance energy transfer reveals a dynamic equilibrium between closed and open conformations of syntaxin 1". In: *Proceedings of the National Academy of Sciences* 100.26 (2003), pp. 15516–15521.

[24] E. V. Kuzmenkina, C. D. Heyes, and G. U. Nienhaus. "Single-molecule FRET Study of Denaturant Induced Unfolding of RNase H". In: *Journal of Molecular Biology* 357.1 (2006), pp. 313 –324.

[25] A. Borgia, P. M. Williams, and J. Clarke. "Single-Molecule Studies of Protein Folding". In: *Annual Review of Biochemistry* 77.1 (2008), pp. 101–125.

[26] K. A. Merchant et al. "Characterizing the unfolded states of proteins using single-molecule FRET spectroscopy and molecular simulations". In: *Proceedings of the National Academy of Sciences* 104.5 (2007), pp. 1528–1533.

[27] P. R. Banerjee and A. A. Deniz. "Shedding light on protein folding landscapes by single-molecule fluorescence". In: *Chem. Soc. Rev.* 43 (4 2014), pp. 1172–1188.

[28] S. Kalinin et al. "A toolkit and benchmark study for FRET-restrained high-precision structural modeling". In: *Nature Methods* 9.12 (2012), pp. 1218–1225.

[29] A. Muschielok et al. "A nano-positioning system for macromolecular structural analysis". In: *Nature Methods* 5.11 (2008), pp. 965–971.

[30] J. Nagy et al. "Complete architecture of the archaeal RNA polymerase open complex from single-molecule FRET and NPS". In: *Nature Communications* 6 (2015).

[31] A. J. Trexler and E. Rhoades. "Single Molecule Characterization of α-Synuclein in Aggregation-Prone States". In: *Biophysical Journal* 99.9 (2010), pp. 3048 –3055.

[32] M. Iljina et al. "Kinetic model of the aggregation of alpha-synuclein provides insights into prion-like spreading". In: *Proceedings of the National Academy of Sciences* 113.9 (2016), E1206–E1215.

[33] L. Tosatto et al. "Single-molecule FRET studies on alpha-synuclein oligomerization of Parkinsons disease genetically related mutants". In: *Scientific Reports* 5 (2015), pp. 1–12.

[34] N. Hildebrandt. "How to Apply FRET: From Experimental Design to Data Analysis". In: *FRET-Förster Resonance Energy Transfer: From Theory to Applications*. Ed. by I. Medintz and N. Hildebrandt. Wiley-VCH Verlag GmbH and Co. KGaA, 2013, pp. 105–164.

[35] S. G. Schulman and A. C. Capomacchia. "Variations of fluorescence quantum yields with pH or Hammett acidity. Near equilibrium vs nonequilibrium excited state proton exchange". In: *The Journal of Physical Chemistry* 79.14 (1975), pp. 1337–1343.

[36] S. Sharafy and K. A. Muszkat. "Viscosity dependence of fluorescence quantum yields". In: *Journal of the American Chemical Society* 93.17 (1971), pp. 4119–4125.

[37] H.-J. van Manen et al. "Refractive Index Sensing of Green Fluorescent Proteins in Living Cells Using Fluorescence Lifetime Imaging Microscopy". In: *Biophysical Journal* 94.8 (2008), pp. L67 –L69.

[38] J. J. Fisz. "Fluorescence Polarization Spectroscopy at Combined High-Aperture Excitation and Detection: Application to One-Photon-Excitation Fluorescence Microscopy". In: *The Journal of Physical Chemistry A* 111.35 (2007), pp. 8606–8621.

[39] P. R. Dragsten. "Mechanism of Voltage-Induced Fluorescence Changes of the Membrane Probe Merocyanine 540. A Fluorescence Polarization Study". dissertation. Cornell University Ithaca, New York, 1977.

[40] D. Axelrod. "Carbocyanine dye orientation in red cell membrane studied by microscopic fluorescence polarization". In: *Biophysical Journal* 26.3 (1979), pp. 557 –573.

[41] Taekjip Ha et al. "Polarization Spectroscopy of Single Fluorescent Molecules". In: *The Journal of Physical Chemistry B* 103.33 (1999), pp. 6839–6850.

[42] J. J. Fisz. "Another Treatment of Fluorescence Polarization Microspectroscopy and Imaging". In: *The Journal of Physical Chemistry A* 113.15 (2009), pp. 3505–3516.

[43] J. R. Lakowicz. *Principles of Fluorescence Spectroscopy*. Second. New York Boston Dordrecht London Moscow: Kluwer Academic/Plenum Publishers, 1999.

[44] N. G. Walter et al. "Do-it-yourself guide: how to use the modern single-molecule toolkit". In: *Nature Methods* 5 (2008), pp. 475–489.

[45] T. Ha and P. Tinnefeld. "Photophysics of Fluorescence Probes for Single Molecule Biophysics and Super-Resolution Imaging". In: *Annual Reviews Physical Chemistry* 63 (2012), pp. 595–617.

[46] H. V. Drushel, A. L. Sommers, and R. C. Cox. "Correction of Luminescence Spectra and Calculation of Quantum Efficiencies Using Computer Techniques." In: *Analytical Chemistry* 35.13 (1963), pp. 2166–2172.

[47] C. A. Parker and W. T. Rees. "Correction of fluorescence spectra and measurement of fluorescence quantum efficiency". In: *Analyst* 85 (1013 1960), pp. 587–600.

[48] G. A. Crosby and J. N. Demas. "Measurement of photoluminescence quantum yields. Review". In: *The Journal of Physical Chemistry* 75.8 (1971), pp. 991–1024.

[49] D. Magde, E. Elson, and W. W. Webb. "Thermodynamic Fluctuations in a Reacting System—Measurement by Fluorescence Correlation Spectroscopy". In: *Phys. Rev. Lett.* 29 (11 Sept. 1972), pp. 705–708.

[50] E. L. Elson and D. Magde. "Fluorescence correlation spectroscopy. I. Conceptual basis and theory". In: *Biopolymers* 13.1 (Jan. 1974), pp. 1–27. ISSN: 1097-0282.

[51] J. Enderlein et al. "Performance of Fluorescence Correlation Spectroscopy for Measuring Diffusion and Concentration". In: *ChemPhys Chem* 6.11 (2005), pp. 2324–2336.

[52] J. Enderlein et al. "Art and Artefacts of Fluorescence Correlation Spectroscopy". In: *Current Pharmaceutical Biotechnology* 5.2 (2004), pp. 155–161.

[53] Y. Shimizu et al. "Cell free translation reconstituted with purified components". In: *Nature Biotechnology* 19 (2001), pp. 751–755.

[54] Y. Kuruma and T. Ueda. "The PURE system for the cell-free synthesis of membrane proteins". In: *Nature Protocols* 10 (2015), pp. 1328–1344.

[55] S. Nag et al. "Nature of the Amyloid-β Monomer and the Monomer-Oligomer Equilibrium". In: *Journal of Biological Chemistry* 286.16 (2011), pp. 13827–13833.

[56] J. Hu and C.-Y. Zhang. "Simple and Accurate Quantification of Quantum Yield at the Single-MoleculeParticle Level". In: *Analytical Chemistry* 85.4 (2013), pp. 2000–2004.

[57] A. I. Chizhik et al. "Nanocavity-Based Determination of Absolute Values of Photoluminescence Quantum Yields". In: *ChemPhysChem* 14.3 (2013).

[58] N. Karedla et al. "Absolute Photoluminescence Quantum Yield Measurement in a Complex Nanoscopic System with Multiple Overlapping States". In: *The Journal of Physical Chemistry Letters* 5.7 (), pp. 1198–1202.

[59] C. N. Pace. "[14]Determination and analysis of urea and guanidine hydrochloride denaturation curves". In: *Enzyme Structure Part L*. Vol. 131. Methods in Enzymology. Academic Press, 1986, pp. 266 –280.

[60] R. Chitra and P. E. Smith. "Molecular Dynamics Simulations of the Properties of Cosolvent Solutions". In: *The Journal of Physical Chemistry B* 104.24 (2000), pp. 5854–5864.

[61] K. Kawahara and C. Tanford. "Viscosity and Density of Aqueous Solutions of Urea and Guanidine Hydrochloride". In: *Journal of Biological Chemistry* 241.13 (1966), pp. 3228–3232.

[62] B. Dumat, A. F. Larsen, and L. M. Wilhelmsson. "Studying Z-DNA and B- to Z-DNA transitions using a cytosine analogue FRET-pair". In: *Nucleic Acids Research* 44.11 (2016), e101.

[63] N. F. Dupuis, E. D. Holmstrom, and D. J. Nesbitt. "Single-Molecule Kinetics Reveal Cation-Promoted DNA Duplex Formation Through Ordering of Single-Stranded Helices". In: *Biophysical Journal* 105.3 (2013), pp. 756 –766.

[64] A. H. Crevenna et al. "Effects of Hofmeister Ions on the α-Helical Structure of Proteins". In: *Biophysical Journal* 102.4 (2012), pp. 907 –915.

[65] K. Nörtemann, J. Hilland, and U. Kaatze. "Dielectric Properties of Aqueous NaCl Solutions at Microwave Frequencies". In: *The Journal of Physical Chemistry A* 101.37 (1997), pp. 6864–6869.

[66] H. Yuan et al. "Temperature-cycle single-molecule FRET microscopy on polyprolines". In: *Phys. Chem. Chem. Phys.* 13 (5 2011), pp. 1762–1769.

[67] M. J. Shoura et al. "Contribution of Fluorophore Dynamics and Solvation to Resonant Energy Transfer in Protein-DNA Complexes: A Molecular-Dynamics Study". In: *Biophysical Journal* 107.3 (2014), pp. 700 –710.

[68] J. B. Segur and H. E. Oberstar. "Viscosity of Glycerol and Its Aqueous Solutions". In: *Industrial & Engineering Chemistry* 43.9 (1951), pp. 2117–2120.

[69] R. Crawford et al. "Long-Lived Intracellular Single-Molecule Fluorescence Using Electroporated Molecules". In: *Biophysical Journal* 105.11 (2013), pp. 2439 –2450.

[70] I. König et al. "Single-molecule spectroscopy of protein conformational dynamics in live eukaryotic cells". In: *Nature methods* 12 (2015), pp. 773–779.

[71] J. J. Sakon and K. R. Weninger. "Detecting the conformation of individual proteins in live cells". In: *Nature methods* 7 (2010), pp. 203–205.

[72] M. Sustarsic and A. N. Kapanidis. "Taking the ruler to the jungle: single-molecule FRET for understanding biomolecular structure and dynamics in live cells". In: *Current Opinion in Structural Biology* 34 (2015), pp. 52 –59.

[73] H. M. Watkins et al. "Random coil negative control reproduces the discrepancy between scattering and FRET measurements of denatured protein dimensions". In: *Proceedings of the National Academy of Sciences* 112.21 (2015), pp. 6631–6636.

[74] H.-X. Zhou, G. Rivas, and A. P. Minton. "Macromolecular Crowding and Confinement: Biochemical, Biophysical, and Potential Physiological Consequences". In: *Annual Review of Biophysics* 37 (2008), pp. 375–397.

[75] L. E. Baltierra-Jasso et al. "Crowding-Induced Hybridization of Single DNA Hairpins". In: *Journal of the American Chemical Society* 137.51 (2015), pp. 16020–16023.

[76] M. Gao et al. "RNA Hairpin Folding in the Crowded Cell". In: *Angewandte Chemie International Edition* 55.9 (2016).

[77] J. Groen et al. "Associative Interactions in Crowded Solutions of Biopolymers Counteract Depletion Effects". In: *Journal of the American Chemical Society* 137.40 (2015), pp. 13041–13048.

[78] A. Soranno et al. "Single-molecule spectroscopy reveals polymer effects of disordered proteins in crowded environments". In: *Proceedings of the National Academy of Sciences* 111.13 (2014), pp. 4874–4879.

[79] R. Engel et al. "Macromolecular Crowding Compacts Unfolded Apoflavodoxin and Causes Severe Aggregation of the Off-pathway Intermediate during Apoflavodoxin Folding". In: *Journal of Biological Chemistry* 283.41 (2008), pp. 27383–27394.

[80] J. Li E.and Placone, M. Merzlyakov, and K. Hristova. "Quantitative Measurements of Protein Interactions in a Crowded Cellular Environment". In: *Analytical Chemistry* 80.15 (2008), pp. 5976–5985.

[81] D. S. Banks and C. Fradin. "Anomalous Diffusion of Proteins Due to Molecular Crowding". In: *Biophysical Journal* 89.5 (2005), pp. 2960–2971.

[82] A. J. Boersma, I. S. Zuhorn, and B. Poolman. "A sensor for quantification of macromolecular crowding in living cells". In: *Nature Methods* 12 (2015), pp. 227–229.

[83] E. Sherman and G. Haran. "Coil globule transition in the denatured state of a small protein". In: *Proceedings of the National Academy of Sciences* 103.31 (2006), pp. 11539–11543.

[84] T. Y. Yoo et al. "Small-Angle X-ray Scattering and Single-Molecule FRET Spectroscopy Produce Highly Divergent Views of the Low-Denaturant Unfolded State". In: *Journal of Molecular Biology* 418 (2012), pp. 226–236.

[85] H. Höfig et al. "Inter-Dye Distance Distributions Studied by a Combination of Single-Molecule FRET-Filtered Lifetime Measurements and a Weighted Accessible Volume (wAV) Algorithm". In: *Molecules* 19.12 (2014), pp. 19269–19291.

[86] A. Schöne. "Etablierung eines Systems aus Cysteinmutanten der Phos-phoglycerat Kinase für Entfaltungsstudien mit Einzelmolekül-FRET". dissertation. RWTH Aachen, 2016.

[87] L. F. Hoyt. "New Table of the Refractive Index of Pure Glycerol at 20°C". In: *Industrial and Engineering Chemistry* 26.3 (1934), pp. 329–332.

[88] M. Szabelski et al. "Evaluation of instrument response functions for lifetime imaging detectors using quenched Rose Bengal solutions". In: *Chemical Physics Letters* 471 (2009), pp. 153–159.

[89] *A Guide to Recording Fluorescence Quantum Yields*. HORIBA Jobin Yvon Ltd.

[90] E. Gaviola and P. Pringsheim. "Über den Einfluß der Konzentration auf die Polarisation der Fluoreszenz von Farbstofflösungen". In: *Zeitschrift für Physik* 24.1 (1924), pp. 24–36.

[91] J. B. Perrin. "Fluorescence et induction moléculaire par résonance." In: *Comptes rendus hebdomadaires des séances de l'Académie des sciences* 184 (1927), pp. 1097 –1100.

[92] F. Perrin. "Théorie quantique des transferts d'activation entre molécules de même espèce. Cas des solutions fluorescentes." In: *Annales de Physique* 17 (1932), pp. 283 –314.

[93] F. Perrin. "La Fluorescence des solutions: Induction moleculaire, polarisation et duree d'emission, photochemie." In: *Annales de Physique* 12 (1929), pp. 169 –275.

[94] B. W. van de Meer. "Förster Theory". In: *FRET-Förster Resonance Energy Transfer: From Theory to Applications*. Ed. by I. Medintz and N. Hildebrandt. Wiley-VCH Verlag GmbH and Co. KGaA, 2013, pp. 23–62.

[95] M. J. Levene et al. "Zero-Mode Waveguides for Single-Molecule Analysis at High Concentrations". In: *Science* 299.5607 (2003), pp. 682–686.

[96] F. L. H. Brown. "Generating functions for single-molecule statistics". In: *Theory and evaluation of single-molecule signals*. World Scientific Publishing Co. Pte. Ltd., 2008, pp. 61–92.

[97] Samuel T. H. and Watt W. W. "Focal Volume Optics and Experimental Artifacts in Confocal Fluorescence Correlation Spectroscopy". In: *Biophysical Journal* 83.4 (2002), pp. 2300 –2317.

[98] F. Pampaloni and J. Enderlein. "Gaussian, Hermite-Gaussian, and La-guerre-Gaussian beams: A primer". In: *ArXiv Physics e-prints* (Oct. 2004).

[99] J. Enderlein and C. Zander. "Theoretical Foundations of Single Molecule Detection in Solution". In: *Single Molecule Detection in Solution*. Wiley-VCH Verlag GmbH & Co. KGaA, 2003, pp. 21–67.

[100] O. Svelto. "Ray and Wave Propagation Through Optical Media". In: *Principles of Lasers, 5th edition*. Ed. by D. C. Hanna. Springer Science and Business Media, 2010, pp. 131–161.

[101] H. Qian and E. L. Elson. "Analysis of confocal laser-microscope optics for 3-D fluorescence correlation spectroscopy". In: *Appl. Opt.* 30.10 (Apr. 1991), pp. 1185–1195.

[102] *Quantitative FCS: Determination of the Confocal Volume by FCS and Bead Scanning with the MicroTime 200*. 1.1. Picoquant. 2009.

[103] X. Michalet et al. "Development of new photon-counting detectors for single-molecule fluorescence microscopy". In: *Philosophical Transactions of the Royal Society B: Biological Sciences* 368.1611 (2012).

[104] X. Michalet and S. Weiss. "Single-molecule spectroscopy and microscopy". In: *Comptes Rendus Physique* 3.5 (2002), pp. 619–644.

[105] R. Kühnemuth and C. A. M. Seidel. "Principles of Single Molecule Multiparameter Fluorescence Spectroscopy". In: *Single Molecules* 2.4 (2001), pp. 251–254.

[106] S. Nie, D. T. Chiu, and R. N. Zare. "Probing individual molecules with confocal fluorescence microscopy". In: *Science* 266.5187 (1994), pp. 1018–1021.

[107] C. W. Wilkerson Jr. et al. "Detection and lifetime measurement of single molecules in flowing sample streams by laser induced fluorescence". In: *Applied Physics Letters* 62.17 (1993), pp. 2030–2032.

[108] C. Eggeling et al. "Monitoring conformational dynamics of a single molecule by selective fluorescence spectroscopy". In: *Proceedings of the National Academy of Sciences* 95.4 (1998), pp. 1556–1561.

[109] E. Nir et al. "Shot-Noise Limited Single-Molecule FRET Histograms: Comparison between Theory and Experiments". In: *The Journal of Physical Chemistry B* 110.44 (2006), pp. 22103–22124.

[110] J. R. Fries et al. "Quantitative Identification of Different Single Molecules by Selective Time-Resolved Confocal Fluorescence Spectroscopy". In: *The Journal of Physical Chemistry A* 102.33 (1998), pp. 6601–6613.

[111] Y. Chen et al. "The Photon Counting Histogram in Fluorescence Fluctuation Spectroscopy". In: *Biophysical Journal* 77.1 (1999), pp. 553 –567.

[112] I. V. Gopich and . Szabo. "Single-Molecule FRET with Diffusion and Conformational Dynamics". In: *The Journal of Physical Chemistry B* 111.44 (2007), pp. 12925–12932.

[113] A. Miseta and P. Csutora. "Relationship Between the Occurrence of Cysteine in Proteins and the Complexity of Organisms". In: *Molecular Biology and Evolution* 17.8 (2000), pp. 1232–1239.

[114] P. Carter. "Site-directed mutagenesis". In: *Biochemical Journal* 237.1 (1986), pp. 1–7.

[115] N. J. Greenfield. "Using circular dichroism spectra to estimate protein secondary structure". In: *Nature Protocols* 1.6 (2007), pp. 2876–2890.

[116] B. K. Müller et al. "Pulsed Interleaved Excitation". In: *Biophysical Journal* 89.5 (2005), pp. 3508 –3522.

[117] I. Gopich and A. Szabo. "Theory of photon statistics in single-molecule Förster resonance energy transfer". In: *The Journal of Chemical Physics* 122.1 (2005), p. 014707.

[118] S. Kalinin et al. "On the Origin of Broadening of Single-Molecule FRET Efficiency Distributions beyond Shot Noise Limits". In: *The Journal of Physical Chemistry B* 114.18 (2010), pp. 6197–6206.

[119] L. Onsager. "Reciprocal Relations in Irreversible Processes. I." In: *Phys. Rev.* 37 (4 Feb. 1931), pp. 405–426.

[120] L. Onsager. "Reciprocal Relations in Irreversible Processes. II." In: *Phys. Rev.* 38 (12 Dec. 1931), pp. 2265–2279.

[121] J. Widengren and R. Rigler. "Ultrasensitive detection of single molecules by fluorescence correlation spectroscopy". In: *Bioscience* 3 (1990), pp. 180–183.

[122] P. Schwille. "Cross-correlation analysis in FCS". In: *Fluorescence Correlation Spectroscopy: Theory and Applications*. Ed. by R. Rigler and E. S. Elson. Springer Verlag Berlin Heidelberg New York, 2001, pp. 360–378.

[123] P. Kapusta. *Absolute Diffusion Coefficients: Compilation of Reference Data for FCS Calibration*. Picoquant. 2010.

[124] J. Enderlein and I. Gregor. "Using fluorescence lifetime for discriminating detector afterpulsing in fluorescence-correlation spectroscopy". In: *Review of Scientific Instruments* 76.3 (2005), p. 033102.

[125] K. Kinosita, A. Ikegami, and S. Kawato. "On the wobbling-in-cone analysis of fluorescence anisotropy decay". In: *Biophysical Journal* 37.2 (1982), pp. 461 –464.

[126] S. Rüttinger. "Confocal Microscopy and Quantitative Single Molecule Techniques for Metrology in Molecular Medicine". dissertation. Technische Universität Berlin, 2006.

[127] D. Petrásek and P. Schwille. "Precise Measurement of Diffusion Coefficients using Scanning Fluorescence Correlation Spectroscopy". In: *Biophysical journal* 94.4 (2007), pp. 1437–1448.

[128] M. Wahl. *Time-correlated single photon counting*. Picoquant. 2014.

[129] E. Rusinova et al. "Alexa and Oregon Green dyes as fluorescence anisotropy probes for measuring protein - protein and protein - nucleic acid interactions". In: *Analytical Biochemistry* 308 (2002), pp. 18–25.

[130] M. J. Nasse and J. C. Woehl. "Realistic modeling of the illumination point spread function in confocal scanning optical microscopy". In: *J. Opt. Soc. Am. A* 27.2 (Feb. 2010), pp. 295–302.

[131] J. Widengren, U. Mets, and R. Rigler. "Fluorescence correlation spectroscopy of triplet states in solution: a theoretical and experimental study". In: *The Journal of Physical Chemistry* 99.36 (1995), pp. 13368–13379.

[132] I. Gregor, D. Patra, and J. Enderlein. "Optical Saturation in Fluorescence Correlation Spectroscopy under Continuous-Wave and Pulsed Excitation". In: *ChemPhysChem* 6.1 (2005), pp. 164–170.

[133] C. Eggeling et al. "Analysis of Photobleaching in Single-Molecule Multicolor Excitation and Förster Resonance Energy Transfer Measurements". In: *The Journal of Physical Chemistry A* 110.9 (2006), pp. 2979–2995.

[134] H. Blom et al. "Triplet-State Investigations of Fluorescent Dyes at Dielectric Interfaces Using Total Internal Reflection Fluorescence Correlation Spectroscopy". In: *The Journal of Physical Chemistry A* 113.19 (2009), pp. 5554–5566.

[135] D. E. Koppel. "Statistical accuracy in fluorescence correlation spectroscopy". In: *Phys. Rev. A* 10 (6 Dec. 1974), pp. 1938–1945.

[136] V. Buschmann, K. D. Weston, and M. Sauer. "Spectroscopic Study and Evaluation of Red-Absorbing Fluorescent Dyes". In: *Bioconjugate Chemistry* 14.1 (2003), pp. 195–204.

[137] J. Widengren and P. Schwille. "Characterization of Photoinduced Isomerization and Back-Isomerization of the Cyanine Dye Cy5 by Fluorescence Correlation Spectroscopy". In: *The Journal of Physical Chemistry A* 104.27 (2000), pp. 6416–6428.

[138] S. Rüttinger et al. "Comparison and accuracy of methods to determine the confocal volume for quantitative fluorescence correlation spectroscopy". In: *Journal of Microscopy* 232.2 (2008), pp. 343–352.

[139] A. Einstein. "Über die von der molekularkinetischen Theorie der Wärme geforderte Bewegung von in ruhenden Flüssigkeiten suspendierten Teilchen". In: *Annalen der Physik* 322.8 (1905), pp. 549–560.

[140] G. G. Stokes. "On the Effect of the Internal Friction of Fluids on the Motion of Pendulums". In: *Transactions of the Cambridge Philosophical Society* 9 (1851), p. 8.

[141] Glycerine Producers' Association. *Physical Properties of Glycerine and Its Solutions*. Glycerine Producers' Association, 1963.

[142] N. S. Heyman and J. M. Burt. "Hindered Diffusion through an Aqueous Pore Describes Invariant Dye Selectivity of Cx43 Junctions". In: *Biophysical Journal* 94.3 (2008), pp. 840 –854.

[143] J. Widengren and P. Schwille. "Characterization of Photoinduced Isomerization and Back-Isomerization of the Cyanine Dye Cy5 by Fluorescence Correlation Spectroscopy". In: *The Journal of Physical Chemistry A* 104.27 (2000), pp. 6416–6428.

[144] A. Brouwer. "Standards for photoluminescence quantum yield measurements in solution (IUPAC Technical Report)". In: *Pure and Applied Chemistry* 83.11 (2011), pp. 2213–2228.

[145] S. J. Strickler and R. A. Berg. "Relationship between Absorption Intensity and Fluorescence Lifetime of Molecules". In: *The Journal of Chemical Physics* 37.4 (1962), pp. 814–822.

[146] M. A. El-Bayoumi, J. P. Dalle, and F. O'Dwyer. "Fluorescence lifetimes of molecules that undergo large configurational changes upon excitation". In: *Journal of the American Chemical Society* 92.11 (1970), pp. 3494–3495.

[147] T. Susdorf et al. "Absorption and emission spectroscopic characterization of some azo dyes and a diamino-maleonitrile dye". In: *Chemical Physics* 333 (2007), pp. 49–56.

[148] H. Chen et al. "Mechanisms of Quenching of Alexa Fluorophores by Natural Amino Acids". In: *Journal of the American Chemical Society* 132.21 (2010), pp. 7244–7245.

[149] D. Haenni et al. "Intramolecular Distances and Dynamics from the Combined Photon Statistics of Single-Molecule FRET and Photoinduced Electron Transfer". In: *The Journal of Physical Chemistry B* 117.42 (2013), pp. 13015–13028.

[150] M. Robins and A. Fillery-Travis. "Colloidal dispersions." In: *Journal of Chemical Technology and Biotechnology* 54.2 (1992), pp. 201–202.

[151] S. Sindbert et al. "Accurate Distance Determination of Nucleic Acids via Förster Resonance Energy Transfer: Implications of Dye Linker Length and Rigidity". In: *Journal of the American Chemical Society* 133.8 (2011), pp. 2463–2480.

[152] M. van Dijk and A. M. J. J. Bonvin. "3D-DART: a DNA structure modelling server". In: *Nucleic Acids Research* 37.suppl 2 (2009), W235–W239.

[153] B. W. van der Meer. "Kappa-squared: from nuisance to new sense". In: *Reviews in Molecular Biotechnology* 82.3 (2002), pp. 181 –196.

[154] J. K. Chung and A. R. Denton. "Effective electrostatic interactions in mixtures of charged colloids". In: *Phys. Rev. E* 88 (2 Aug. 2013), p. 022306.

[155] C. Gutsche et al. "Forces between single pairs of charged colloids in aqueous salt solutions". In: *Phys. Rev. E* 76 (3 Sept. 2007), p. 031403.

[156] G. F. Schröder, U. Alexiev, and H. Grubmüller. "Simulation of Fluorescence Anisotropy Experiments: Probing Protein Dynamics". In: *Biophysical Journal* 89.6 (2005), pp. 3757 –3770.

[157] L. A. Campos et al. "A photoprotection strategy for microsecond-resolution single-molecule fluorescence spectroscopy". In: *Nature methods* 8 (2011), pp. 143 –146.

[158] M. Koshioka, K. Sasaki, and H. Masuhara. "Time-Dependent Fluorescence Depolarization Analysis in Three-Dimensional Microspectroscopy". In: *Appl. Spectrosc.* 49.2 (Feb. 1995), pp. 224–228.

[159] J. B. Pawley. *Handbook of Biological Confocal Microscopy*. Third. New York: Springer Science and Business Media, 2006.

[160] J. Schaffer et al. "Identification of Single Molecules in Aqueous Solution by Time-Resolved Fluorescence Anisotropy". In: *The Journal of Physical Chemistry A* 103.3 (1999), pp. 331–336.

[161] C. B. Müller et al. "Dual-focus fluorescence correlation spectroscopy: a robust tool for studying molecular crowding". In: *Soft Matter* 5 (7 2009), pp. 1358–1366.

[162] C. A. M. Seidel, A. Schulz, and M. H. M. Sauer. "Nucleobase-Specific Quenching of Fluorescent Dyes. 1. Nucleobase One-Electron Redox Potentials and Their Correlation with Static and Dynamic Quenching Efficiencies". In: *The Journal of Physical Chemistry* 100.13 (1996), pp. 5541–5553.

[163] B. Wilhelmi. "Influence of solvent viscosity on excited state lifetime and fluorescence quantum yield of dye molecules". In: *Chemical Physics* 66.3 (1982), pp. 351 –355.

[164] T. Nakabayashi et al. "pH dependence of the fluorescence lifetime of enhanced yellow fluorescent protein in solution and cells". In: *Journal of Photochemistry and Photobiology A: Chemistry* 235 (2012), pp. 65 –71.

[165] Y. Chen et al. "The Photon Counting Histogram in Fluorescence Fluctuation Spectroscopy". In: *Biophysical Journal* 77.1 (1999), pp. 553 –567.

[166] M. Aznauryan et al. “Comprehensive structural and dynamical view of an unfolded protein from the combination of single-molecule FRET, NMR, and SAXS”. In: *Proceedings of the National Academy of Sciences* 113.37 (2016), E5389–E5398.

[167] H. M. Watkins et al. “Random coil negative control reproduces the discrepancy between scattering and FRET measurements of denatured protein dimensions”. In: *Proceedings of the National Academy of Sciences* 112.21 (2015), pp. 6631–6636.

[168] M. Neumann and D. Gabel. “Simple Method for Reduction of Autofluorescence in Fluorescence Microscopy”. In: *Journal of Histochemistry & Cytochemistry* 50.3 (2002), pp. 437–439.